REPORT DOCUMENTATION PAGE		READ INSTRUCTIONS BEFORE COMPLETING FORM
1 REPORT NUMBER AFIT/CI/NR 83-82D	2 GOVT ACCESSION NO A139173	3 RECIPIENT'S CATALOG NUMBER
4 TITLE (and Subtitle) Autonomous Navigation of USAF Spacecraft		5 TYPE OF REPORT & PERIOD COVERED THESIS/DISSERTATION
		6 PERFORMING ORG. REPORT NUMBER
7. AUTHOR(s) Jackson Robert Ferguson, Jr.		8 CONTRACT OR GRANT NUMBER(s)
9 PERFORMING ORGANIZATION NAME AND ADDRESS AFIT STUDENT AT: University of Texas at Austin		10 PROGRAM ELEMENT PROJECT, TASK AREA & WORK UNIT NUMBERS
11 CONTROLLING OFFICE NAME AND ADDRESS AFIT/NR WPAFB OH 45433		12 REPORT DATE December 1983
		13. NUMBER OF PAGES 193
14 MONITORING AGENCY NAME & ADDRESS(if different from Controlling Office)		15 SECURITY CLASS (of this report) UNCLASS
		15a DECLASSIFICATION DOWNGRADING SCHEDULE

16 DISTRIBUTION STATEMENT (of this Report)

APPROVED FOR PUBLIC RELEASE; DISTRIBUTION UNLIMITED

17 DISTRIBUTION STATEMENT (of the abstract entered in Block 20, if different from Report)

18. SUPPLEMENTARY NOTES

APPROVED FOR PUBLIC RELEASE: IAW AFR 190-17

13 Feb 1984

LYNN E. WOLAVER
Dean for Research and
Professional Development

19 KEY WORDS (Continue on reverse side if necessary and identify by block number)

20 ABSTRACT (Continue on reverse side if necessary and identify by block number)

ATTACHED

DTIC
ELECTE
MAR 2 1 1984
E

DD FORM 1473 EDITION OF 1 NOV 65 IS OBSOLETE

UNCLASS

AUTONOMOUS NAVIGATION OF

USAF SPACECRAFT

by

Jackson Robert Ferguson, Jr., B.S., M.S.

DISSERTATION

Presented to the Faculty of the Graduate School of

The University of Texas at Austin

in Partial Fulfillment

of the Requirements

for the Degree of

DOCTOR OF PHILOSOPHY

THE UNIVERSITY OF TEXAS AT AUSTIN

December 1983

AUTONOMOUS NAVIGATION OF

USAF SPACECRAFT

APPROVED BY SUPERVISORY COMMITTEE:

B. D. Tapley

Raynor L. Duncombe

Wallace T. Fowler

Thomas Allen

B.E. Schutz

R. Bruce

ACKNOWLEDGMENTS

Even though my name appears alone on the cover of this dissertation, it was a cooperative effort. I want to thank all of my professors at the University of Texas for their insight and their time, especially Byron D. Tapley and Raynor L. Duncombe. Their help was above and beyond the call of duty. I also received an education in space systems from two Aerospace Corporation experts: Dr. Joseph L. Lemay and Roy T. Pace.

One other person spent almost as much time as I on this project, and all compliments concerning style and appearance should go to her: Karen Johnson from the University of Texas. All complaints concerning content should go to me.

Finally and most importantly, I thank my wife, Christine, and children, Jack and Joy, for their undying love and patience, and especially for their gentle pressure to finish.

AUTONOMOUS NAVIGATION OF USAF SPACECRAFT

Publication No.

Jackson Robert Ferguson, Jr., Ph.D.
The University of Texas at Austin, 1983

Supervising Professor: Byron D. Tapley

The U. S. Air Force is developing satellite-borne sensors to enable autonomous navigation of spacecraft in the near future. This study compares the observations from several medium-accuracy space sensors, such as the existing telescopic space sextant, with those of future matrix-type sensors. The large field of view of matrix sensors will allow them to determine the earth horizon to approximately an order of magnitude better than current infrared sensors by observing atmospheric refraction of stellar light. This horizon determination will give the matrix sensors an accuracy of less than 1 km. The limiting factor in earth-horizon determination is the modeling of atmospheric refraction effects. For high-accuracy requirements (100 meters or less), the Global Positioning System (GPS) offers the only near-term solution. A relative navigation technique using range and doppler data is proposed for autonomous navigation of the GPS satellites. The navigation accuracy of this technique is evaluated by consider covariance

analysis and by processing corrupted data through a reduced-order onboard Sequentially Partitioned Algorithm. The algorithm is stable and for the GPS system pro uces in-plane accuracy of 40 meters over twenty days. However, out-of-plane motion is shown to be unobservable in the GPS-to-GPS tracking mode, and errors of up to 1.5 km over 60 days are experienced. For this reason, a supplemental transmitter on the ground or in a different orbit is recommended.

TABLE OF CONTENTS

viii

LIST OF FIGURES

xi

LIST OF TABLES

LIST OF ACRONYMS

CHAPTER 1

INTRODUCTION

1.1 Autonomous Satellite Navigation History

Self-contained or autonomous navigation of spacecraft was
a desired capability almost at the very beginning of space flight.
The earliest references to space navigation discuss its necessity
for manned missions and interplanetary travel [Henry, 1963; Gersten
and Schwarzbein, 1963], but unmanned earth satellites have continued
to be tracked and controlled by worldwide tracking networks. These
networks, set up by both the United States Air Force and the
National Aeronautics and Space Administration (NASA) are complex,
expensive, redundant and require large operation and maintenance
budgets.

Studies of artificial satellite autonomous navigation
sensors and techniques have been performed since the late 1960
decade by Brogan and Lemay [1968], Gura, et al. [1971] and Lemay, et
al. [1973], but sensor development has lagged far behind the
analyses and only recently have serious moves been taken to build
and test sensors that will enable transfer of the navigation
function from the earth-based system to each active spacecraft.
NASA, driven primarily by cost considerations, is planning to use
the Tracking and Data Relay Satellite System (TDRSS) as an orbital
tracking station, with data processing still to be performed on the

1

ground. The Department of Defense (DOD), however, is more concerned with vulnerability, as stated by Robert S. Cooper, head of the Defense Advanced Research Projects Agency [Aviation Week, 1982], and with the overseas ground stations being the most vulnerable links in the tracking and control system, DOD is funding spaceborne sensor systems of varying degrees of autonomy to enable the onboard performance of the navigation function.

Previous autonomous satellite navigation investigations involved several different types of sensors. Lemay, et al. [1973] thoroughly investigated the use of both known and unknown landmark trackers, horizon scanners, satellite-to-satellite measurements of angles, range and range-rate, star-horizon sensors and space sextant measurements. Their investigation, which was based upon state-of-the-art sensor precision in 1973, indicated that landmark trackers had the potential for yielding the best navigation performance. Development of landmark trackers, however, never achieved the potential expected of them, and optical star trackers, along with the Global Positioning System (GPS), are the onboard navigation systems currently under development.

It is interesting to note that USSR interest in autonomous navigation started somewhat parallel to but behind the United States. The paper by Zybin [1969] proposes using star-planet observations in a deterministic orbit determination scheme similar to Gersten [1963]. On-orbit testing of space sextants occurred

early in both manned space programs. Experiments were performed on both the Gemini [Ballentine, 1967] and Skylab [Walsh and Ferrguson, 1975] spacecraft, as well as in the Soviet manned spacecraft [Nikoloev, et al., 1975].

1.2 Air Force Spacecraft Navigation Requirements

The new sensors under development promise navigation accuracies that may be competitive with ground-based systems in meeting most current and projected Air Force spacecraft position knowledge requirements. Discussions with Air Force System Program Offices (SPO's) during the summer of 1981 led to a list of accuracy requirements whose one-sigma values spanned the range from less than 10 m to ore than 37 km [Tapley and Ferguson, 1983].

To meet these requirements, some of the program offices are investigating the use of current sensor data, while others will require new sensors of the type being developed. The Defense Meteorological Support Program (DMSP) is typical of those investigating their current sensor capabilities. The DMSP Primary Attitude Determination System (PADS) consists of a fixed star tracker pair, a sun sensor and earth horizon sensors. When all sensors are in operation, the attitude error sigma is 36 arcsec and the system outputs attitude errors and a unit vector pointing to the center of the earth. This unit vector can be utilized by a navigation filter to perform the autonomous navigation function. Current sensor data studies have a goal of 1 nm accuracy with

atmospheric radiance, bias modeling and filter design being the areas needing improvements. Since the program navigation requirement is .5 nm (930 meters), improvements to the sensors or new horizon sensors are necessary. Other programs, whose accuracy requirements are in the 100 m-1 km range, are also candidates for the optical star trackers being built and tested under Space Division auspices.

Some satellite programs, however, require position knowledge to 50 m or less and will thus necessitate the development of extremely precise onboard measurement equipment. The GPS program is not only one of those that requires very accurate navigation information but is the only navigation system proposed whose position accuracies meet the requirements of other high-precision users. It's main limitation from an autonomous system viewpoint is that it is dependent upon a global tracking system. User satellites are thus dependent upon a navigation system that is still vulnerable to ground system failures and outages.

The GPS Joint Program Office (JPO) has performed limited studies on two autonomous navigation schemes, one using range and integrated doppler measurements from other GPS vehicles via the cross-link antenna and the other involving precise horizon data from a new optical sensor. The GPS satellite relative range study by Liu [1981] indicates that although in-track errors grow to 30 meters, 10 meter accuracy can be maintained in the user line-of-sight

direction for Phase I vehicles involved in active satellite-to-satellite cracking for 14 days following one day of ground tracking. Earth geopotential resonance terms are the largest error sources, and improved values for C_{44}, S_{44}, C_{32} and S_{32} are required. The study did not address the Phase III constellation, long-term stability, clock variation or stability of an onboard solution process.

The optical sensor proposed for GPS measures the earth's horizon by atmospheric dispersion of star images, and is named SHAD for Stellar Horizon by Atmospheric Dispersion. The current sensor design is intended for mid-course missile guidance and is expected to result in a position error sigma of 65 m [Quell, 1981], so it would require approximately an order of magnitude improvement to be used by GPS. Earth atmospheric density modeling, as discussed in Section 2.8, is a major factor limiting the accuracy achievable by SHAD.

1.3 Purpose of the Study

While some Air Force satellite SPO's are actively investigating the capability of current and future onboard sensors, several others are either independently soliciting proposals for new sensors or are waiting for sensors to be developed to the operational stage before making a decision on the route they will take to satisfy autonomous navigation requirements. There is a need to assess the capabilities of sensors now under development, match

them to these program requirements and identify needed improvements so that decisions can be made as to the direction future sensor development should take. The purpose of this study, then, is to assess navigation accuracies using these new sensors so they may be matched to existing and planned satellite missions. Since some users have requirements that can only be met by GPS, an investigation of improved GPS autonomy is also undertaken.

The report consists of a description of the new technology, a comparison of the two main types of optical sensors under development: the Space Sextant and the matrix star sensor, and an analysis of GPS autonomous navigation using satellite-to-satellite range and integrated doppler measurements. The GPS section contains a relative geometry description, a description of relevant error sources, ephemeris model selection using consider analysis, orbit and clock simulation descriptions and analysis of a proposed local estimation algorithm. Conclusions concerning the various sensors are drawn and recommendations are made.

1.4 Description of Sensors

Five of the sensors now under development yield data which hold high promise for current autonomous navigation applications. These include the Space Sextant Autonomous Navigation and Attitude Reference System (SS/ANARS), the Multimission Attitude Determination and Autonomous Navigation System (MADAN) and the Digistar and STELLAR star sensors. The measurement from each of these sensors is

based on the sensor's ability to measure accurately the angle between a star and a near celestial body or the angle between two stars. One additional sensor, the GPSPAC, uses range and/or integrated doppler measurements from the Global Positioning System satellites as data for the navigation function. The advertised characteristics as determined by the design specifications for these sensors are given in Table 1.1. Operational characteristics of each sensor are described in further detail in the subsequent discussion.

TABLE 1.1. ADVERTISED SYSTEM CHARACTERISTICS

Type	1c Sensor Precision	Weight	Power	Operational Date
Space Sextant	.5 arcsec	65 lbs	50 watts	1985
MADAN	2 arcsec	50 lbs	50 watts	1987
Digistar	.5-2 arcsec	30-60 lbs	30-60 watts	1985 (2 arcsec)
STELLAR	1-30 arcsec	40 lbs	40 watts	
GPSPAC	Pos: 18 m Att: .02°-.6° (71-2143 arcsec)	43 lbs	45 watts	1987

1.4.1 Space Sextant

The Space Sextant Autonomous Navigation and Attitude Reference System is being developed by Martin-Marietta. A flight demonstration model has been built and ground-tested, and an operational version may be ready by 1985. The test model weighs approximately 220 lbs and consumes 280 watts, but the operational model proposed for the Mini-HALO program is advertised to weigh 65 lbs and consume 50 watts of power [Martin-Marietta, 1980].

The sextant is composed of two cassegrain tracking telescopes mounted on a 3 degree-of-freedom inertial platform (Fig. 1.1). In the navigation mode, one telescope tracks the bright limb of the moon, while the other tracks stars visible to the system. A timing wheel located between the telescopes rotates a prism at 9 rps such that optical signals are injected into each telescope parallel to the received starlight. The angle between the two lines of sight is then determined to < .5 arcsec by measuring the time interval between the optical signal reception at each telescope's detector.

1.4.2 MADAN

The Multimission Attitude Determination and Autonomous Navigation system is a solid-state matrix star sensor being developed by TRW (Fig. 1.2). The heart of the sensor is a matrix charge-coupled device (CCD) developed by Hughes. The matrix contains four arrays of 324 x 324 elements or pixels, each 1 mil x 1 mil (25.4 μm x 25.4 μm) [TRW, 1979]. A Schmidt-Cassegrain reflecting telescope with a 7.1° x 7.1° field of view produces an intentionally defocused image on the array and a sensor data processor determines the centroid of the image to approximately 5 percent of a pixel width with respect to the sensor line of sight. Since each pixel subtends 39.4 sec, a 5 percent error gives 1σ < 2 arcsec. Two such sensors can be used to determine spacecraft attitude, but the star sensor, along with its data processor, is not capable of autonomous navigation without an earth horizon sensor.
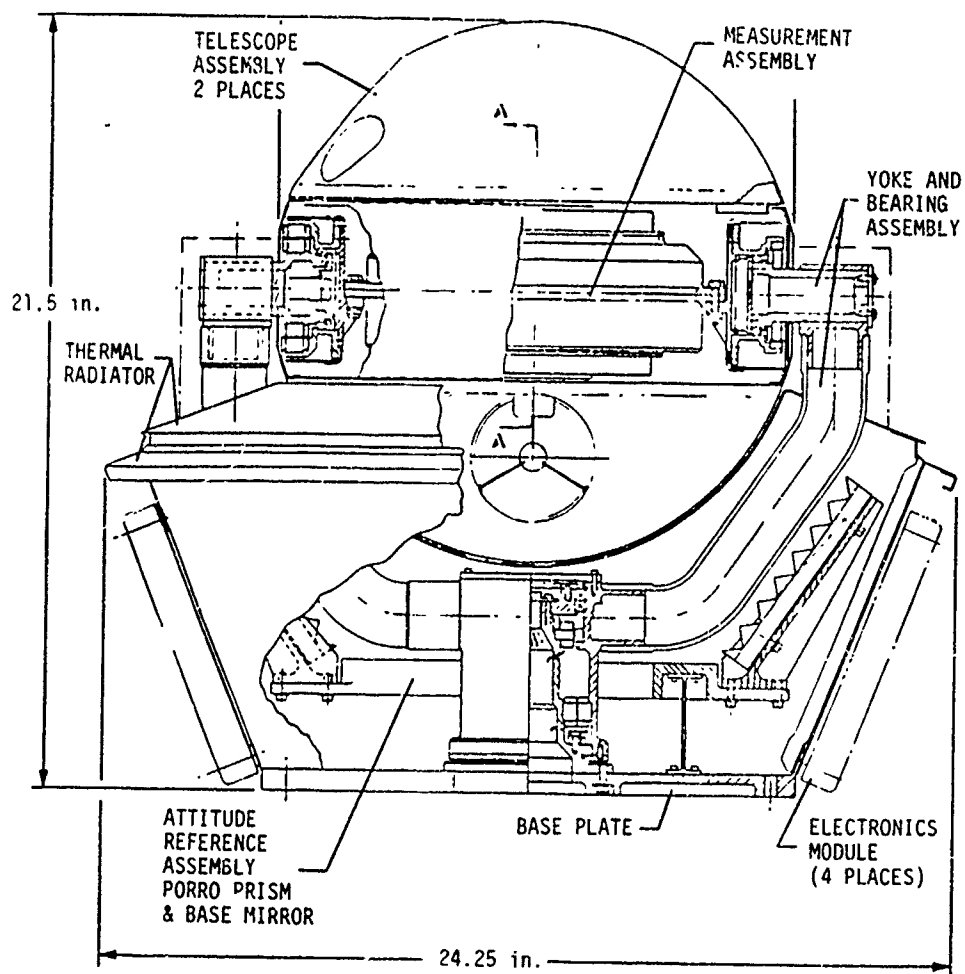
Courtesy of Martin-Marietta Corp.

Figure 1.1. Space Sextant
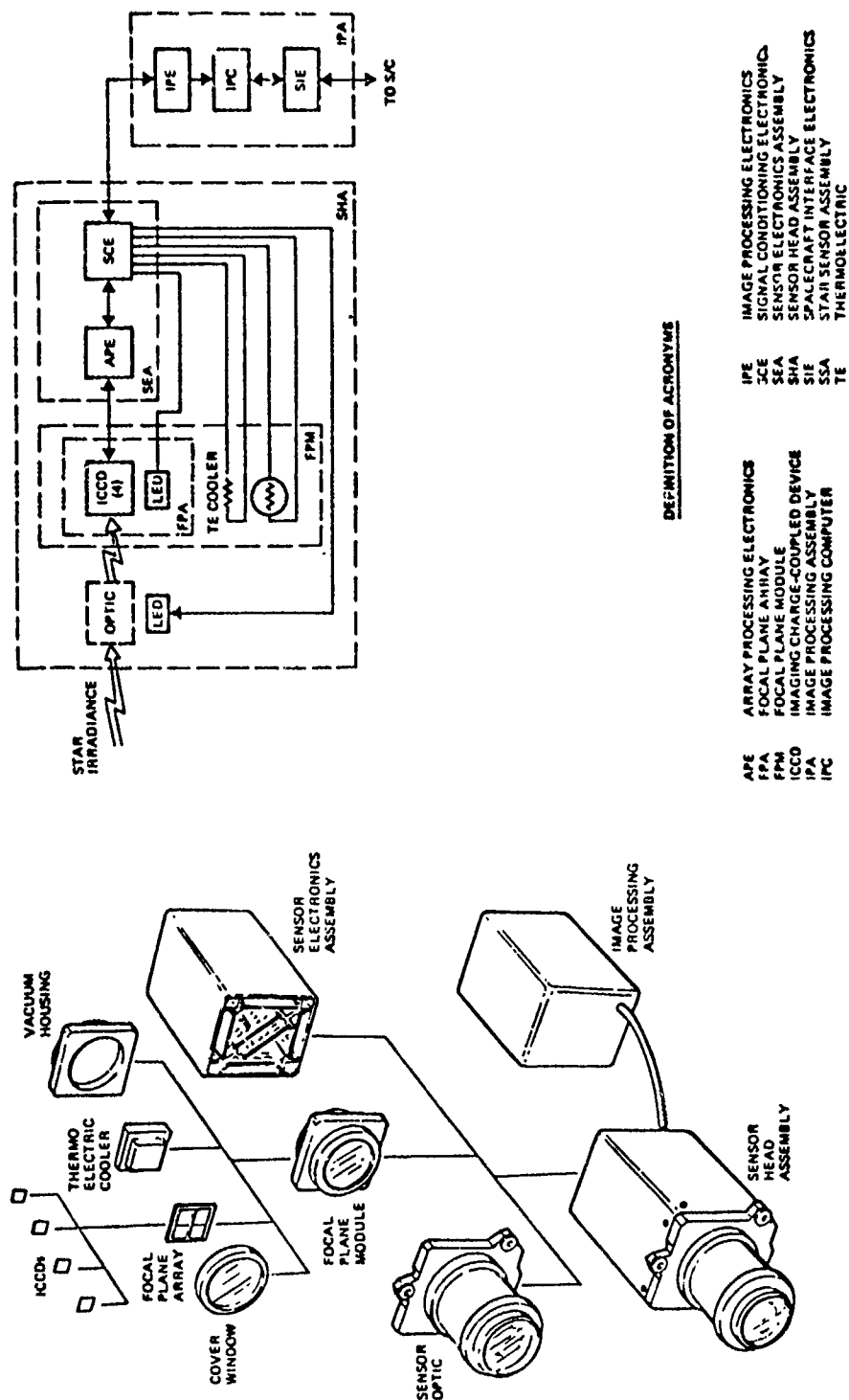
Figure 1.2. MADAN Star Sensor

Courtesy of TRW

It may be possible to use the star sensor as an earth horizon sensor by measuring a star position as it is refracted by the atmosphere, but the current design does not include the necessary software. The use of this sensor for horizon determination is discussed further in Section 2.4.1.

A MADAN test model is being fabricated by TRW, with bench test results expected in 1983. An operational version could be flown by 1987.

1.4.3 Digistar

Digistar is another solid-state matrix star sensor being built by Ball Aerospace Systems Division (Fig. 1.3). It employs a 256 x 256 pixel charge injection device (CID) developed by the General Electric Corporation. Each pixel element is 20 x 20 μm. The refracting telescope produces an image on the focal plane matrix, and an interpolation scheme is used to arrive at an image centroid with a precision of less than 1 percent of pixel size in a field of view of 2.93° x 2.93°. Since each pixel subtends 41 arcsec, the resulting star position precision is expected to be about .4 arcsec. Testing of a breadboard model currently demonstrates a 1σ tracking error of .8 arcsec [Ball Aerospace, 1981]. According to a Ball representative, an operational model could fly in 1985.
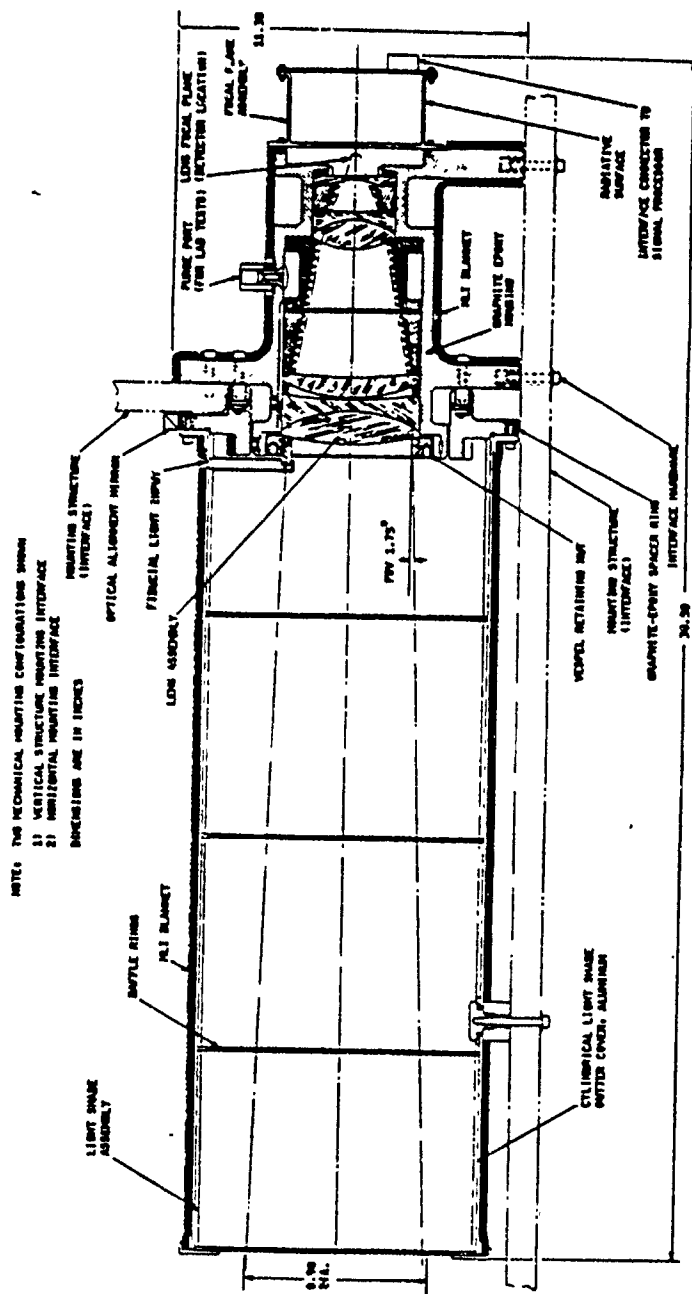
Note: Additional signal processor assembly required; approximate dimensions: 6.75 in. high x 6.25 in. wide x 7.8 in. long

Courtesy of Ball Aerospace Systems Division

Figure 1.3. Digistar Star Tracker

1.4 4 STELLAR

The Jet Propulsion Laboratory (JPL) has been developing CCD-based star sensors since 1974 [Salomon, 1981]. The project is named STELLAR for Star Tracker for Economical Long Life Attitude Reference. To date, two large array trackers have been developed. The Video Inertial Pointing (VIP) tracker employs a Fairchild-produced CCD having a 190 x 244 element array with a 1.9° x 2.5° field-of-view, 36 arcsec pixels and 2.2 arcsec resolution. This instrument flew on a balloon payload in June 1979.

The Extended Life Attitude Control System (ELACS) tracker uses a 380 x 488 element CCD built by Fairchild and has a 10° x 32° field-of-view. The resolution is 12 arcsec along the short axis and 30 arcsec along the long axis. Even though it is less accurate than the VIP tracker, it allows commandable fields-of-view, so several operating modes, such as star field mapping, star acquisition and star tracking, are available from one instrument.

The JPL goal is to have three instruments: a wide-field star tracker, like ELACS, a general purpose tracker and an instrument pointing sensor with accuracies varying from 30 to 1 arcsec. According to Salomon [1981], each tracker would weigh between 8 and 13 lb and draw 10 watts of power.

1.4.5 GPSPAC

A spaceborne Global Position System receiver (GPSPAC) is under development by Magnavox, among others. Utilizing the GPS

ranging signal, position errors of 18 m (1σ) are expected for user satellites below GPS altitude (20197 km) in Phase III operation. This system is dependent upon the GPS spacecraft launch schedule but is expected to be operational in 1987.

User satellite attitude can be determined from GPS-derived interferometric information obtained by using two widely separated antennas and a suitably modified receiver. This information is obtained separately from the navigation data and requires additional receiver design. Attitude determination accuracy using this technique is only on the order of .02° to .6° [Ellis and Creswell, 1978].

1.5 Sensor Comparison

The relative advantages and disadvantages of each sensor, from the operational point of view, can be summarized as follows:

A. Space Sextant

Advantages:

1. High-accuracy angle measurement

2. Self-gimbaled

3. Early operational date

Disadvantages:

1. Mechanical gimbals, possibly reducing reliability

2. Moon-star angle is less sensitive to orbit dynamics than an earth-star angle.

B. Solid-state Matrix Sensor (MADAN, Digistar and STELLAR)

Advantages.

   1. Small, solid state

   2. Modular

   3. Can view several stars simultaneously

Disadvantages:

   1. Fixed to spacecraft with no automatic scan capability

   2. No existing comparable earth horizon sensor

   3. Later operational date for a navigation system

C. GPS Receiver

   Advantages: High positional accuracy

   Disadvantages:

   1. Dependent on ground tracking system

   2. Low attitude precision

CHAPTER 2

OPTICAL SENSOR NAVIGATION ACCURACIES

2.1 Introduction

Since the various instruments described in the previous sections will provide different navigation information, conversions must be made from sensor precision to spacecraft position error to compare the navigation accuracies of the three types of instruments. For the GPSPAC, simulations of the ranging system errors coupled with GPS ephemeris and clock errors produce a user position error of less than 18 meters during periods when at least four satellites with acceptable geometrical displacement are visible [Fuchs, et al., 1977]. Since earth-orbiting satellites will continuously see at least four GPS vehicles in Phase III, this accuracy is assumed for all users. Semi-autonomous maintenance of GPS ephemerides is analyzed in later chapters.

The Space Sextant has been analyzed in detail by the Martin-Marietta Corporation [1975], and a navigation accuracy of 300 meters is predicted for a .5 arcsec sensor. The matrix sensors have not been analyzed in detail nor have the comparisons between them and the Space Sextant been made. Such a comparison will be a primary objective of this study. Since the expected navigation accuracy of the Space Sextant is known, the information content of the star-moon measurement can be compared with that of the star-

16

earth horizon observations produced by the matrix sensors, and the resulting relative accuracies will be indicative of matrix sensor performance.

2.2 Optical Satellite Navigation Covariance Program

To compare the navigation accuracies of the two types of optical sensors involved in this study, a computer program for performing covariance propagation and analysis was written. This program assumes only zero-mean Gaussian measurement errors are present and propagate the satellite state error covariance using the following Extended Kalman Filter (EKF) update scheme. The nonlinear model for the system is represented by

$$\dot{X} = F\big(X(t),t\big) \tag{2.1}$$

where the state vector, $X(t)$, has components measured in an inertial frame:

$$X(t) = \begin{bmatrix} x_1(t) \\ x_2(t) \\ x_3(t) \\ x_4(t) \\ x_5(t) \\ x_6(t) \end{bmatrix} = \begin{bmatrix} \overline{r}(t) \\ \overline{v}(t) \end{bmatrix} \tag{2.2}$$

and where the force function, $F(X(t),t)$, is defined as:

$$F(X(t),t) = \begin{bmatrix} \dot{\tilde{r}}(t) \\ \dot{\tilde{v}}(t) \end{bmatrix} = \begin{bmatrix} x_4(t) \\ x_5(t) \\ x_6(t) \\ \dfrac{-\mu x_1(t)}{r^3} + \tilde{P}_x(t) \\ \dfrac{-\mu x_2(t)}{r^3} + \tilde{P}_y(t) \\ \dfrac{-\mu x_3(t)}{r^3} + \tilde{P}_z(t) \end{bmatrix} \qquad (2.3)$$

where

μ = gravitation parameter of earth = 398603.2 km^3/sec^2,

r = the magnitude of the satellite position vector,

$$r(t) = \left(x_1^2 + x_2^2 + x_3^2 \right)^{1/2}$$

$\tilde{P}(t)$ is any perturbing force.

In this analysis, $\tilde{P}(t) = 0$, and the resulting orbit is two-body; however, the program can simulate any desired forces acting on the spacecraft by changing the derivative subroutine.

Between planned observation times, the state is propagated by either closed-form analytic integration for the two-body case or by a Runge-Kutta (RK4) or Adams predictor-corrector numerical integrator. The state error covariance matrix, P, is given at the start of the analysis as P_o at t_o and is propagated between observation times by

$$\overline{P}(t + \Delta t) - \Phi(t + \Delta t, t) \; P(t) \; \Phi^T(t + \Delta t, t) \tag{2.4}$$

where $\Phi(t + \Delta t, t)$, the state transition matrix, is approximated from a second-order Taylor series solution to

$$\dot{\Phi}(\tau, t) = A(\tau) \; \Phi(\tau, t); \quad \Phi(t, t) = I \tag{2.5}$$

where

$$A(\tau) = \frac{\partial F(X(\tau), \tau)}{\partial X(\tau)}$$

The approximate solution for $\Phi(t + \Delta t, t)$ is given by Murata [1982] as

$$\Phi(t + \Delta t, t) = I + A(t)\Delta t + \frac{1}{2} \left[\dot{A}(t) + A^2(t) \right] \Delta t^2 \tag{2.6}$$

where

$$\dot{A}(t) = \frac{A(t + \Delta t) - A(t)}{\Delta t} \tag{2.7}$$

At each simulated observation time, t_k , the covariance matrix is updated by the contribution of the type of observation assumed to be available at that time.

2.2.1 Measurement Model

At each measurement epoch, the covariance matrix is updated, and symmetry is enforced by the following algorithms:

$$P = (I - KH)\overline{P} \tag{2.8}$$

$$P := \frac{1}{2} (P + P^T) \tag{2.9}$$

where := is defined as "replaced by."

Once the H matrix is computed at each observation epoch, the Kalman gain, K, is given by

$$K = \bar{P}H^T\left(H\bar{P}H^T + R\right)^{-1} \tag{2.10}$$

where $R = \sigma^2$ for the sensor simulated at t_k. A complete derivation of Kalman continuous-discrete update and propagation algorithms is given by Jazwinski [1970], pp. 195-200.

For the purposes of the analysis conducted here, the covariance matrix is rotated from its original coordinate system, the earth-centered inertial (ECI), to an inertial coordinate system residing at the spacecraft, aligned with the instantaneous radial, tangential, normal (RTN) system. Figure 2.1 shows these coordinate systems and the measurement geometry simulated. The diagonal elements of P then form a 1σ error ellipsoid about the estimated spacecraft position. If $\left[T_{ECI}^{RTN}\right]$ is a 3 x 3 orthogonal transformation matrix from ECI to RTN coordinates, then

$$P_{RTN} = \begin{bmatrix} T_{ECI}^{RTN} & 0 \\ 0 & T_{ECI}^{RTN} \end{bmatrix} P_{ECI} \begin{bmatrix} T_{ECI}^{RTN} & 0 \\ 0 & T_{ECI}^{RTN} \end{bmatrix}^T \tag{2.11}$$

and the ellipsoid axes defined by the position sigmas

$$\sigma_{r_{rad}} = \left[P_{RTN_{11}}\right]^{1/2}$$
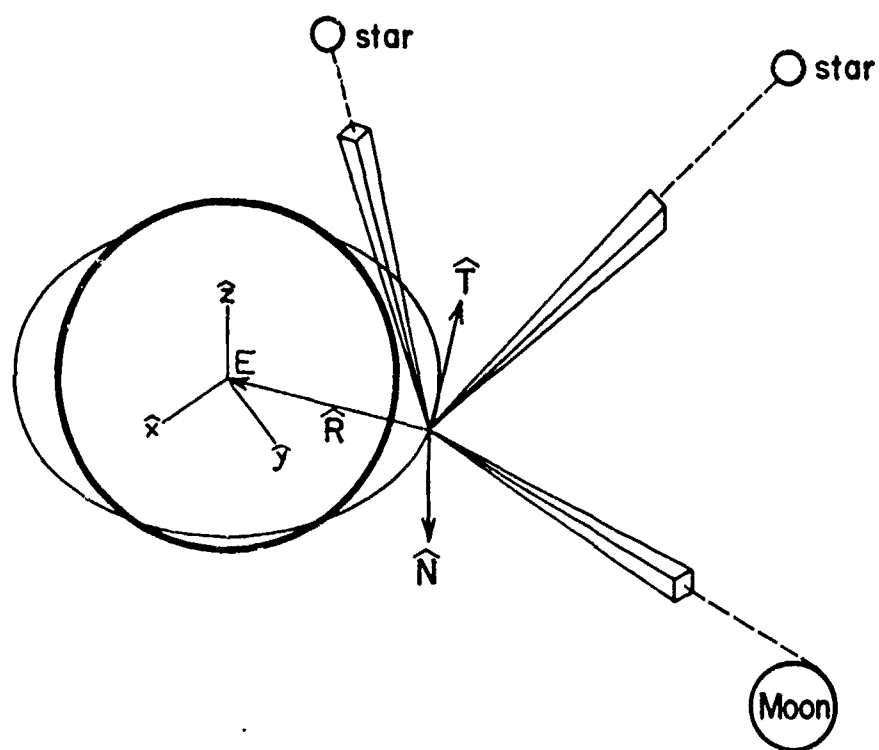
Figure 2.1. Spacecraft Sensor Orientation

$$\sigma_{r_{tan}} = \left[P_{RTN_{22}} \right]^{1/2} \qquad (2.12)$$

$$\sigma_{r_{nor}} = \left[P_{RTN_{33}} \right]^{1/2}$$

are related to the sensor-orbit geometry and are usually aligned with the largest axis along the T unit vector of the RTN system. The velocity error ellipsoid given by

$$\sigma_{v_{rad}} = \left[P_{RTN_{44}} \right]^{1/2}$$

$$\sigma_{v_{tan}} = \left[P_{RTN_{55}} \right]^{1/2} \qquad (2.13)$$

$$\sigma_{v_{nor}} = \left[P_{RTN_{66}} \right]^{1/2}$$

defines an instantaneous inertial velocity error located at the satellite but does not include terms associated with the angular velocity and acceleration of the RTN coordinate system itself.

The measurement sensitivity matrix, H , relates the difference between the measured and computed observations, $y = Y-Y*$, using an a priori estimate of the trajectory, to the error in the state $x = X - X*$. The covariance matrix P represents the uncertainty in the estimate of x. The structure of the measurement sensitivity matrix, H , will depend on the individual observation types. For the cases considered, H is given by:

$$H = \left[\frac{\partial \text{ measurement } (t_k)}{\partial X_k} \right] X_k = X_k^* \qquad (2.14)$$

2.2.1.1 Star-Horizon Geometry

For a star-horizon observation, Fig. 2.2 shows the geometry, with vectors and angles defined as follows. Let

$$\bar{r} = \begin{bmatrix} x_1 \\ x_2 \\ x_3 \end{bmatrix} \qquad (2.15)$$

and

$r = |\bar{r}|$

r_h = ray tangent altitude(RTA) + r_e

$\hat{s}$ = unit vector to star, defined by line-of-sight of sensor

       in inertial coordinates

Then,

$$a = \sin^{-1}\left(\frac{r_h}{r}\right) \qquad (2.16)$$

$$b = \cos^{-1}\left(-\frac{\bar{r} \cdot \hat{s}}{r}\right) \qquad (2.17)$$

$$ob = b - a \qquad (2.18)$$

and the first three components of the measurement matrix are
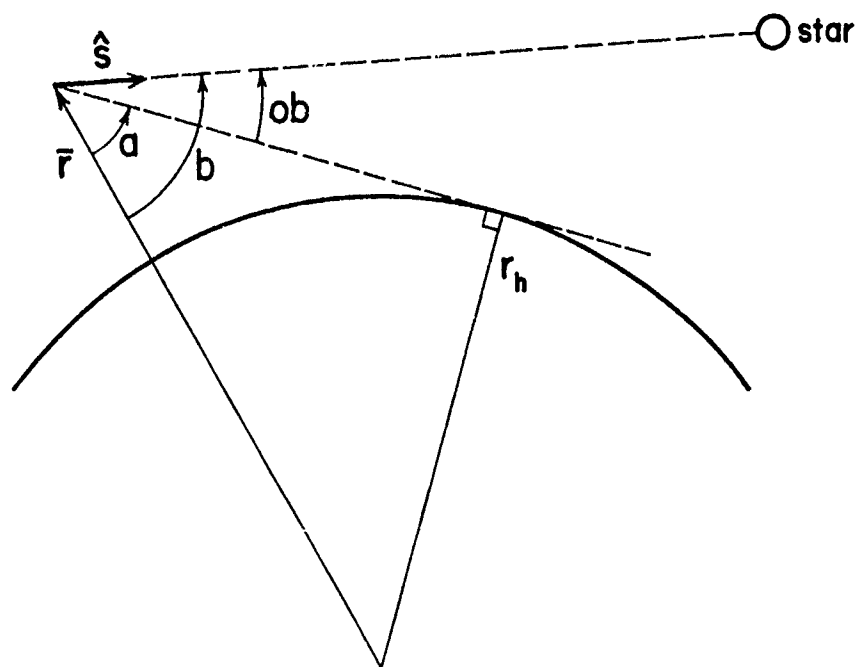
Figure 2.2. Star-Horizon Geometry

$$H_{1,2,3} = \left[1 - \left(\frac{\overline{r} \cdot \hat{s}}{r} \right)^2 \right]^{-1/2} \left[\left(\frac{\hat{s}}{r} \right) + \frac{(\overline{r} \cdot \hat{s})\overline{r}}{r^3} \right]$$

$$+ \left[1 - \left(\frac{r_h}{r} \right)^2 \right]^{-1/2} \left(\frac{r_h}{r^3} \right) \overline{r}$$

$$= \csc b \; \frac{\hat{s}}{r} + \frac{(\overline{r} \cdot \hat{s})\overline{r}}{r^3} + \sec a \; \frac{r_h}{r^3} \; \overline{r} \qquad (2.19)$$

while the second three components are

$$H_{4,5,6\ldots} = 0 \qquad (2.20)$$

2.2.1.2 Horizon Sensor Geometry

For a horizon observation, the simulated star direction is assumed to be in the plane defined by the center of the earth, the spacecraft and the line-of-sight of the same star sensor simulated in the star-horizon observation. The unit vector $\hat{s}$ is replaced by a unit vector pointing to the intersection of this plane and the surface of the earth's atmosphere as given by an input tangent height. The new value for $\hat{s}$ is

$$\hat{s} := \frac{1}{\sin(b)} \left[\sin(a) \; \hat{s} - \sin(ob) \; \frac{\overline{r}}{r} \right] \qquad (2.21)$$

and the partial derivative matrix, H , is the same as above.

2.2.1.3 Star-Moon Geometry

A star-moon observation is defined as shown in Fig. 2.3, with the observation being the acute angle between the lunar limb
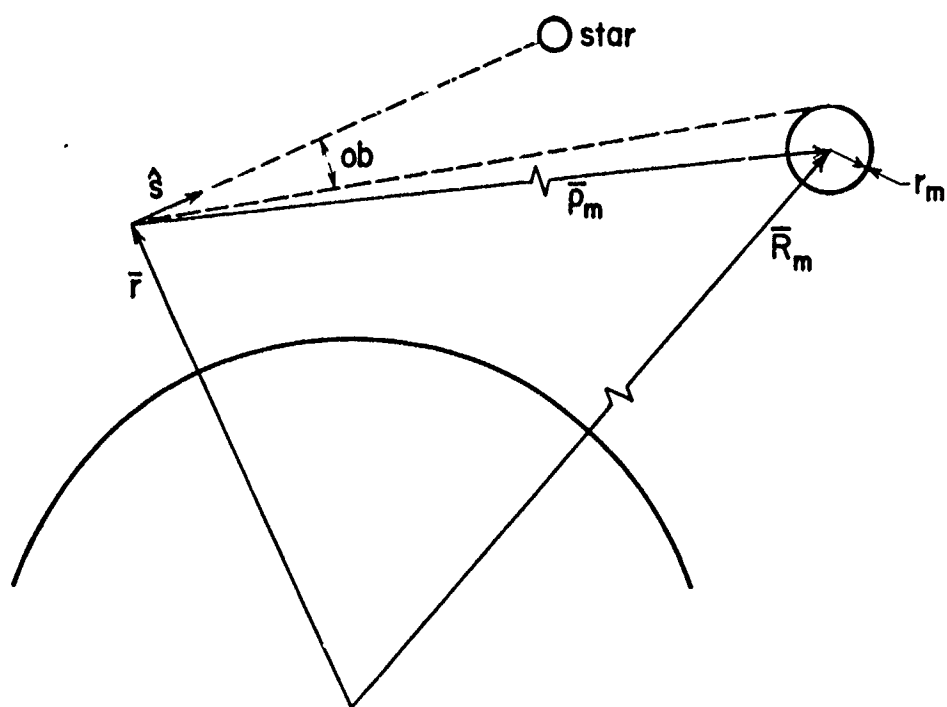
Figure 2.3. Star-Moon Geometry

nearest a star and that star.

$$ob = \cos^{-1}\left[\frac{\hat{s} \cdot \bar{\rho}_m}{\rho_m}\right] - \sin\left[\frac{r_m}{\rho_m}\right] \qquad (2.22)$$

and

$$H_{1,2,3} = \left[1 - \left(\frac{\hat{s} \cdot \bar{\rho}_m}{\rho_m}\right)^2\right]^{-1/2} \left[\left(\frac{\hat{s}}{\rho_m}\right) - \left(\frac{(\hat{s} \cdot \bar{\rho}_m)\bar{\rho}_m}{\rho_m^3}\right)\right]$$

$$- \left[1 - \left(\frac{r_m}{\rho_m}\right)^2\right]^{-1/2} \left(\frac{r_m}{\rho_m^3}\right)\bar{\rho}_m \qquad (2.23)$$

$$H_{4,5,6} = 0 \qquad (2.24)$$

2.3 Star-Moon Sensor Performance

The space sextant uses star-moon angles for input to a navigation filter because the earth horizon cannot be accurately determined by current infra-red and visible sensor technologies. Since the sextant telescopes can gimbal freely with respect to each other and with respect to the spacecraft, one can normally track the bright lunar limb while the other locks on stars visible to the system. This allows a more precise angle measurement than is possible with a current earth horizon sensor. In the situations of lunar occultation by the earth or sun-moon interference, the sensor tracks the earth horizon as a temporary replacement for the moon. The sensor's independence of motion gives it the advantage of being

able to track known targets, even when the spacecraft is unstable in attituae and also frees the navigation solution from attitude errors.

The space sextant type of observation was simulated by computing the angle between unit vectors to the nearest lunar limb and stars at ±45° from the spacecraft T unit vector in the local horizon plane. As shown in Figure 2.4, the resulting navigation error exhibits a large twice-per-orbit periodic effect. This is due to the orbit-moon geometry and, for various initial moon-ascending node angles, exhibits varying amplitudes. The case with minimum periodic amplitude $(\Omega = 73.4°)$ was then used for the star-moon accuracy curves in the main report to maintain as much consistency as possible in the error vs. period plots.

This twice-per-orbit fluctuation is due to the particular simulation geometry used -- two fixed star directions relative to the spacecraft. To more closely simulate the Space Sextant scanning scheme, as described by Martin-Marietta [1981], another mode was programmed in which the star unit vector was changed randomly between 0° and 360° in right ascension and between -90° and +90° in declination for each consecutive simulated measurement. The results (Fig. 2.5) show a random pattern in position error after convergence of the filter. This random behavior would adversely affect the consistency of results when various period orbits are considered, so the original sensor configuration with $\Omega = 73.4°$ was retained in the
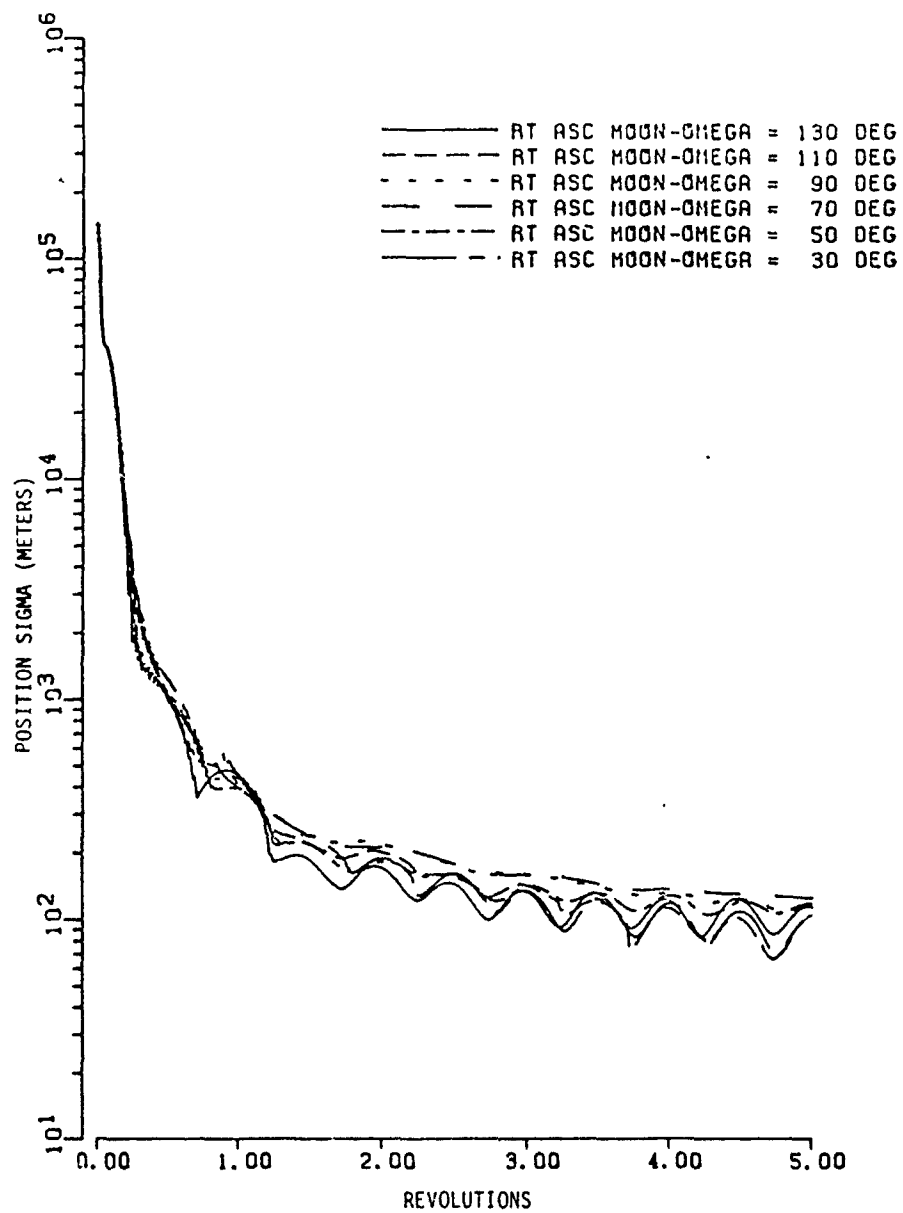
Figure 2.4. Navigation Error for Space Sextant as a
Function of Ascending Node-Moon Angle
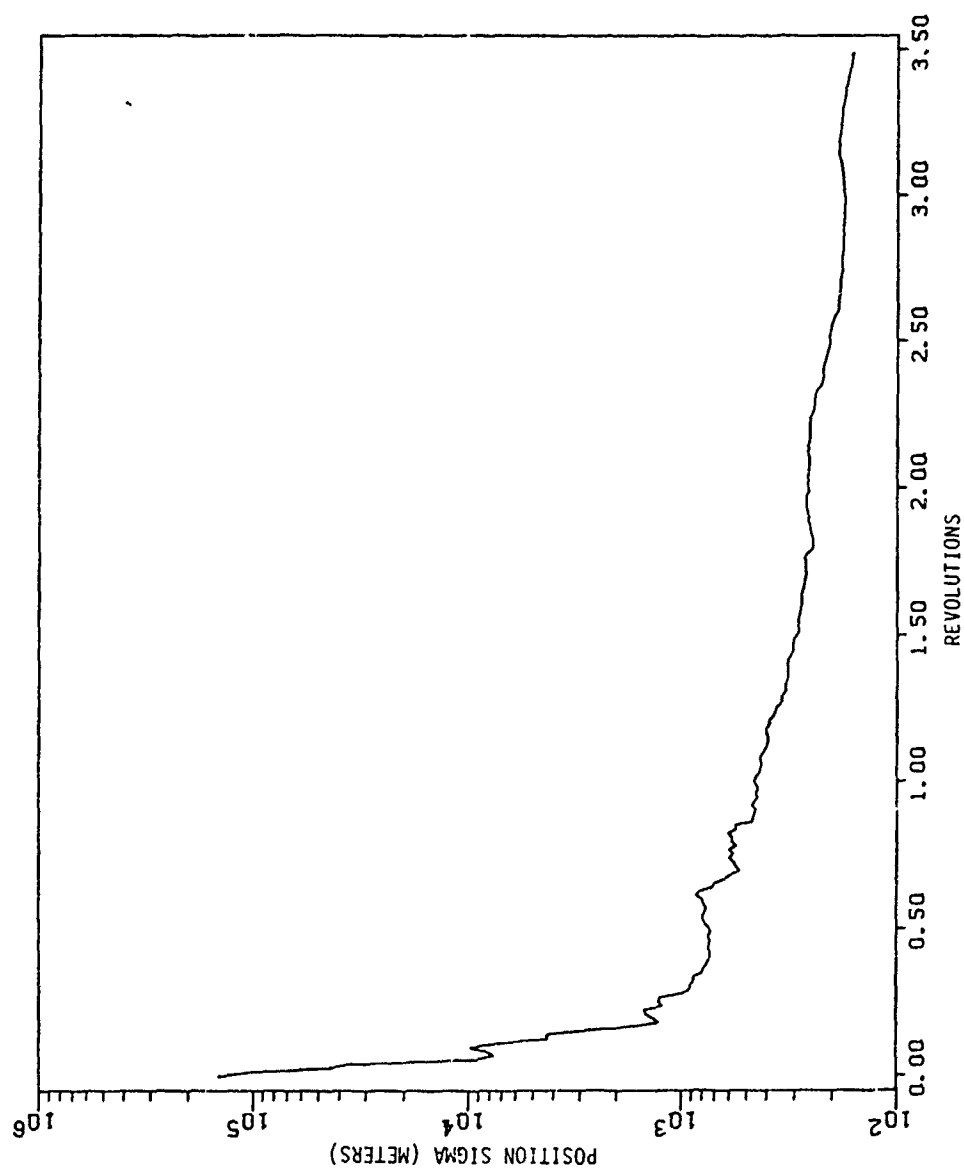
Figure 2.5. Navigation Error for Space Sextant Using
Randomly Selected Stars

analysis.

2.4 Star-Horizon Sensor Performance

The solid-state modular sensors (MADAN, Digistar and STELLAR) are designed to be rigidly fixed to the spacecraft and, therefore, cannot observe the lunar limb except when it happens to fall in the field of view. Optical celestial navigation from a spacecraft, however, requires the measurement of angles between a star and a body that appears to move as the vehicle moves in its orbit. This rules out star-star angles except for attitude information. One sensor must observe a near celestial body and, for earth-oriented spacecraft, the earth horizon is the only feasible target for fixed sensors. Also, since the earth horizon appears to move 360° during each orbit while the moon appears to move $2 \tan^{-1}(r/R_m)$ (12.6 deg for sync orbit), the earth-star angle is much more sensitive to orbit dynamics. Furthermore, since the earth horizon is normally closer to the spacecraft than the moon horizon, the earth-horizon based measurement should give a higher navigation accuracy for angle measurements of comparable precision.

For near-term conventional horizon sensors, the state of the art is about .02° [Fowler, 1981]. Figure 2.6 shows the results obtained in the covariance analysis for both star-earth and star-moon sensors. The covariance analysis program propagates the state covariance matrix and updates this matrix with information obtained from each type of observation at fixed-time intervals. The

resulting RSS position sigma from the diagonal terms of the covariance is plotted versus time expressed in orbits, with the solid line representing a one-sigma error for star-horizon measurements obtained from a 2 arcsec star sensor and a .02 deg horizon sensor. The dashed line represents the one-sigma error for a Space Sextant measuring star-moon limb angles to a .5 arcsec precision. For the star-earth measurement, the earth's horizon is sensed, and for a star-moon angle, the moon's bright limb is sensed. Two horizon sensors with .02° accuracy capability, when used with two fixed star sensors with a precision of 2 arcsec, would provide a navigation accuracy of 2500 meters for a satellite in a 12-hour circular orbit. As seen in Fig. 2.6, this is more than a factor of 10 worse than that achievable by a space sextant with a precision of .5 arcsec. Thus, to take advantage of the improved measurement-orbit geometry, the solid state star sensors must be coupled with horizon sensors of at least an order of magnitude improvement: 0.002° or 7 arcsec.

2.4.1 Star Refraction Measurement of Earth Horizon

Fortunately, the new star sensors themselves offer a means by which earth-horizon sensing may be improved. As starlight passes through the atmosphere, it is refracted and dispersed. The angles of refraction and dispersion depend upon ray tangent altitude (RTA), the point where a starlight ray is nearest to the earth's surface as shown in Figure 2.7, and atmospheric conditions, but the measurement
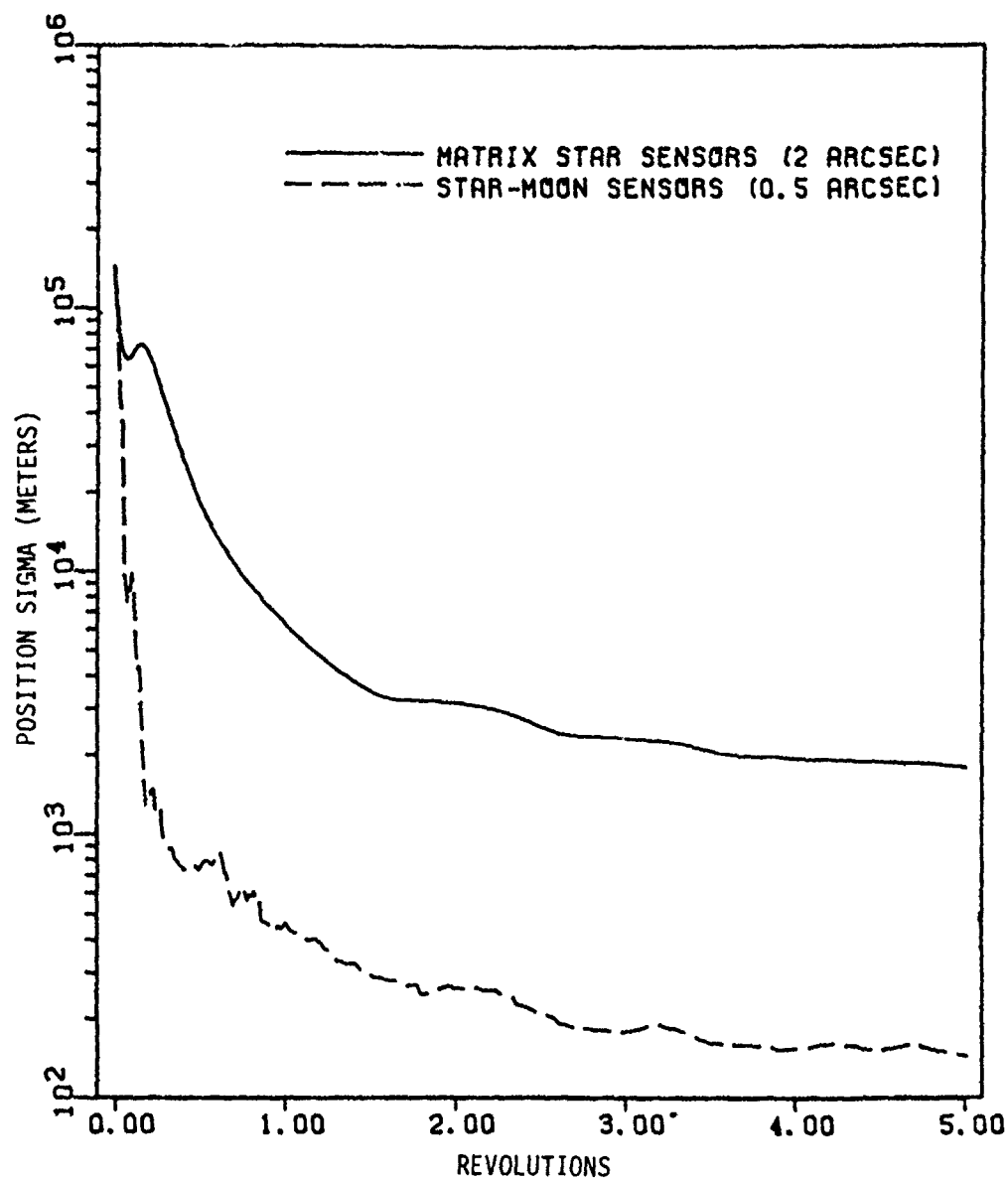
Figure 2.6. Navigation Error for 12h Circular Orbit; Earth-
Horizon Sensor Precision = 0.02°
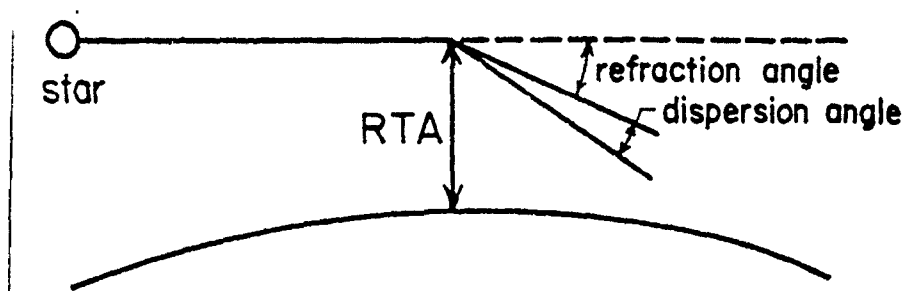
Figure 2.7. Starlight Ray Geometry

of either of these angles offer the possibility of a more accurately defined horizon. The Office of Naval Research is presently investigating the feasibility of using the dispersion sensor SHAD, for mid-course ICBM guidance, with an expected 1σ error of 65 meters [Quell, 1981], while Chambers [1981] of the Aerospace Corporation proposes measuring refraction using the unique capabilities of MADAN. Since this sensor has a wide field of view (7.1° square), a minimum of two stars can be observed continuously. By measuring the angle between two stars before and during the time one of them is refracted by the atmosphere due to spacecraft motion, the refraction angle inferred from this changing geometry defines the height of starlight tangency to the atmosphere (RTA). According to Chambers, a 3 arcsec knowledge of this refraction angle, obtained by looking at two stars to a precision of 2 arcsec each, gives a tangent height uncertainty of 150 meters for a tangent height of 25 km. Since this uncertainty depends upon a priori knowledge of the properties of the atmosphere and sensor and not on orbit altitude, the resulting apparent horizon determination precision varies from 16.7 arcsec for a 90-minute orbit to .72 arcsec for a geosynchronous orbit. Figure 2.8 from Chambers [1981] shows that the refraction curve has a fairly consistent slope for all models considered such that a given refraction error produces the same tangent height error for each curve. In addition, this tangent height error is only a function of refraction error, and refraction error is a function of
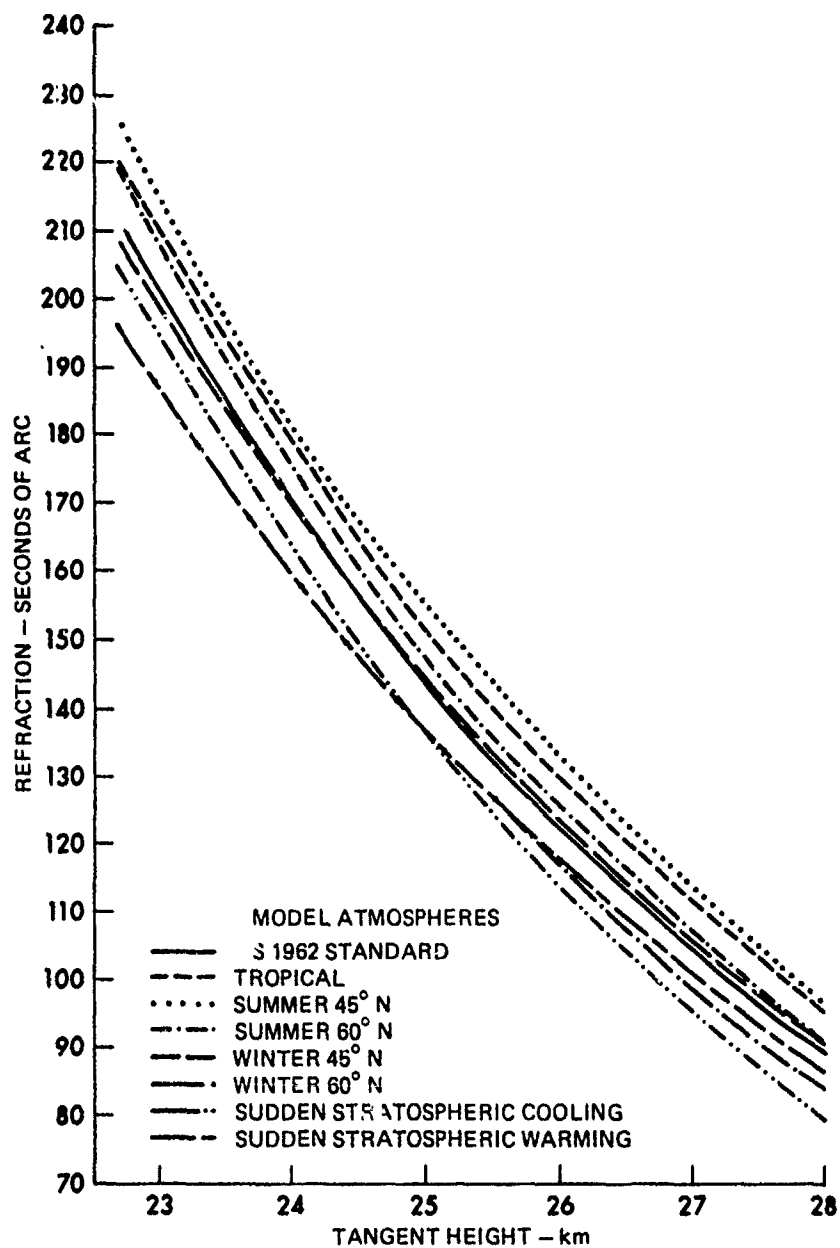
Figure 2.8. Atmospheric Refraction Versus Tangent Height
at 7000°A

the optical measurement device, not orbit altitude.

When the solid-state sensors are used as horizon sensors, they can either be combined with other similar devices to provide star-horizon data or they can be employed alone, with a priori knowledge of the angular position of the stars being observed, to give the angle between the horizon and the center of the earth. Fig. 2.9 shows the navigation accuracies expected from two star-horizon sensors, two horizon sensors and two star-moon sensors in a 12-hour circular orbit with the following instrument precision:

Sensor	Instrument Precision (1σ)
Star-horizon sensors	
Star:	2 arcsec
Horizon:	3 arcsec
Horizon sensors	3 arcsec
Star-moon sensors	.5 arcsec

Note that, even with a four- to six-fold decrease in observation precision, the star-horizon and horizon sensor navigation errors are two to seven times smaller than those predicted for the star-moon sensor. If the horizon sensors are an order of magnitude worse $(1\sigma = 30$ arcsec), the star-horizon and horizon sensor navigation errors grow to 350 m and 230 m, respectively.

2.4.2 Star-Horizon Performance vs. Sensor Orientation

To determine the optimum sensor configuration for two star sensors, the sensor bore-sight direction was first moved in azimuth
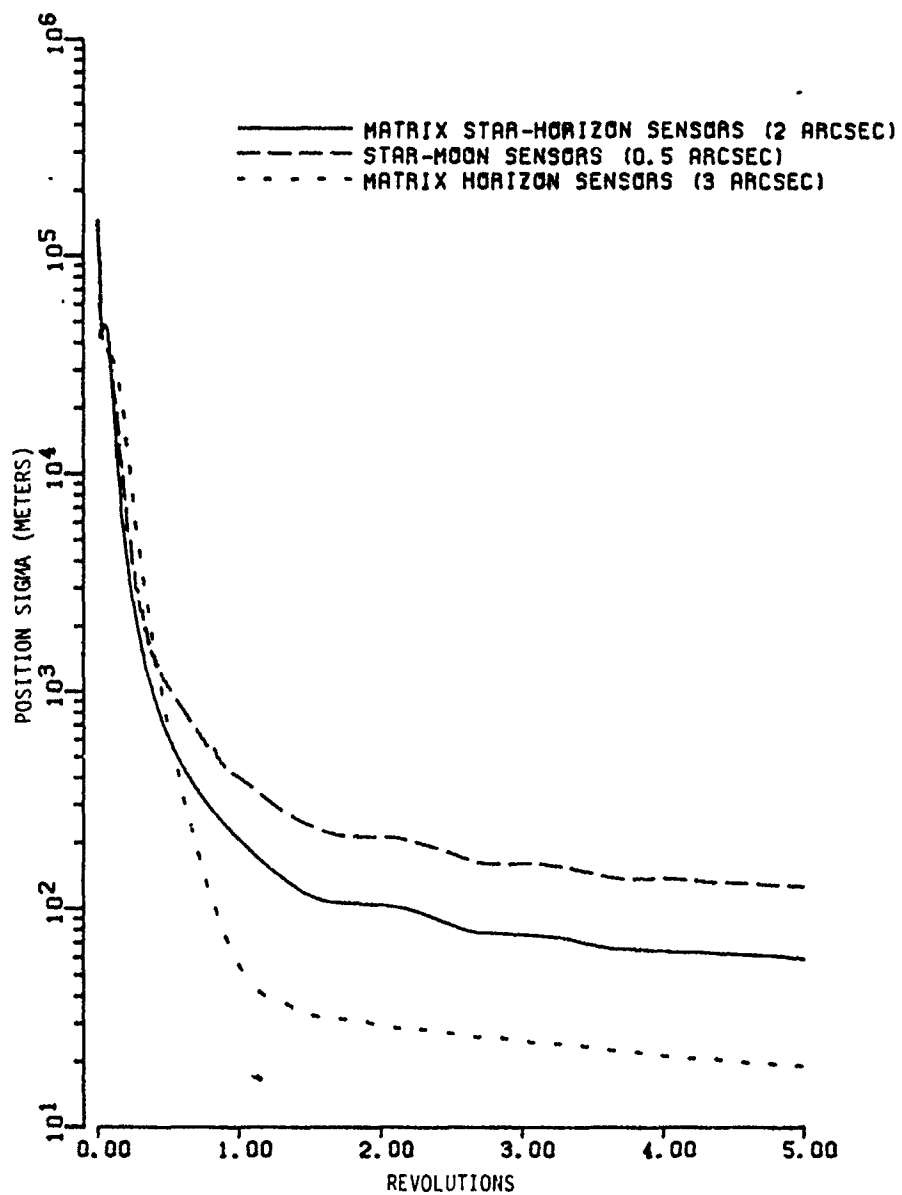
Figure 2.9. Navigation Error for 12 h Circular Orbit
Earth-Horizon Sensor Precision = 3 arcsec

in the local horizon plane and then in elevation for a 90-minute and a 12-hour orbit. Figures 2.10 and 2.11 show the effect of azimuth in the 90-minute and 12-hour orbits, while Figures 2.12 and 2.13 examine the effect of elevation in the two cases.

From the figures it is seen that, for high-altitude orbits, sensors located between 45° and 50° azimuth and as low an elevation as possible give the best results. The lowest elevation possible coincides with the horizon sensors themselves; thus, the horizon sensors alone produce the best navigation accuracy in the absence of attitude errors. While the 90-minute orbit was fairly insensitive to azimuth changes, it seems to be more sensitive to elevation angle than does the 12-hour orbit. Interestingly, a very high elevation star sensor gives improved performance in low orbit, and in fact, the test program that led to PADS had a star sensor pair mounted 60° from the local horizon, one at 0° azimuth and the other at 180° [Honeywell, 1973].

Since performance over the period range 90 min to 5 days is of interest to this study, the star sensor configuration selected for comparison with the other optical measurements in this analysis was one with star sensors located on the spacecraft in the local horizon plane, ± 45° from the T unit vector.

2.5 Optical Sensor Performance vs. Circular Orbit Period

Fig. 2.14 through 2.15 show the performance of the optical sensors as a function of altitude or period. While the star-horizon
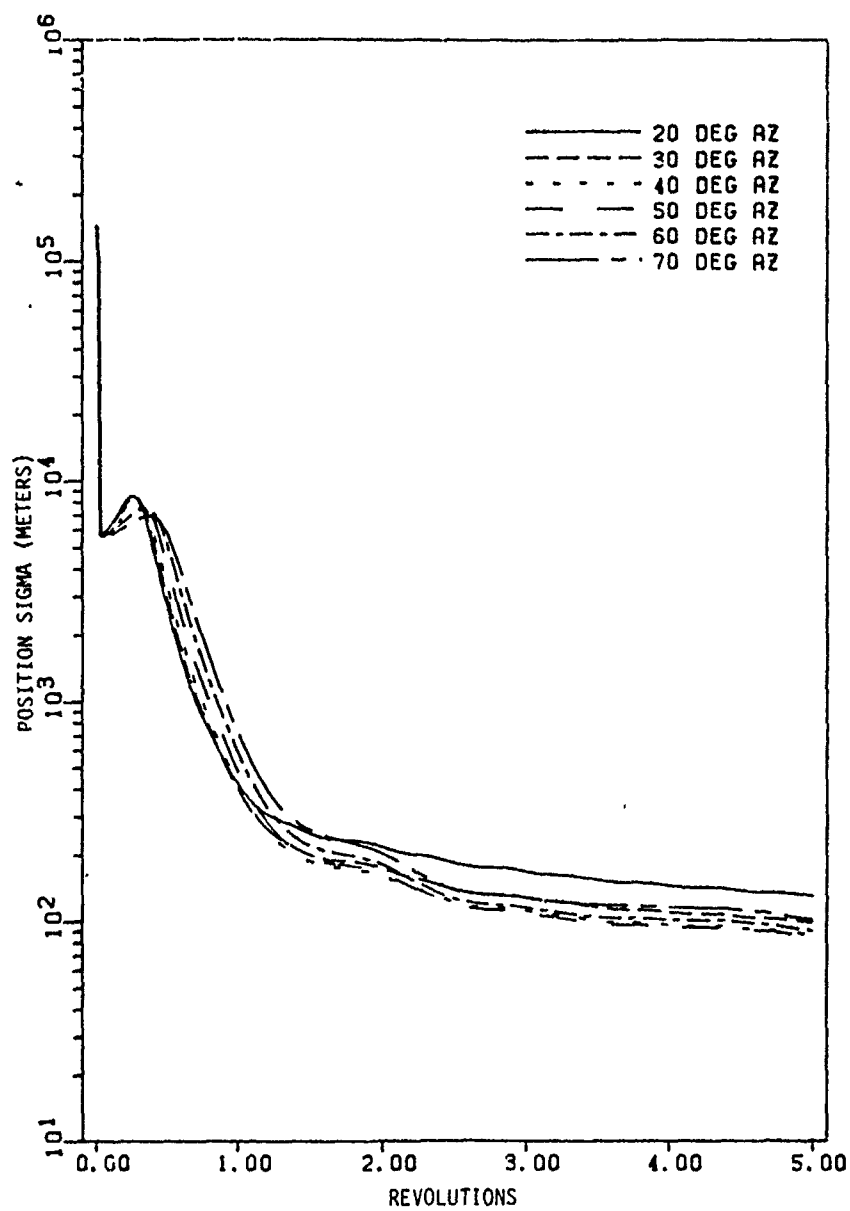
Figure 2.10. Navigation Error vs. Sensor Azimuth
90 min Circular Orbit, Star-Horizon Sensors
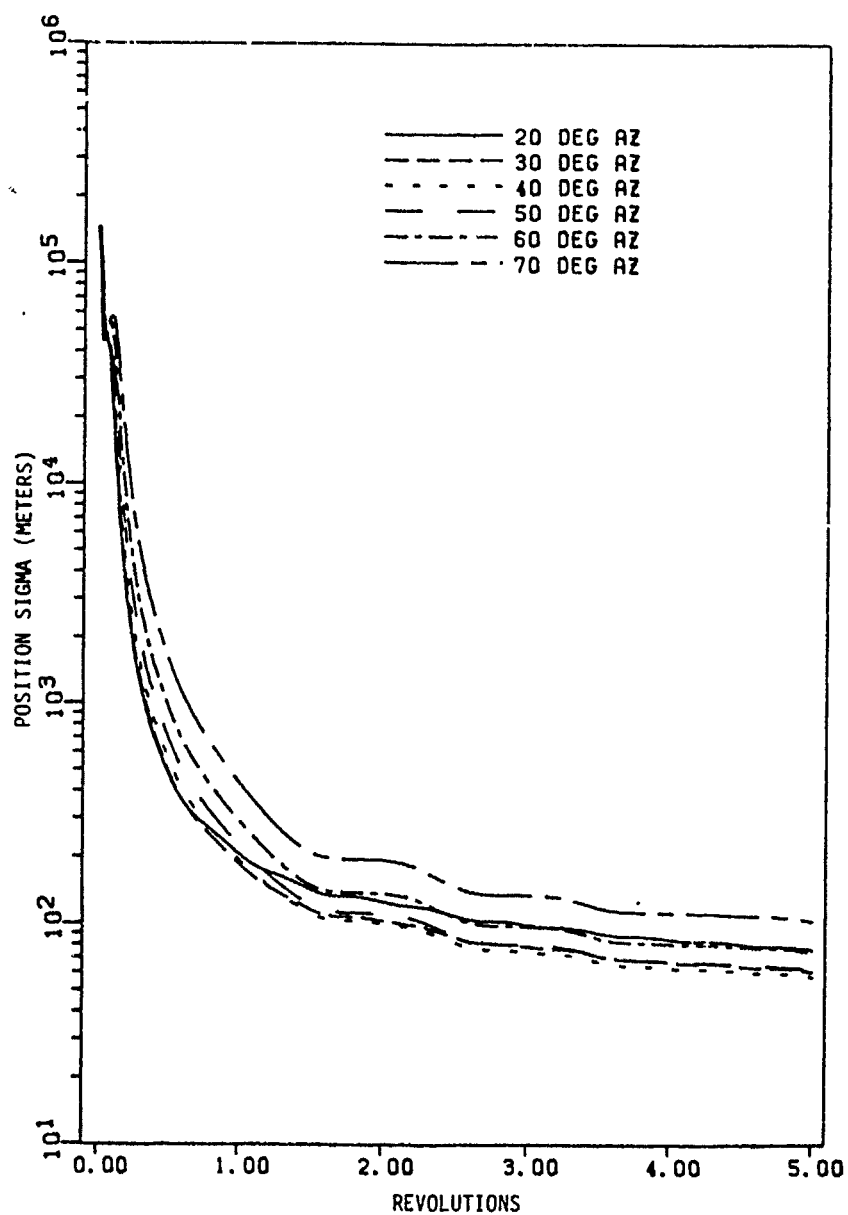
Figure 2.11.   Navigation Error vs. Sensor Azimuth 12 h
Circular Orbit, Star-Horizon Sensors
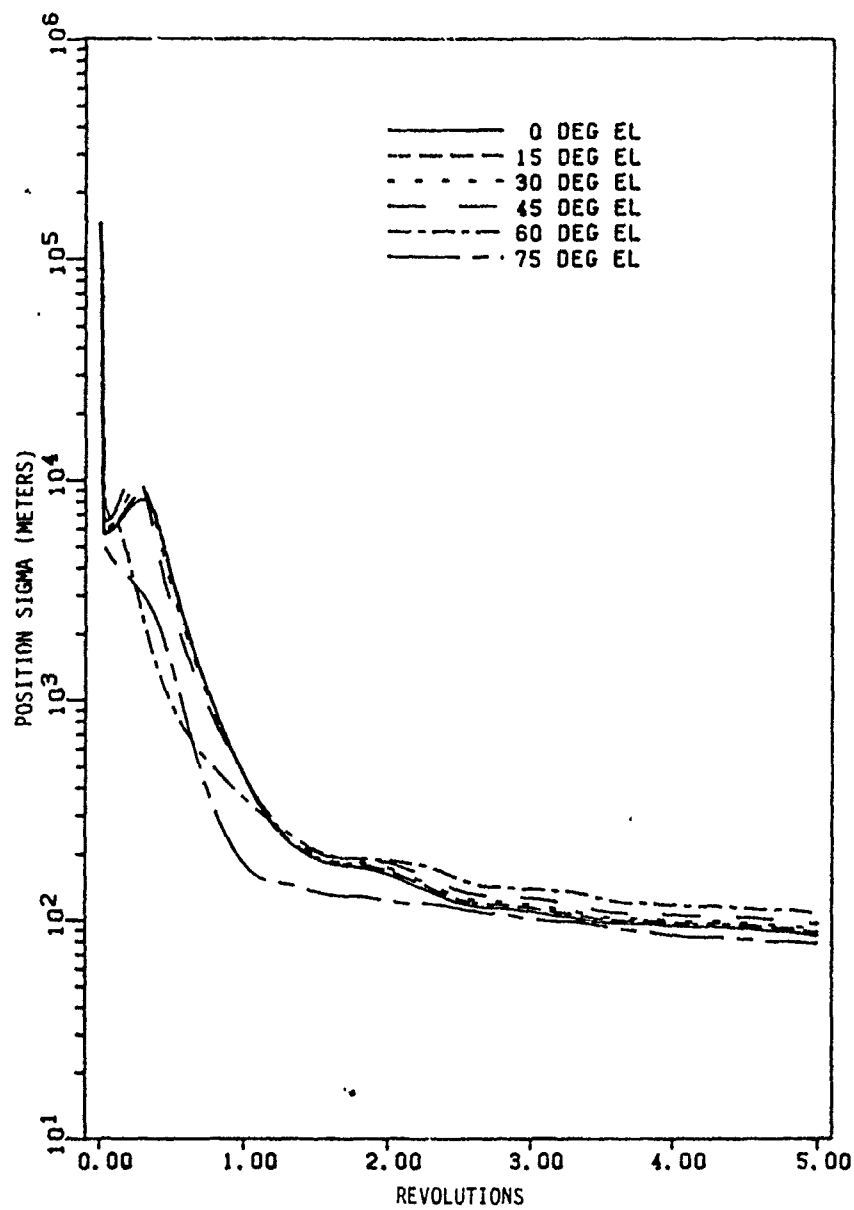
Figure 2.12. Navigation Error vs. Sensor Elevation
90 min Circular Orbit, Star-Horizon Sensors
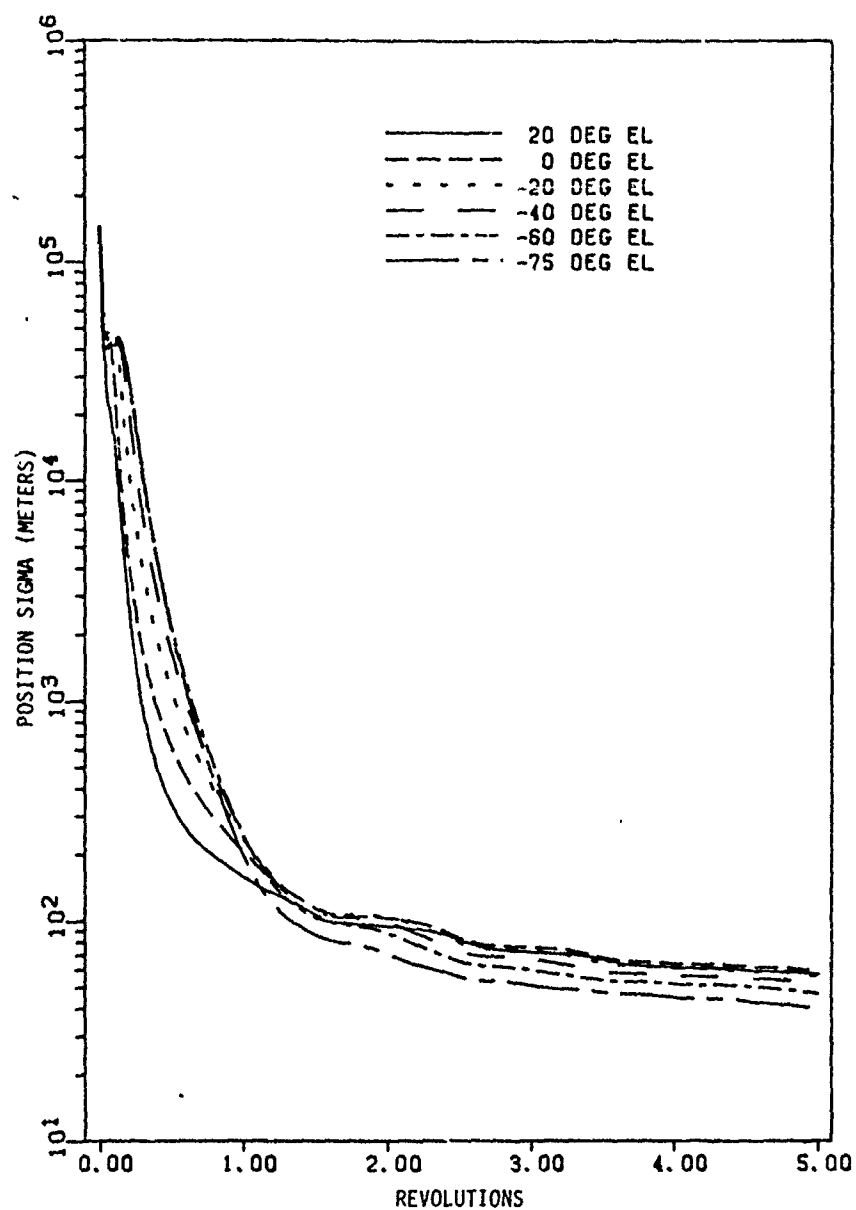
Figure 2.13. Navigation Error vs. Sensor Elevation
12 h Circular Orbit, Star-Horizon Sensors
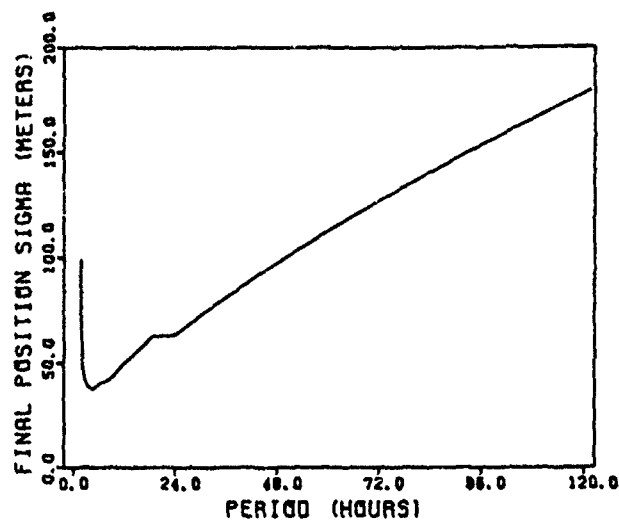
(a)

STAR-HORIZON SENSORS (2 arcsec)
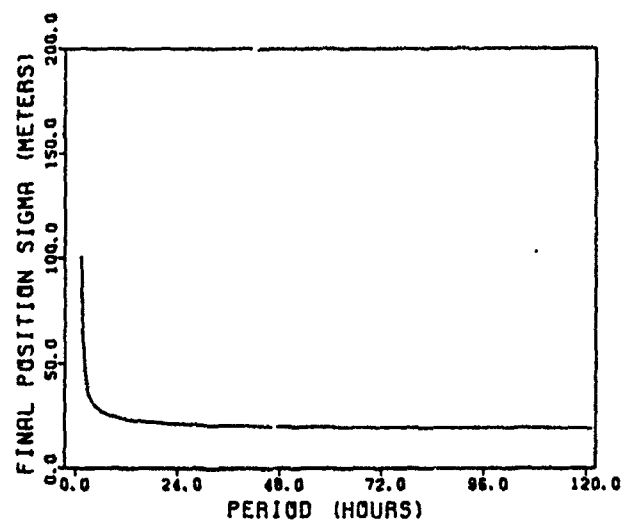
(b)

HORIZON SENSORS (3 arcsec)

Figure 2.14. Navigation Error vs. Period of a Circular
Orbit for Horizon Sensors (3 arcsec)
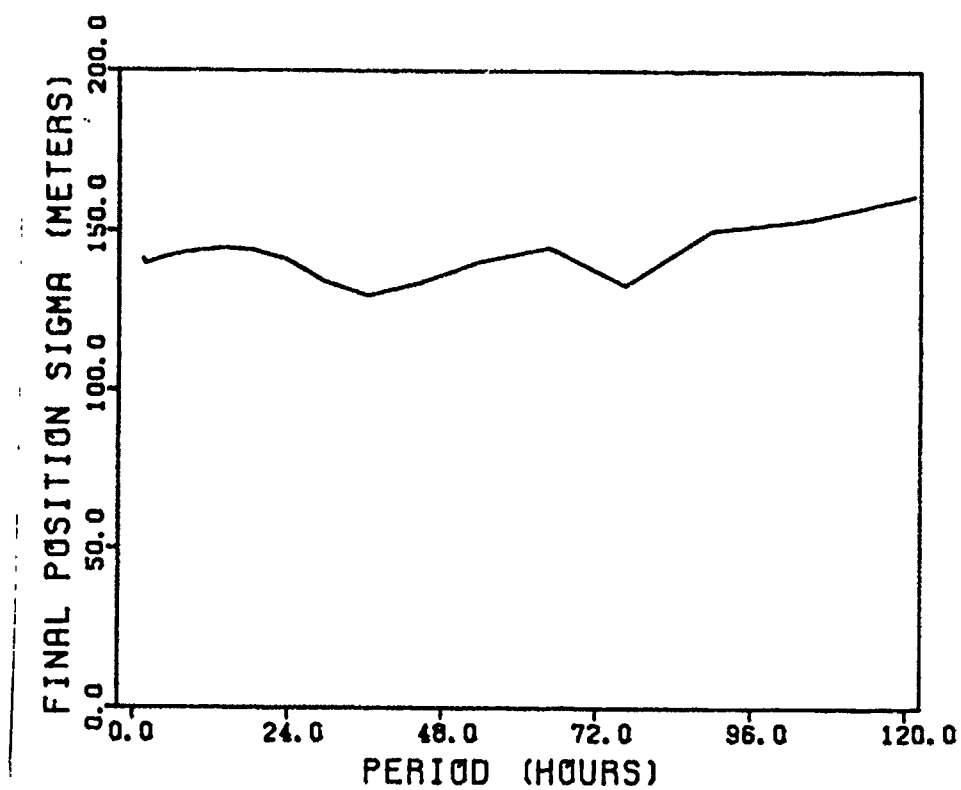
Figure 2.15.   Navigation Error vs. Period of a Circular
              Orbit for Star-Moon Sensors (0.5 arcsec)

sensor shows an error growth with altitude due to the changing geometry, the space sextant exhibits an almost constant error. This is due to the distance of the moon being so much greater than the satellite radius. The horizon sensor shows the interesting feature of a sharp drop in position uncertainty followed by nearly constant performance as the altitude increases. For a constant sensor error, the navigation performance would be expected to degrade with increasing altitude, as for the star-horizon sensor. However, the horizon sensor's apparent precision due to a constant 150 meter tangent height uncertainty (o_h), falls rapidly at low-to-medium altitudes and then drops more slowly as altitude increases (Fig. 2.16). Note that the increase in apparent sensor precision parallels the navigation performance seen in Fig. 2.14b, i.e., as altitude increases from near-earth orbits, the rapid improvement in apparent sensor precision leads directly to corresponding improvements in navigation accuracy. These results show that if the earth horizon can be tracked to o_h ≈ 150 m, two horizon sensors can provide much better navigation accuracies than the space sextant. If the horizon detection is accurate to only 1500 m, the resulting navigation error increases to 234-350 m for a 12-hour orbit, depending upon the mode used (horizon only or star-horizon).

2.6 Sensor Performance on an Elliptical Orbit

Figure 2.17 shows the performance of the three measurement types applied to a 12-hour elliptical orbit (e ≈ .75) with sensors
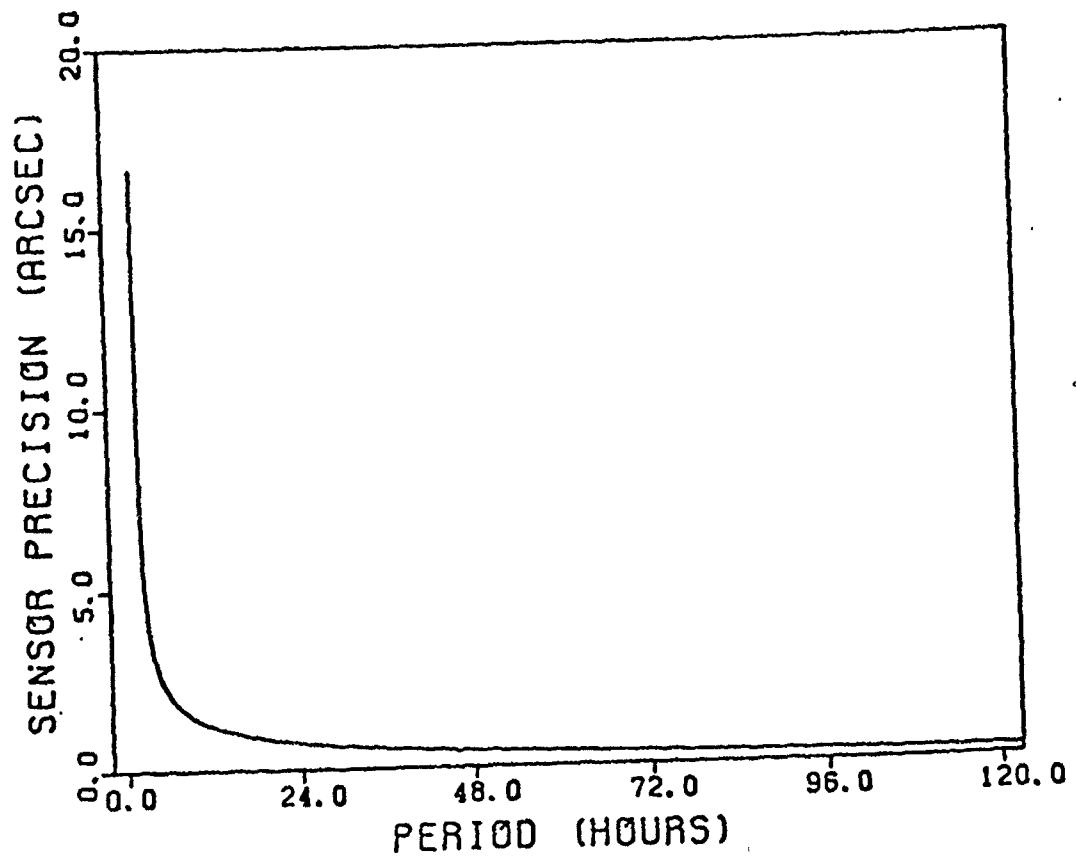
Figure 2.16. Apparent Horizon Sensor Precision vs. Period of a Circular Orbit
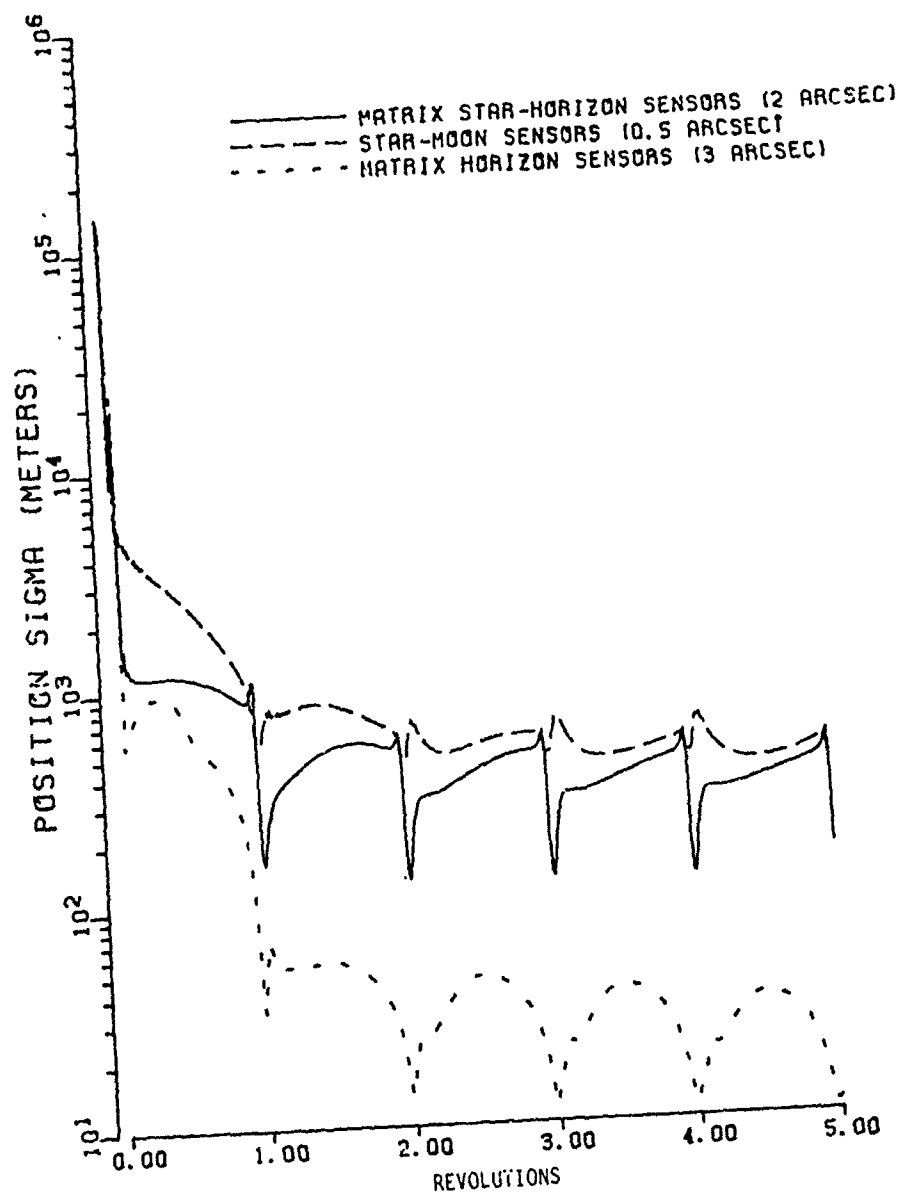
Figure 2.17. Navigation Error for 12 h Orbit, ECC = 0.75
Earth-Horizon Sensor Precision = 3 arcsec

at ± 45° azimuth and 0° elevation. The horizon sensor must be gimbaled, however, and the gimbal mechanism would introduce some error in the horizon definition.

Comparing these results to Figure 2.9, it is seen that the relative order of sensor performance stays the same when applied to an elliptic orbit, but the error magnitude grows, especially for the star-horizon sensor pair. This error growth could be reduced by selecting a lower elevation sensor direction as altitude is increased, but that would lead to a much more complicated system unless the star and horizon sensor pair were mounted on the same gimbaled platform. If that were the case, the relative orientation of the two sensors would remain the same, and gimbal inaccuracies could probably be reduced considerably.

2.7 Comparative Sensor Performance for Circular Orbits

The results of this analysis are summarized in Table 2.1, where the matrix sensors are operated in either the star-horizon angle mode or as horizon sensors alone. The navigation accuracies are representative of orbits above 300-minute period.

TABLE 2.1

PREDIC ED NAVIGATION ERROR DUE TO SENSOR ERROR

Sensor	Sensor Precision (arcsec)	Navigation Error (meters)
Space Sextant	.5	150
Matrix Sensors		
Star-Horizon	2	40-180
	1	19-90
	.5	9-45
Horizon	2	20
	1	11
	.5	6

It should be emphasized that only sensor error was considered and that the fixed sensor's results would be degraded by attitude errors. This is especially true for the horizon sensor, since the vehicle-determined local vertical forms the measurement reference. Note that the optical sensors may also form the attitude determination sensor system, as indicated in the proposed utilization of the space sextant. Correlation between attitude and navigation solutions may be a problem, but since the attitude filter requires high frequency updates while the navigation filter may require less frequent update, the two requirements may be handled as two separate problems as long as the navigation system is aware of the time history of the attitude solution.

2.8 Refraction Errors

The largest error sources inherent in the star-earth

horizon measurement of star refraction are the sensor itself and the atmospheric modeling required to predict refraction angles. In studies recently completed for the Naval Surface Weapons Center (NSWC) by Clynch [1979 and 1981b], a ray tracing program was used to compute refraction of a star ray passing through earth's atmosphere. The model for refractivity was from Owens [1967] where the refractivity, N, is a function of the refractive index,

$$N \equiv 10^6(n-1) \tag{2.25}$$

but the refractive index, n, of a gas must be determined by the molecular density and relative polarizability. This refractive index is obtained from the Lorentz-Lorenz equation,

$$\frac{n^2-1}{n^2+2} = \hat{R}_1\hat{\rho}_1 + \hat{R}_2\hat{\rho}_2 + \ldots + \hat{R}_i\hat{\rho}_i + \ldots = \sum_i \hat{R}_i\hat{\rho}_i \tag{2.26}$$

where $\hat{R}_i$ and $\hat{\rho}_i$ are the specific refractivity and density of the ith component. Assuming that dry, CO_2-free air can be treated as single component, equation (2.26) can be approximated by

$$\frac{n^2-1}{n^2+2} = \hat{R}\,\hat{\rho} \tag{2.27}$$

From (2.27), it is seen that

$$n^2 = \frac{1 + 2\,\hat{R}\,\hat{\rho}}{1 - \hat{R}\,\hat{\rho}} \tag{2.28}$$

Thus,

$$N = 10^6 \left[\left(\frac{1 + 2\,\hat{R}\,\hat{\rho}}{1 - \hat{R}\,\hat{\rho}} \right)^{1/2} - 1 \right] \qquad (2.29)$$

Note that $\hat{R}$ in Eq. (2.29) is a constant for a homogenous dry air mixture, but that density, $\hat{\rho}$, is not a constant nor is it a well-behaved function of altitude. Density is usually modeled as an exponential function of altitude,

$$\hat{\rho} = \hat{\rho}_0\, e^{-a/H_s} \qquad (2.30)$$

where

$\hat{\rho}_0$ = bottom altitude density

a = altitude

H_s = scale height

but this exponential model breaks down when attempting to model large altitude bands. To extend the range of the equation, the altitude is broken into several altitude bands of constant thickness. The constants in Eqs. (2.29) and (2.30), $\hat{R}$, $\hat{\rho}_0$ and H, also vary as a function of location and of local weather conditions; thus, location errors and delays result in errors in computed refraction index and thus in the computed refraction angle for a given ray altitude. The computed refraction angle, θ, in a slab is given by a continuous form of Snell's law in the case where a slab is defined as a region in which n has a small, constant gradient

[Kelso, 1964]

$$n \sin \theta = \text{constant} = n_o \sin \theta_o \qquad\qquad (2.31)$$

The computer program used by Clynch propagates the starlight through the atmosphere and, by constructing a series of slabs of constant refractive index gradient, computes the bending of the ray as it moves from one slab through another. In this analysis, the log of density vs. altitude data obtained from the National Oceanic and Atmospheric Administration were fit with cubic polynomials with an average relative error of 0.5 percent. When these models were then used to predict atmospheric density and then RTA (Fig. 2.7), it was found that the error in RTA was approximately proportional to the relative error in density at the ray tangent point with a 1 percent density error producing a 100 m RTA error. When data one to four days apart were processed, the results showed the effect of data aging. Table 2.2 lists typical errors of $\Delta\rho/\rho$ for several one- and four-day spans in 1979. These values are computed near the north pole, and latitudes below which density changes of ≤ 5 percent were observed are indicated. Winter pole density errors are very large compared to summer, but the error quickly drops as warmer weather approaches. Even in the worst month, however, 5 percent error or less is observed over approximately 60 percent of the earth's surface.

TABLE 2.2

EFFECT OF ATMOSPHERIC DATA AGEING AT 20 KM ALTITUDE

Date	Age (Days)	$\Delta\rho/\rho$ (%)	Latitude
9 Jan	1	7.5	40°
12 Jan	4	27.5	40°
21 Jun	4	4.4	90°

Clynch states that when data are aged for five days or more, they are comparable to climatology predictions; thus, density predictions covering the quiet 60 percent of the earth should be accurate to approximately 5 percent.

These errors are those expected from a complex ray tracing computer program operating with aged atmospheric data. In the onboard navigation scenario, it is not possible to implement this ray tracing algorithm, and a reduced order model must be used that includes an atmosphere generated onboard with a minimum of updates. Clynch [1981a] proposes an approximation to the ray path that matches the actual density and density gradient only at the ray tangent point (RTP). Altitude (a) near the RTP is approximated as a function of distance from the RTP, (s), by

$$a - RTA \cong \frac{s^2}{2r_r} \qquad (2.32)$$

where

$$r_r = R_e + RTA$$

The refraction angle θ is then expressed as the integral over the path length

$$\theta(RTA) = \int_{-\infty}^{\infty} \frac{d\theta}{ds}\, ds. \tag{2.33}$$

The actual path length derivative $d\theta/ds$ is a function of conditions in each slab, but when the actual optical path is replaced by a straight line through the RTP and tangent to the ray there, the integral becomes a Gaussian integral (containing $e^{-x^2} dx$ terms).

$$\theta(RTA) = \frac{3\hat{R}(\lambda)\rho}{2H_s} \int_{-\infty}^{\infty} \exp\left(\frac{-s^2}{2r_r H_s}\right) ds$$

$$= \frac{3\hat{R}(\lambda)rh}{2} \left[\frac{2\pi r_r}{H_s}\right]^{1/2} \tag{2.34}$$

where $\hat{R}(\lambda)$ is the specific refractivity of dry air at the wavelength, λ, of interest, and ρ is evaluated at the RTP.

If, in addition to the assumption that curvature of the path takes place very near the RTP, it can also be assumed that conditions about the RTP are stable, then data on the atmosphere at the geometric tangent point (the geometric intersection of tangent lines from the star and spacecraft = GTP) can be used to determine H and $\theta(RTA)$. RTA is then approximated by geometric tangent altitude (GTA). This greatly simplifies the problem since GTA is

determined by star, earth and spacecraft positions alone. The equation relating $\theta(\text{GTA})$ and $\theta(\text{RTA})$ is

$$\theta(\text{RTA}) = \theta(\text{GTA}) \exp\left[-\beta\theta(\text{RTA})\right] \tag{2.35}$$

where

$$\beta = \frac{1}{H_s}\left[S_p - \left(\frac{r_r H_s}{2\pi}\right)^{1/2}\right]. \tag{2.36}$$

S_p = distance from observer to point of ray tangency

Since Eq. (2.35) is transcendental in $\theta(\text{RTA})$, large differences in atmospheric conditions $(H_s$ and $\rho)$ between GTA and RTA would require an iterative solution.

Testing this simplified model for $\theta(\text{RTA})$ vs. the complex atmosphere in the ray tracing program showed a relative error of approximately 2 percent in the GTA range 25 to 45 km. This corresponds to an error of 2.4 to .16 arcsec in $\theta(\text{RTA})$. These results indicate that the contribution of atmospheric modeling to the CCD sensor error budget is on the order of 2 arcsec plus the error due to not having current atmospheric data. If monthly atmospheric data are transmitted to the vehicle and if that data can then be extrapolated to produce less than an 8 percent density error, then the refraction model would contribute approximately 1000 m to the error in GTA.

Even a total error in density of 15 percent, giving a GTA

error of 1500 m would result in a 12-hour orbit navigation error of only 350 m with two star-horizon CCD sensor pairs. Lower orbits would feel that GTA error more acutely, and higher orbit accuracy would be better. Before realistic error budgets can be produced, however, more work must be done to quantify errors in long-term density prediction.

CHAPTER 3

GLOBAL POSITIONING SYSTEM

3.1 Introduction

The results of Sections 2.7 and 2.8 show that the optical sensors being developed will produce navigation accuracies on the order of 300 meters. Several satellite programs, however, require errors of less than 50 m and are therefore potential GPS users if GPS can be made less dependent on ground tracking and control. This is the purpose of the remainder of this report -- to investigate the feasibility of autonomous navigation of GPS vehicles using satellite-to-satellite range and integrated doppler information in a reasonably sized onboard navigation processor. The approach taken is to first determine constellation selection effects, then to analyze filter model requirements with consider covariance techniques and to propose an onboard filter design and evaluate its error propagation characteristics.

3.2 GPS Constellations

The Global Positioning System is composed of a spaceborne segment consisting of a variable number of satellites in 12-sidereal hour orbits, a control segment consisting of a Master Control Station (MCS), and four remote Monitor Stations (MS) and a user segment consisting of many different user receiver sets built by

58

several different manufacturers. The number of satellites to be placed in the constellation varies with congressional budget decisions. Descriptions of the system and its several facets abound in the literature, and an excellent collection of papers can be found published together by the Institute of Navigation.

The number of satellites currently planned is 18, and two different constellations have been analyzed by the Joint Program Office (JPO) [Book, et al., 1980]. The first of these is a modified three-plane 24-satellite configuration in which two of the eight satellites in each plane are eliminated leaving an unsymmetric 18-satellite constellation. This is termed the 3 x 6 configuration since three planes of six satellites each are employed. The second candidate constellation consists of six planes with three satellites each in a symmetric pattern, i.e., a 6 x 3 constellation. The orbit elements for these constellations are given in Table 3.1.

According to Book, et al., the unsymmetric 3 x 6 constellation has a geometric performance with respect to the ground almost as good as the symmetric 6 x 3 configuration, where GPS geometric performance is determined by examining the trace of a unit covariance matrix of the user position error as follows [Milliken and Zoller, 1980].

If the user receives information from at least four GPS satellites, he can estimate his position and his clock error and the error in these estimates. He measures a pseudo-range to each

satellite:

$$\overline{\rho}_i = \rho_i + c\Delta t_{Ai} + c\left(\Delta t_u - \Delta t_{g_i}\right) + \epsilon_i \qquad (3.1)$$

where

$\overline{\rho}_i$ = pseudo-range to satellite i

ρ_i = geometric range

Δt_{g_i} = satellite i clock offset from a common time scale

Δt_u = user clock offset

Δt_{A_i} = propagation delays, etc.

ϵ_i = random measurement noise

If Δt_{Ai} is determined or adequately modeled and Δt_{g_i} known for each satellite, then four ρ_i measurements to four GPS vehicles provide information to solve for user position (x,y,z) and clock bias $(c\Delta t_u)$. Since $\rho_i = \left[\left(x_{g_i}-x\right)^2 + \left(y_{g_i}-y\right)^2 + \left(z_{g_i}-z\right)^2\right]^{1/2}$, the measurement partial derivatives are given by

$$H_i = \left[\frac{\partial \overline{R}_i}{\partial x}, \frac{\partial \overline{R}_i}{\partial y}, \frac{\partial \overline{R}_i}{\partial z}, \frac{\partial \overline{R}_i}{\partial c\Delta t_u}\right]_{\overline{\rho}_i = \overline{\rho}_i^*}$$

$$= \left[\frac{x-x_{g_i}}{\rho_i}, \frac{y-y_{g_i}}{\rho_i}, \frac{z-z_{g_i}}{\rho_i}, 1\right]_{\overline{\rho}_i = \overline{\rho}_i^*} \qquad (3.2)$$

Now, assuming a unit error variance in $\overline{\rho}_i$, a user information matrix

can be computed from

$$INF_u = \begin{bmatrix} H_1^T & H_2^T & \cdots & H_k^T \end{bmatrix} \begin{bmatrix} I \end{bmatrix} \begin{bmatrix} H_1 \\ H_2 \\ \cdot \\ \cdot \\ H_k \end{bmatrix}_{k \geq 4} \qquad (3.3)$$

and the corresponding unit covariance matrix is

$$COV_u = INF_u^{-1}. \qquad (3.4)$$

This is termed a unit covariance here because the unit range variances do not reflect reality but produce user position sigmas that can then be multiplied by actual system errors to give realistic user errors. The trace of the COV_u matrix describes the variance of the user's position error and clock bias given a unit variance in each range measurement. $\text{Tr}[COV_u]$ is thus called the Geometric Dilution of Precision (GDOP) since it describes a four-dimensional geometric error. Other similar definitions follow:

$$PDOP = \begin{bmatrix} COV_u(1,1) + COV_u(2,2) + COV_u(3,3) \end{bmatrix} \qquad (3.5)$$

$$\equiv \text{Position Dilution of Precision}$$

$$HDOP = \begin{bmatrix} COV_{u_{RTN}}(2,2) + COV_{u_{RTN}}(3,3) \end{bmatrix} \qquad (3.6)$$

$$\equiv \text{Horizontal Dilution of Precision}$$

$$VDOP = COV_{u_{RTN}}(1,1) \qquad (3.7)$$

$\equiv$ Vertical Dilution of Precision

$$TDOP = COV_u(4,4) \qquad (3.8)$$

$\equiv$ Time Dilution of Precision

Note that GDOP requires the inversion of a 4 x 4 symmetric matrix, and PDOP requires the inversion of a 3 x 3 matrix. It will be seen in GDOP and PDOP plots that they provide essentially the same information; thus, a user can save processor time by using PDOP in selecting the optimum set of four GPS satellites. It would be even more beneficial if the trace of the user information matrix instead of COV_u could be used to determine optimum GPS satellite selection. But, as noticed by Fang [1980], each row_i partial in the H matrix is a unit vector pointing to GPS_i, while the fourth component is 1. When the product H^TH is formed, the resulting trace for n satellites can be obtained through the commutative property of the trace,

$$Tr(H^TH) = Tr(HH^T) \qquad (3.9)$$

but,

$$Tr(HH^T) = \sum_{i=1}^{n} \left(\frac{x-x_{g_i}}{\rho_i}\right)^2 + \left(\frac{y-y_{g_i}}{\rho_i}\right)^2 + \left(\frac{z-z_{g_i}}{\rho_i}\right)^2 + 1 = 2n \qquad (3.10)$$

Therefore, the trace of the user information matrix is a constant equal to 2n for n satellites and gives no information about the geometric attributes of the configuration.

3.3 Constellation Comparison

To determine the effect of constellation selection (3 x 6 or 6 x 3) on GPS vehicle navigation, a relative geometry computer program was written to step through one 12-hour GPS cycle. Each 10 minutes, satellite positions were computed and used to determine GDOP and PDOP for any desired GPS user spacecraft. In addition, satellite visibility times were accumulated so a total percentage of the orbit visible to each satellite was available. Figure 3.1 shows GDOP and PDOP, along with number of satellites visible to the GPS #1 spacecraft for the symmetric 6 x 3 constellation. Elevation limits of -28° to -76°, as recommended by Chao [1981], were used in the visibility check, and all satellites visible were included in the calculations. It was decided to use all visible satellites in the geometry calculat⁀ s because the GPS crosslink $(L_3$ at 1381 MHz) will allow each satellite to transmit for approximately 1.5 seconds every 36 seconds [Barr, 1981] and the navigation algorithm would benefit from clock and position information from all available vehicles rather than selecting an optimum set of 4. GDOP and PDOP follow similar but offset paths for other vehicles, but the GDOP patterns are identical for any two vehicles when corrected for
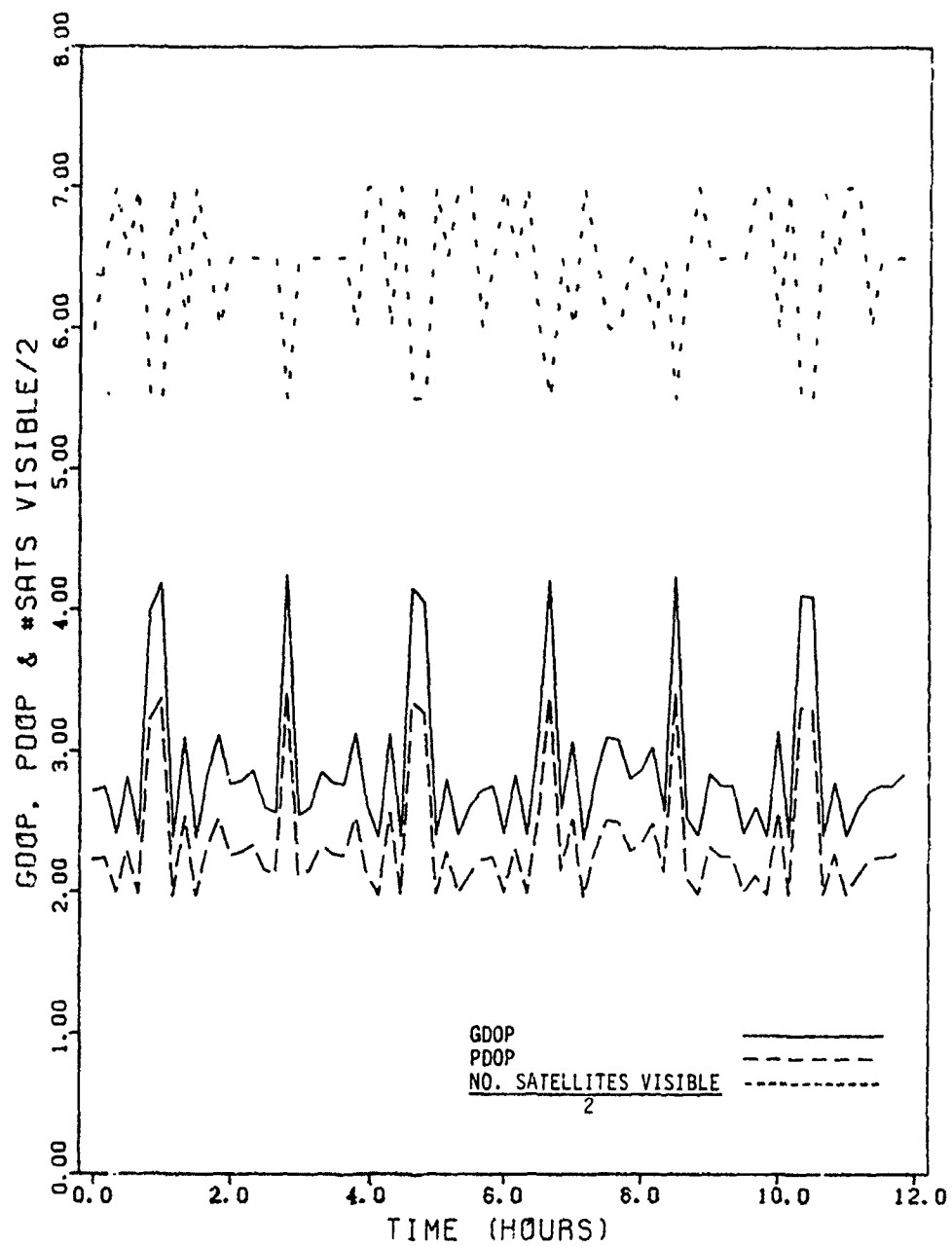
Figure 3.1. GPS Geometric Performance, 6x3 Symmetric
Constellation, Satellite No. 1

satellite phase difference. Note that there is an inverse correlation between GDOP and number of satellites visible, with the minimum GDOP (2.5) corresponding to 14 vehicles visible and the maximum (~4.2) corresponding to 11 visible.

Figure 3.2 shows the same information for the unsymmetric 3 x 6 constellation, satellite #1. This constellation does not produce similar GDOP patterns for different vehicles, and the minimum values (~2.5 and ~2.8) and maximum values (~4.7 and 4.0) are also inconsistent among users. Table 3.2 shows the minimum and maximum values over one orbit for the 18 satellites. Note that most of the values are higher than those encountered in the 6 x 3 constellation and that all of the average values are higher in the 3 x 6 case.

Figure 3.3 shows the percent of the orbit during which each GPS satellite is visible to vehicle #1 in the 6 x 3 constellation. The values range from a low of about 38% to several 100% cases. Figure 3.4 depicts the same information for vehicle #1 in the 3 x 6 constellation. The main difference is that some satellites in the 3 x 6 constellation are invisible to each other (satellite #1 cannot see #2 and #5), potentially weakening the position and clock estimatioon results of the whole system. For this reason and also because of better GDOP performance, the symmetric 6 x 3 constellation is desirable from a satellite-to-satellite tracking viewpoint.
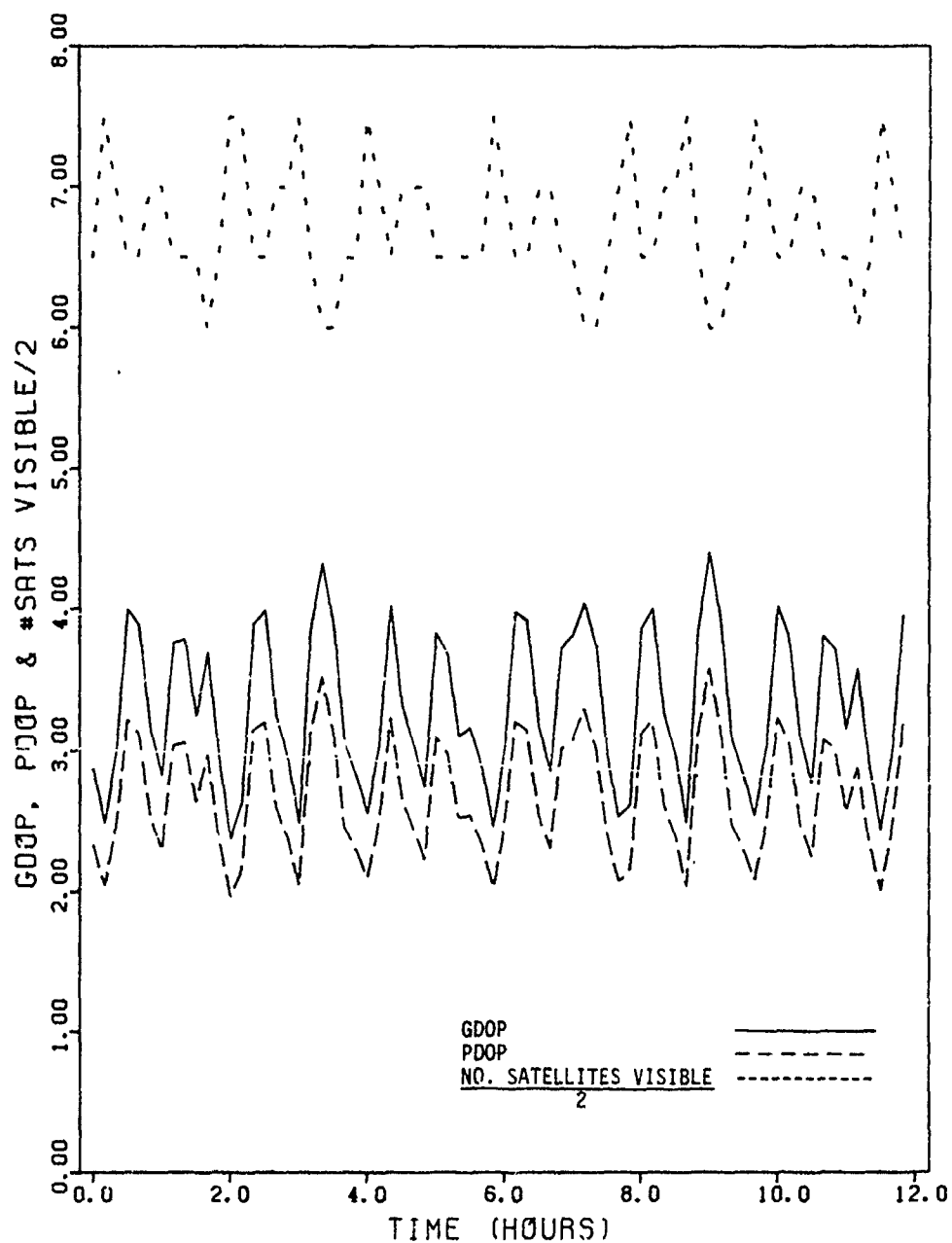
Figure 3.2. GPS Geometric Performance, 3x6 Unsymmetric
Constellation, Satellite No. 1
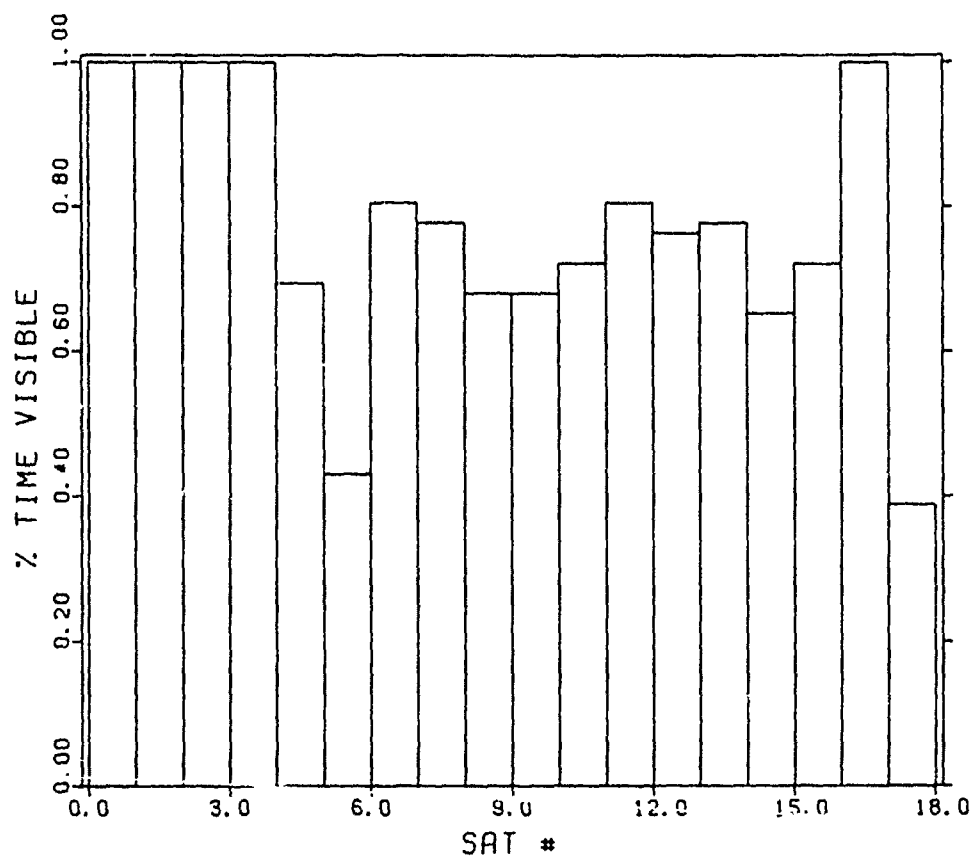
Figure 3.3.   GPS Satellite Visibility to GPS #1 -- Symmetric
6 x 3 Constellation
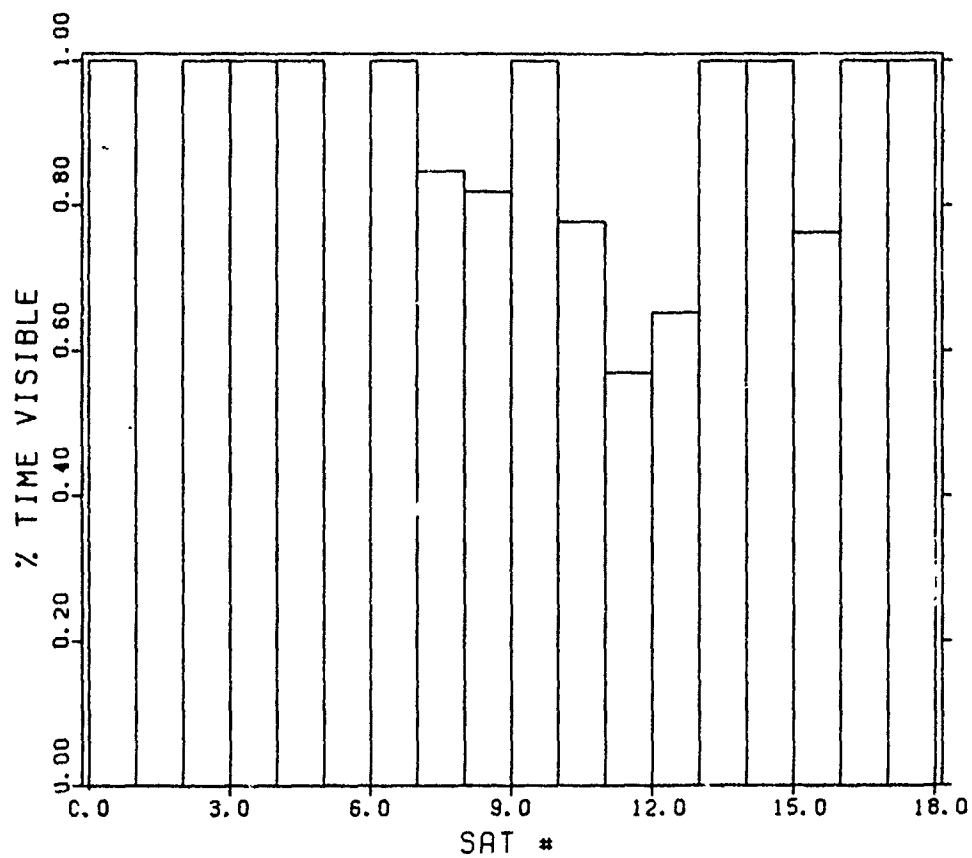
Figure 3.4.   GPS Satellite Visibility to GPS #1 -- Unsymmetric
Figure 3 x 6 Constellation

TABLE 3.1. GPS ORBIT ELEMENTS

A. Unsymmetric 3 x 6 Constellation

Semi-major axis: 26575.6 km

Eccentricity: 0.0

Inclination: 55 deg

Relative Ascending Node: 0, 120, 240 deg

Argument of Perigee: 0 deg

Mean Anomaly at Epoch:
Plane 1:   0,   45,   90, 135, 270, 315 deg
Plane 2:   20,   65, 110, 155, 200, 245 deg
Plane 3:   40, 175, 220, 265, 310, 355 deg

B. Symmetric 6 x 3 Constellation

Semi-major Axis: 26575.6 km

Eccentricity: 0.0

Inclination: 55 deg

Relative Ascending Node: 0, 60, 120, 180, 240, 300 deg

Argument of Perigee: 0 deg

Mean anomaly at Epoch:
Plane 1:   0, 120, 240 deg
Plane 2:   40, 160, 280 deg
Plane 3:   80, 200, 320 deg
Plane 4: 120, 240,   0 deg
Plane 5: 160, 280, 40 deg
Plane 6: 200, 320, 80 deg

3.4 GPS Error Sources

The consider covariance analysis that follows in Chapter 4 provides   realistic   satellite   position errors when given realistic

TABLE 3.2

MINIMUM, MAXIMUM AND AVERAGE GDOP VALUES

A.   Unsymmetric 3 x 6 Constellation

Satellite:	1	2	3	4	5	6	7	8	9
Min GDOP:	2.37	2.47	2.45	2.38	2.46	2.58	2.38	2.46	2.60
Max GDOP:	4.40	4.04	4.72	4.29	4.21	4.70	4.29	4.83	4.51
Avg GDOP:	3.30	3.25	3.48	3.19	3.24	3.46	3.30	3.62	3.51

Satellite:	10	11	12	13	14	15	16	17	18
Min GDOP:	2.65	2.66	2.29	2.58	2.29	2.59	2.38	2.38	2.64
Max GDOP:	4.54	4.62	4.20	4.23	4.10	4.14	4.48	4.58	4.83
Avg GDOP:	3.44	3.60	3.28	3.23	3.19	3.37	3.25	3.35	3.49

B.   Symmetric 6 x 3 Constellation

Satellite:	All
Min GDOP:	2.37
Max GDOP:	4.25
Avg GDOP:	2.88

values of the 1σ errors expected to be seen by the satellite. The purpose of this section is to describe the error sources in the GPS autonomous navigation scenario and, where necessary, to determine values or bounds on the values expected to be experienced by the satellite. The results of the consider analysis will then indicate which error source effects must be modeled or estimated in the onboard filter algorithm. Some of these effects are unobservable by satellite-to-satellite tracking, so these error sources, if the effects are large enough, will be added to the onboard algorithm without considering them in the covariance analysis.

The GPS autonomous navigation problem contains several error sources in common with a user on the ground and some unique errors of its own. A ground user experiences the following error sources [General Dynamics, 1978]:

a. user clock bias and drift,

b. satellite clock bias and drift,

c. receiver movement during signal transit,

d. satellite ephemeris,

e. relativistic effects,

f. antennae offsets,

g. receiver signal delay,

h. time tagging,

i. ionospheric delay,

j. tropospheric delay.

A GPS satellite receiver located above the ionosphere sees errors due to

a. user clock bias and drift,

b. satellite clock bias and drift,

c. receiver movement during signal transit,

d. satellite ephemeris,

e. relativistic effects,

f. antennae offsets,

g. receiver signal delay,

h. time tagging,

i. earth geopotential,

j. n-body gravity,

k. solar radiation pressure,

l. vehicle thrusting or outgassing,

m. earth polar motion and angular velocity.

In this study, it is assumed that pre-processing of pseudo-range and integrated doppler measurements is performed and that residual errors due to receiver movement, relativity, antennae offsets, receiver signal delay and time tagging can be modeled or corrected for with the remaining measurement errors expressed as uncorrelated, zero-mean, Gaussian errors. Simulation of the remaining errors is described in the following sections.

3.4.1 GPS Clock Errors

Operational GPS satellites are planned to contain two rubidium and two cesium beam frequency standards with the possible addition of a hydrogen maser [Payne, 1982]. To characterize the errors inherent in these precise time standards, it is convenient to measure clock stability in terms of the Allan variance of its fractional frequency error, $\frac{\delta f}{f_o}$. The error in the GPS clock after some elapsed time from update is

$$T(f) - T(f_o) = \frac{\Delta f}{f_o} (t-t_o) + \frac{\dot{f}}{2f_o} (t-t_c)^2$$

$$+ \int_{t_o}^{t} \frac{\delta f(s) ds}{f_o} \qquad (3.11)$$

where

$f_o = 2\pi\nu_o =$ nominal frequency (rad/sec)

$f =$ time-varying true frequency

$\Delta f =$ frequency offset

$\dot{f} =$ frequency drift

$\delta f(t) =$ time-varying random frequency error

Differentiating yields

$$\frac{\Delta f(t)}{f_o} = \frac{\Delta f(to)}{f_o} + \frac{\dot{f}}{2f_o} (t-t_o) + \frac{\delta f(t)}{f_o} \qquad (3.12)$$

Now, following the description by Meditch [1975], let

$$y(t) = \frac{\delta f(t)}{f_o} \equiv \text{fractional frequency error,} \qquad (3.13)$$

then the average fractional frequency error over a sampling period, τ, is

$$\overline{y}_k = \frac{1}{\tau} \int_{t_k}^{t_k + \tau} y(t)dt, \qquad (3.14)$$

which, after substituting and assuming δf constant over τ, becomes

$$\overline{y}_k = \frac{\phi(t_k + \tau) - \phi(t_k)}{f_o}, \qquad (3.15)$$

where $\phi(t)$ is the phase error at t. The Allan variance is then defined as

$$\sigma_y^2(\tau) = \frac{1}{2} E[(\overline{y}_{k+1} - \overline{y}_k)^2]$$

$$= \frac{1}{2m} \sum_{k=1}^{m} (\overline{y}_{k+1} - \overline{y}_k)^2$$

for m samples of $\overline{y}$.

Allan variance is defined in the time domain by $\sigma_y^2(\tau)$ and in the frequency domain by $Sy(f)$. Clock errors in the frequency domain typically exhibit at least two types of frequency standard noise: white frequency noise, defined by a constant spectral density versus frequency and flicker noise, defined by a

-20 db/decade slope versus frequency. In addition, at very low frequencies (long sample times, τ), the integral of white noise causes a -40 db/decade slope. A typical Allan variance curve showing GPS specifications is given in Figure 3.5, along with actual on-orbit clock values [Payne, 1982].

3.4.1.1 GPS Clock Error Simulation

Since Allan variance is widely used as a measure of atomic frequency standard stability, time error simulation using an input value for Allan variance is a necessity for GPS error analyses.

To generate a frequency error signal, $y(t)$, and its integral, the phase error, the Allan variance curve is described in the time domain by the power series

$$\sigma_y^2(\tau) = \sum_\beta K_\beta \, \tau^\beta \tag{3.17}$$

where $\beta = -2, -1, 0, +1, +2$ and each value of β dominates in a region τ_i to τ_j. In the frequency domain, a similar series can be used to compute the one-sided spectral density,

$$Sy(f) = \sum_\alpha h_\alpha \, f^\alpha \tag{3.18}$$

with α having the same values as β. Similar to β, each value of α dominates over a certain frequency range. The constants, K_β and h_α define the level of the time or frequency clock error
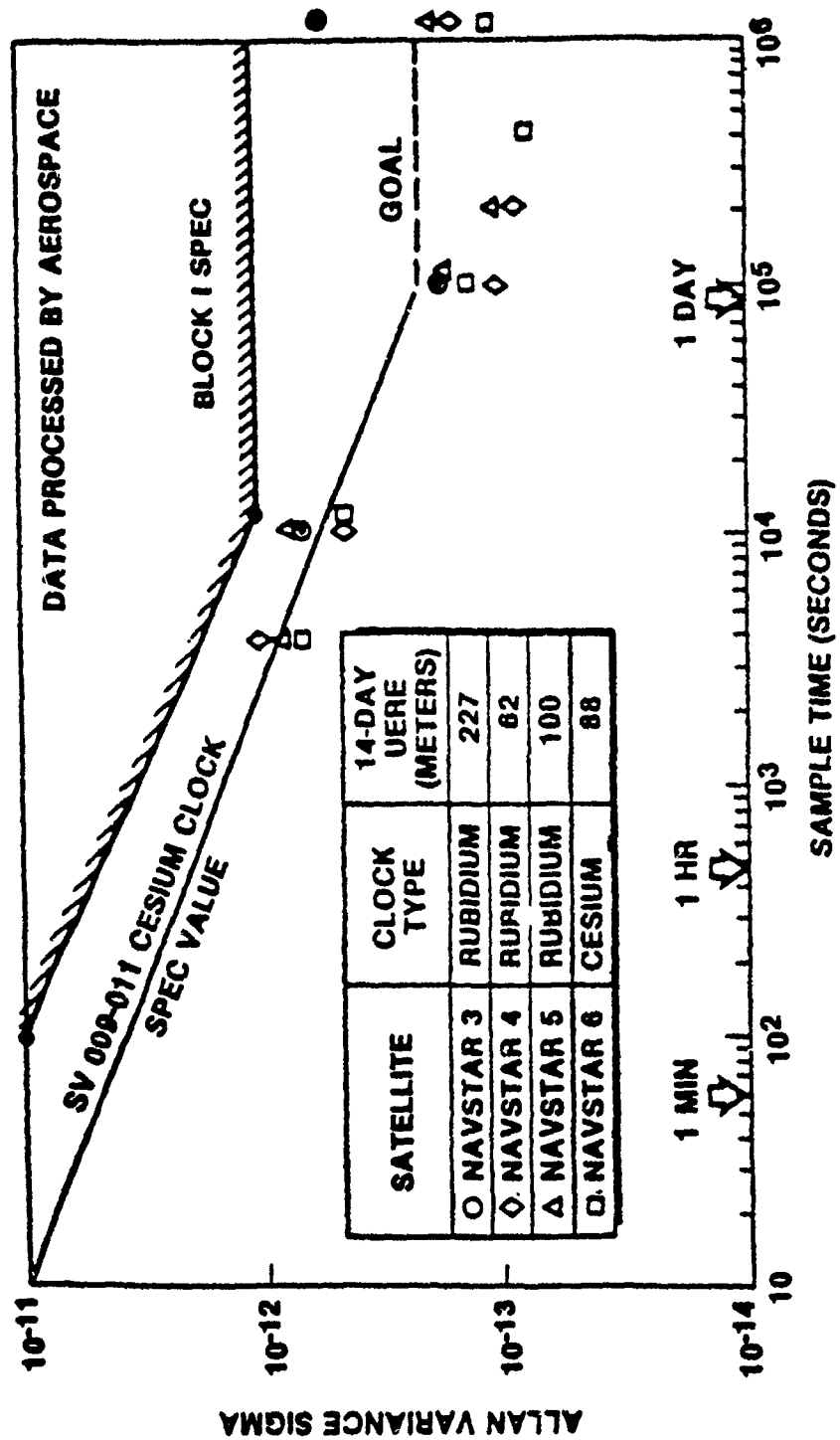
Figure 3.5. On-Orbit Frequency Standard Performance

segment.

To simulate $y(\tau)$, the Allan variance levels and corner frequencies are specified. These values determine the Bode plot of the one-sided spectral density. From the Bode plot, spectral shaping produces a dynamic system function [Laning and Battin, 1977]. An inverse Laplace transform then generates time domain linear differential equations. The solution of these equations produces $y(\tau)$ and its integral.

For white frequency noise and integrated white frequency noise, the inverse Laplace transform is straightforward. The power spectral density function corresponding to integrated white noise (frequencies below f_1 or averaging times above τ_2) is

$$Sy(s) = \frac{b^2(s^2 + a^2\omega_1^2)}{a^2(s^2 + \omega_1^2)} \qquad (3.19)$$

where s is the complex frequency $\sigma + j\omega$ and $\omega = f$.

This is the spectral density of a Gaussian white noise process driving a linear system. It can then be expressed as

$$Sy(s) = H(s) \; H*(s) \; Su(s) \qquad (3.20)$$

where $H(s)$ is the linear system transfer function, $H*(s)$ is its complex conjugate and $Su(s)$ is the spectral density of the white noise process. Since $Su(s)$ is constant, assume it to be unity, implying unit variance, then

$$H(s) = \frac{b}{a} \frac{(s + a\omega_1)}{(s + \omega_1)} \qquad (3.21)$$

and the transfer function for the output signal is

$$Y(s) = H(s) \, U(s) = H(s). \qquad (3.22)$$

Taking an inverse Laplace transform produces the linear differential equation

$$\dot{x}(\tau) = -\omega_1 x(\tau) + (a-1)\omega_1 u(\tau) \qquad (3.23)$$

then

$$y(\tau) = \frac{b}{a} \left[x(\tau) + u(\tau) \right] \qquad (3.24)$$

where $u(t)$ is the output of a unit variance Gaussian random number generator.

Flicker noise, however, cannot be generated by one inverse Laplace transform since the spectral density curve corresponds to a transfer function of the form

$$H(s) \sim \frac{1}{(s)^{1/2}} = \left(\frac{1}{s}\right)^{1/2} \qquad (3.25)$$

for which a finite-order state representation cannot be constructed which will generate the system output [Meditch, 1975]. Several approaches to approximate $y(t)$ for flicker noise have been proposed, and Meditch describes a method by Barnes and Jarvis [1971] that efficiently models $1/(s)^{1/2}$ by a cascade of lag networks.

The technique consists of approximating the desired transfer function with slope -10 db/decade with n stages, each consisting of a -20 db/decade section and a white noise (constant spectral density) section. For simulation purposes, Meditch states that a choice of n = 4 gives a reasonable and efficient approximation to the desired shape.

Once the series approximation to $1/(s)^{1/2}$ is complete, the inverse Laplace transform gives a linear differential equation for each stage. These equations then form an n-vector linear differential equation whose solution provides $x(\tau)$ such that $y(\tau)$ for averaging times between τ_1 and τ_2 can be simulated.

As seen in Figure 3.5, GPS clocks are exhibiting Allan variances of 10^{-12} for $\tau = 1$ hour to 10^{-13} for $\tau > 2$ days. These values give stabilities of 10^{-3} to 10^{-4} ns/s and are used in the GPS navigation error model as expected accuracies of operational cesium clocks. It is assumed that hydrogen masers are one order of magnitude better [Kartaschoff, 1978, p. 62]. Note that, from Figure 3.5, another order of magnitude improvement in $\delta f/f$ would allow the clocks to run independently for 140 days with a user equivalent range error (UERE) of approximately 90 meters.

3.4.2 Satellite Ephemeris Errors

GPS ephemeris errors in the ground tracking mode are required to be on the order of 1-10 m. Current estimates of

position errors indicate that 12-hour periodic errors of 2, 10 and 6 m in the RTN directions are combined with a secular tangential error growth of 3 m/day [Anderle, 1980]. This short-term linear growth becomes quadratic in the long term. GPS satellite-to-satellite tracking errors, however, have not been quantified for long-term operation. This is one goal of this study. Liu's [1981] analysis of satellite ephemeris errors over two weeks of GPS-GPS tracking shows an 80 m secular growth and a six-hour 20 m periodic term due to solar radiation pressure errors.

In this study, one satellite at a time is analyzed and it is assumed that initial RTN error sigmas are 2, 10 and 6 m, respectively, with a secular tangential growth of 3 m/day for the other vehicles. These values are used in the consider analysis to determine navigation errors of satellite #1.

3.4.3 Earth Geopotential Errors

One of the goals of this study is to determine the accuracy and size (order and degree) of the onboard geopotential required for accurate GPS navigation. In addition to being subject to secular perturbations due to J_2, the GPS 12-hour orbit is resonant with the harmonic coefficients of degree 2 and 4, so errors in their values and errors due to their absence in the onboard filter will be magnified over any long prediction interval.

Table 3.3 from Wagner and Lerch [1978] describes the

estimated error in the GEM 8 earth model obtained by comparing the earth model predictions with new observations not included in the model formulation. These errors are then used in the analysis of geopotential error effects on GPS orbits in Chapter 4.

TABLE 3.3

ESTIMATED GEM 8 GEOPOTENTIAL ERRORS (x 10^{-9})

Degree (ℓ)

	0	1	2	3	4	5	6	7	8	9	10	11	12
2	1	3	5										
3	2	7	11	14									
4	1	5	6	6	11								
5	2	8	12	13	14	18							
6	2	7	9	9	12	10	15						
7	3	10	14	15	16	16	16	22					
8	2	9	12	12	14	12	16	12	17				
9	2	12	16	18	20	17	19	18	17	11			
10	2	10	15	16	17	16	17	14	17	11	16		
11	3	14	17	21	20	21	20	18	19	12	16	17	
12	3	11	15	19	18	21	18	18	18	11	15	8	7

Order (m)

3.4.4 Solar Radiation Pressure

As stated in Section 3.4.2, solar radiation errors considered by Liu caused a 20 m periodic satellite position error. Liu assumed a 1σ radiation pressure error of 10%, for an acceleration uncertainty of 10^{-10} m/s². Recent discussions with the NSWC personnel who determine GPS reference orbits indicate that radiation pressure coefficient errors (1σ) of approximately 1% have been observed. These figures provide a range for the errors

considered in this analysis.

3.4.5 Vehicle Thrusting or Outgassing

The GPS vehicle is subject to periodic gas jet thrusting to maintain or change orbital elements and to dump excess momentum from the attitude control system (ACS) momentum wheels. The orbit adjusts are planned and occur infrequently, but when gas jet momentum dumping occurs, it is performed automatically by the ACS. If operational satellites employ gas jet dumping, satellite navigation performance would suffer dramatically each time gas jet firings occur because of thrust imbalance and possible plume impingement. It is expected, however, that magnetic dumping of momentum will be accomplished by the onboard ACS processor. Tests on current GPS vehicles indicate that magnetic momentum dumping is successful [Ferguson and Kronke, 1980], so gas jet thrusting is necessary only for orbit maneuvering.

Outgassing is a phenomenon that does not lend itself to easy prediction. Phase I GPS vehicles on orbit appear to be experiencing an acceleration along the spacecraft solar panel axis on the order of $\pm 10^{-12}$ to $\pm 10^{-13}$ m/s^2. The cause of this acceleration is possibly due to unmatched radiators on opposite sides of the vehicle, and this thrust, while not strictly outgassing, has a form similar to that caused by the boiling off of volatile gases. If analysis confirms that the operational vehicles

may experience unmodeled thrusting, then the onboard filter must include these unmodeled accelerations in the state vector. Since the existence and form of these accelerations in the operational system are unknown, they are neglected in this analysis.

3.4.6 Earth Polar Motion and Angular Velocity

Even if the GPS satellites could navigate accurately with respect to each other and contained precise models of the other perturbing forces, the constellation would still drift from the earth-centered, rotating frame (ECR) in which user positions are defind. The largest error source between an inertial earth-centered frame (ECI) and the ECR frame is the angular velocity of the earth, with smaller errors caused by polar motion. The integral of angular velocity errors is the time difference UT1-UTC. Currently, it has a yearly drift of approximately 1 second, the well-known leap second correction.

UTC (Coordinated Universal Time) represents a "uniform time scale" and is obtained by applying a fixed offset of 32.184 seconds to an international atomic time scale (TAI) maintained by the Bureau International de l'Heure (BIH) in Paris [The Astronomical Almanac, 1983]. The difference, UT1-UTC, plus the record of leap seconds then is a measure of the changes in earth's rotation rate. UT1-UTC is published for 5-day intervals by the BIH, and these tables provide the raw data by which UT1-UTC can be

predicted and these predictions verified [BIH, 1974].

3.4.6.1 UT1-UTC Prediction

BIH tables from 1974 to 1980 were analyzed to determine the long-term (> 6 month) predictability of UT1-UTC. Short-term predictions have been made by Zhu [1981] and Meyerhoff [1978] in which curve fitting techniques were used to fit UT1-UTC values over one year (Meyerhoff) and three years (Zhu) and then predict these values for periods of 5 to 40 days. Each study used a series of the form

$$UT1-UTC = a + bt + \sum_{i=1}^{n} \left[c_i \sin \left(\frac{2\pi i t}{365} \right) + c_i \cos \left(\frac{2\pi i t}{365} \right) \right]$$

(3.30)

Zhu set $n=2$ and Meyerhoff determined fits for $n=1$ to 15 with the best results obtained with $n=4$ to 6. Meyerhoff's power spectral analysis indicated that n must be at least 4 to fit the major frequencies. Both authors then predicted UT1-UTC values for a large number of 5- to 40-day intervals. Meyerhoff found that 1σ errors of 2 to 7 ms resulted from his 5- to 20-day predictions, and Zhu observed prediction errors of 1.8 ms for 5-day predictions to 3.7 ms for 40 days but that the errors grew rapidly after 40 days. It appears that the determination of the long-term drift over three years significantly improved Zhu's results.

Since autonomous operation of GPS for six months is a

goal, the long-term prediction of UT1-UTC is a requirement of the onboard software. To determine the accuracy of this prediction, BIH data from 1974 through 1980 were fit in one-year batches by Eq. (3.30) with n=4. The fit residuals shown for 1974 and 1979 (Figures 3.6 and 3.7) are typical, and it is seen that the fits exhibited maximum errors of approximately 4 ms and RMS values of 2 ms. When the equations were used to predict UT1-UTC for one year following the fit, several different types of behavior were observed. The best prediction was for 1975 (Figure 3.8), with maximum errors of -10 and +17 ms and an apparent long-term periodic behavior. 1975 data predicted to 1976 (Figure 3.9), however, showed a negative slope secular trend with the maximum error reaching -78 ms, and the 1979 fit-1980 prediction (Figure 3.10) had a positive slope with a maximum error of 115 ms. In all of the one-year predictions, six-month performance was better than 70 ms.

When data over three years were fit, Eq. (3.30) was augmented by the addition of two-year periodic terms. After correcting for leap seconds, a sliding three-year fit for data between 1974 and 1979 was used to predict UT1-UTC values for the following one year. The results for one-year predictions at six-month intervals are shown in Figures 3.11 through 3.15, where maximum six-month prediction error was -58 ms and the RMS error for all predictions was 36.7 ms. Note that six-month predictions were much better than those for one year. The one-year RMS error was 86
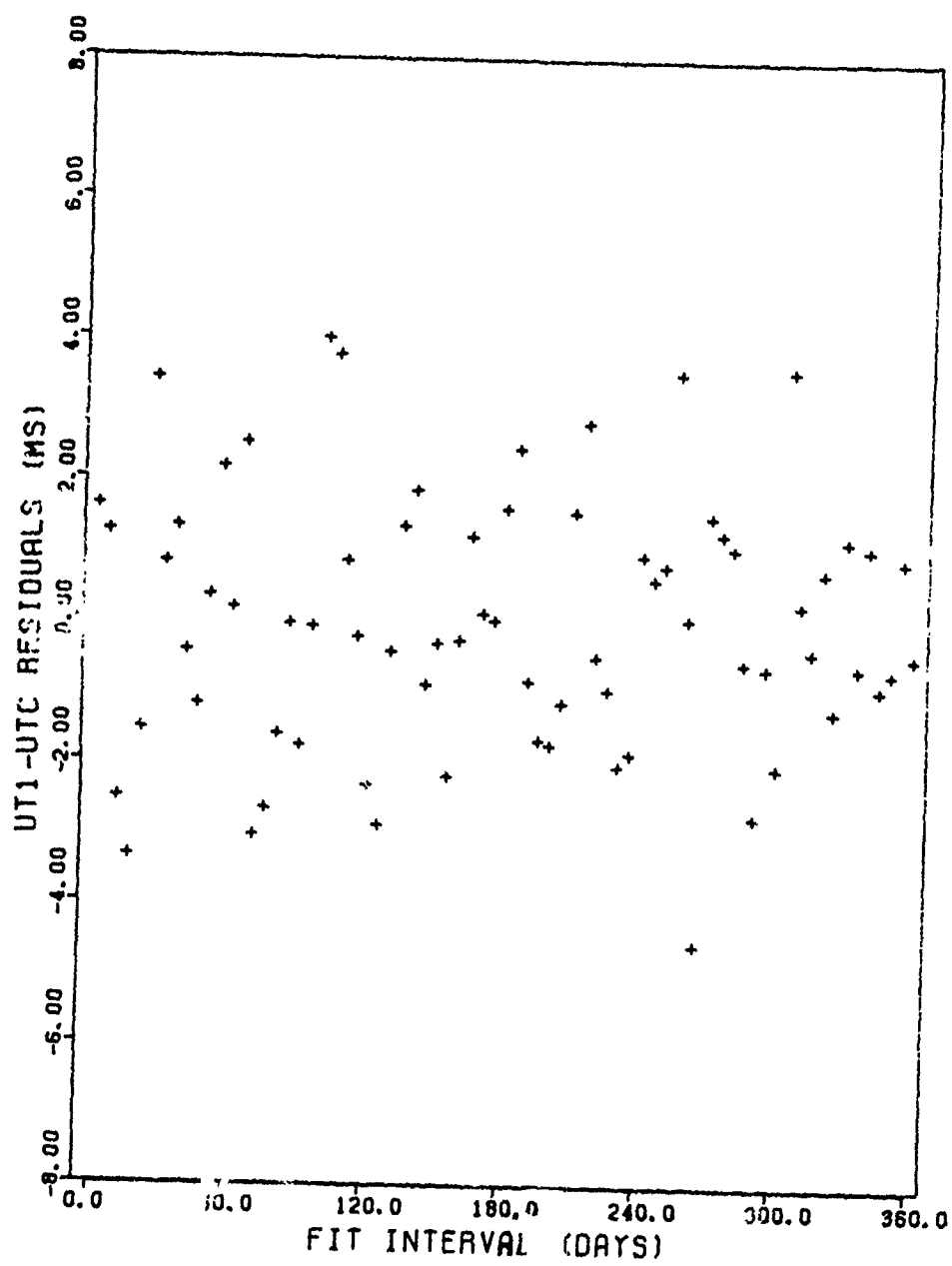
Figure 3.6.   BIH Fit Residuals for 1974
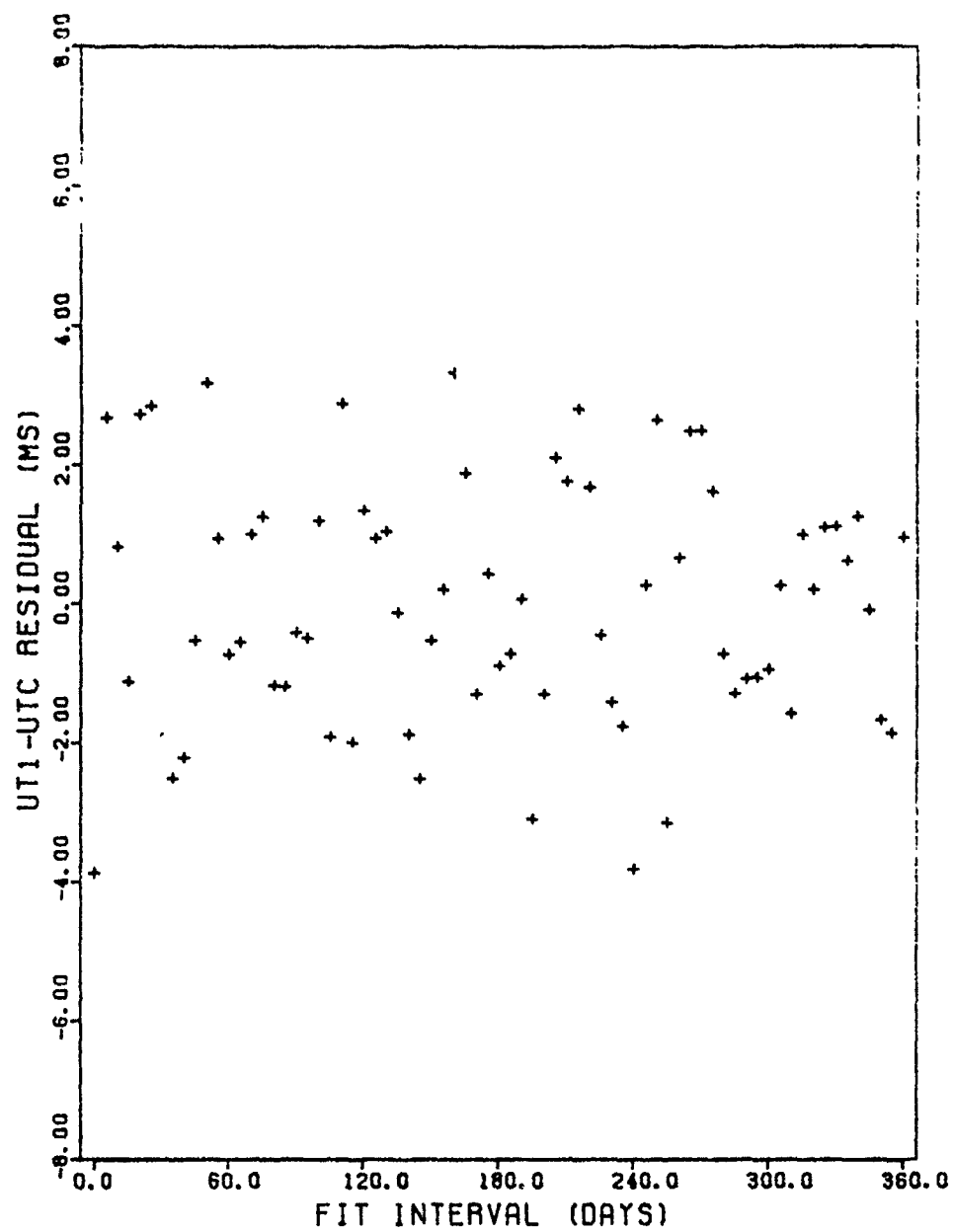
Figure 3.7. BIH Fit Residuals for 1979
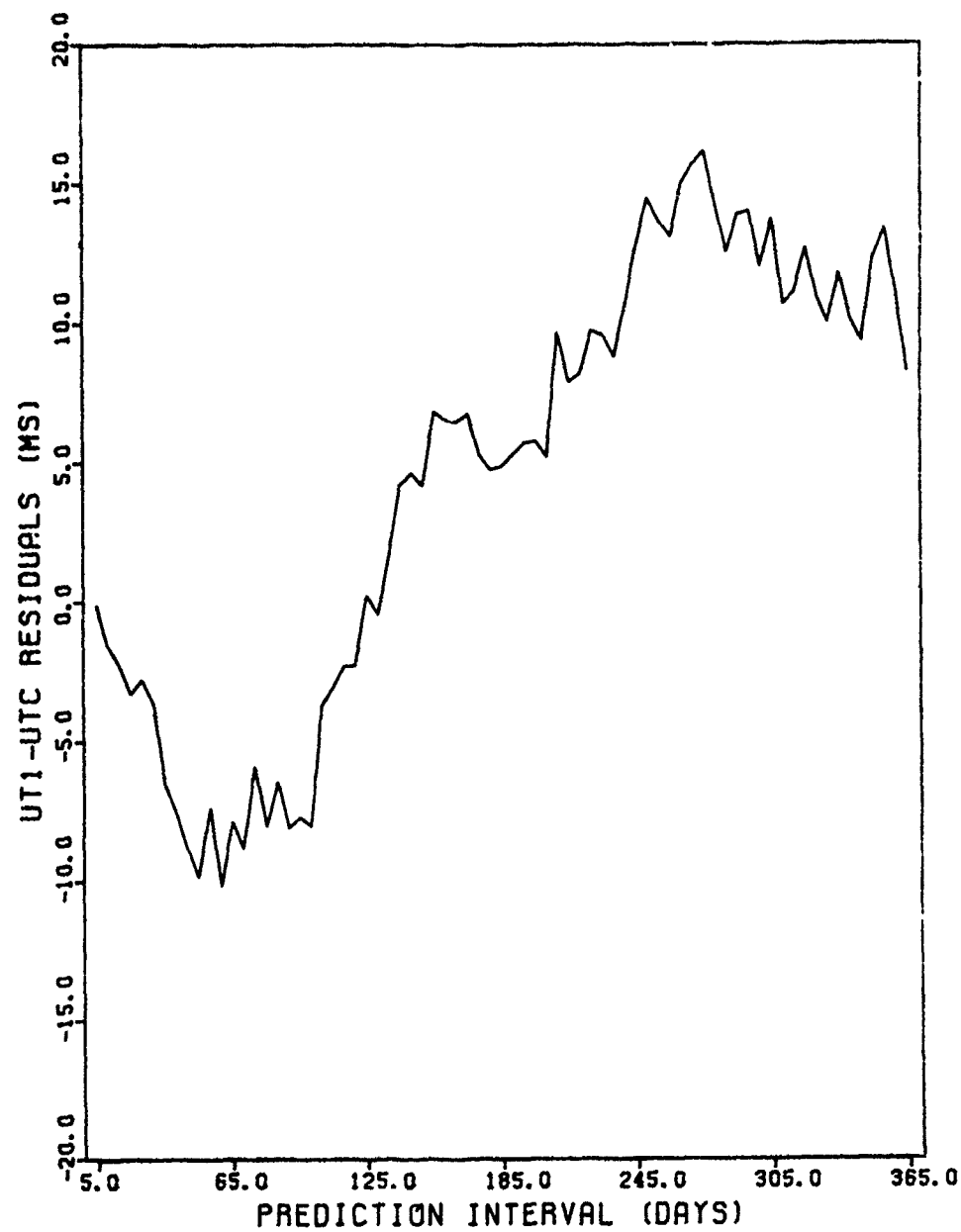
Figure 3.8.   BIH Fit for 1974, Prediction for 1975
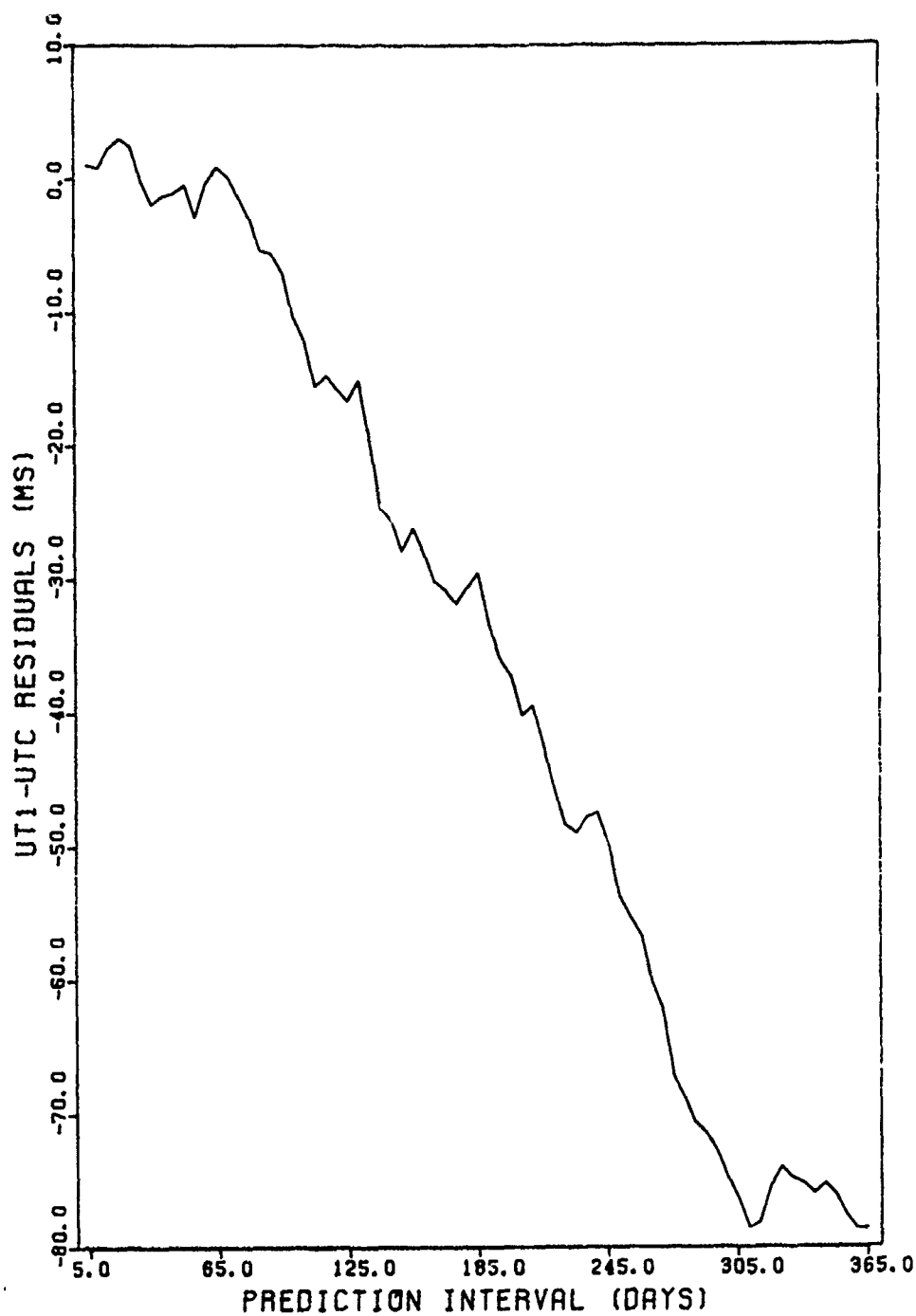
Figure 3.9. BIH Fit for 1975, Prediction for 1976
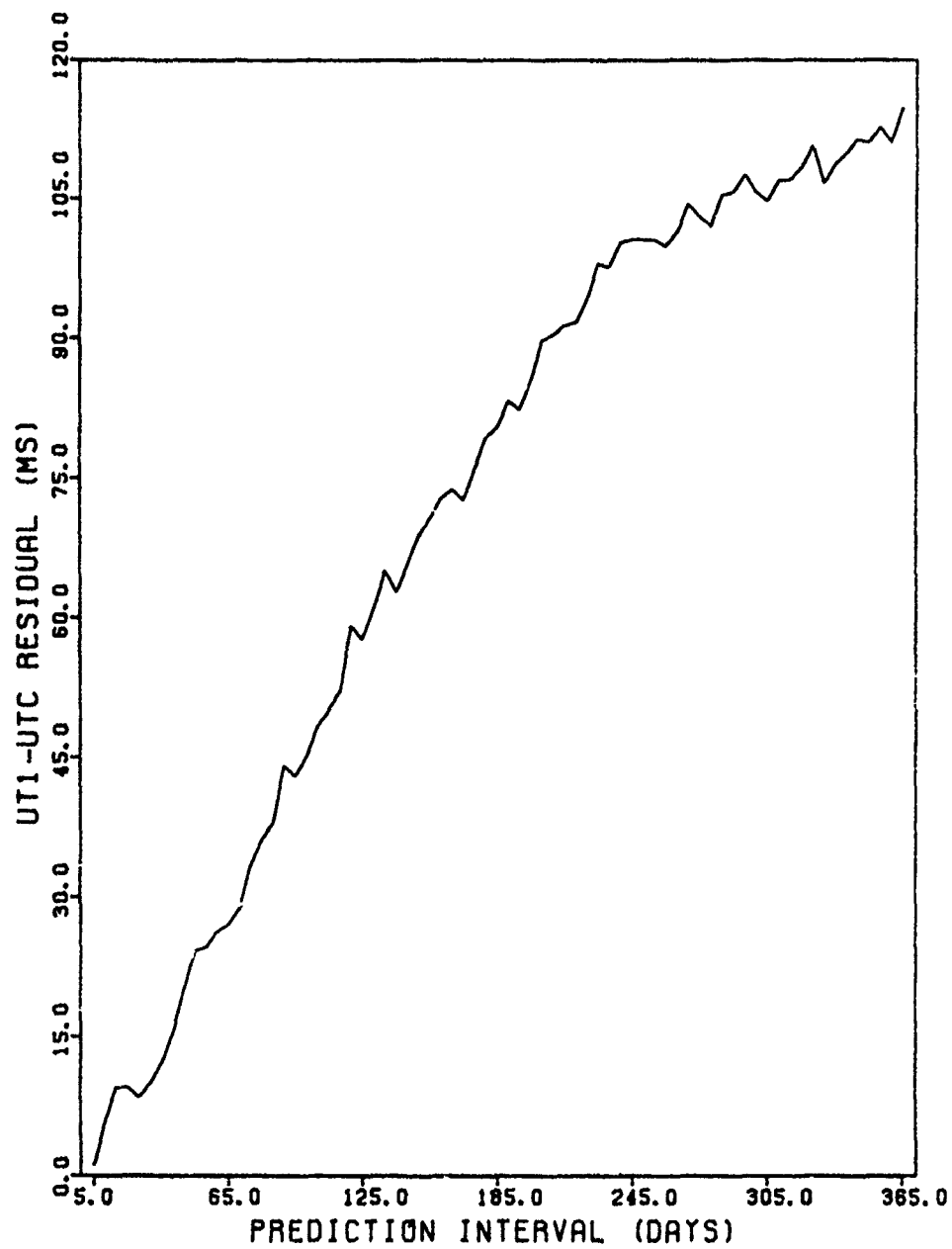
Figure 3.10. BIH Fit for 1979, Prediction for 1980
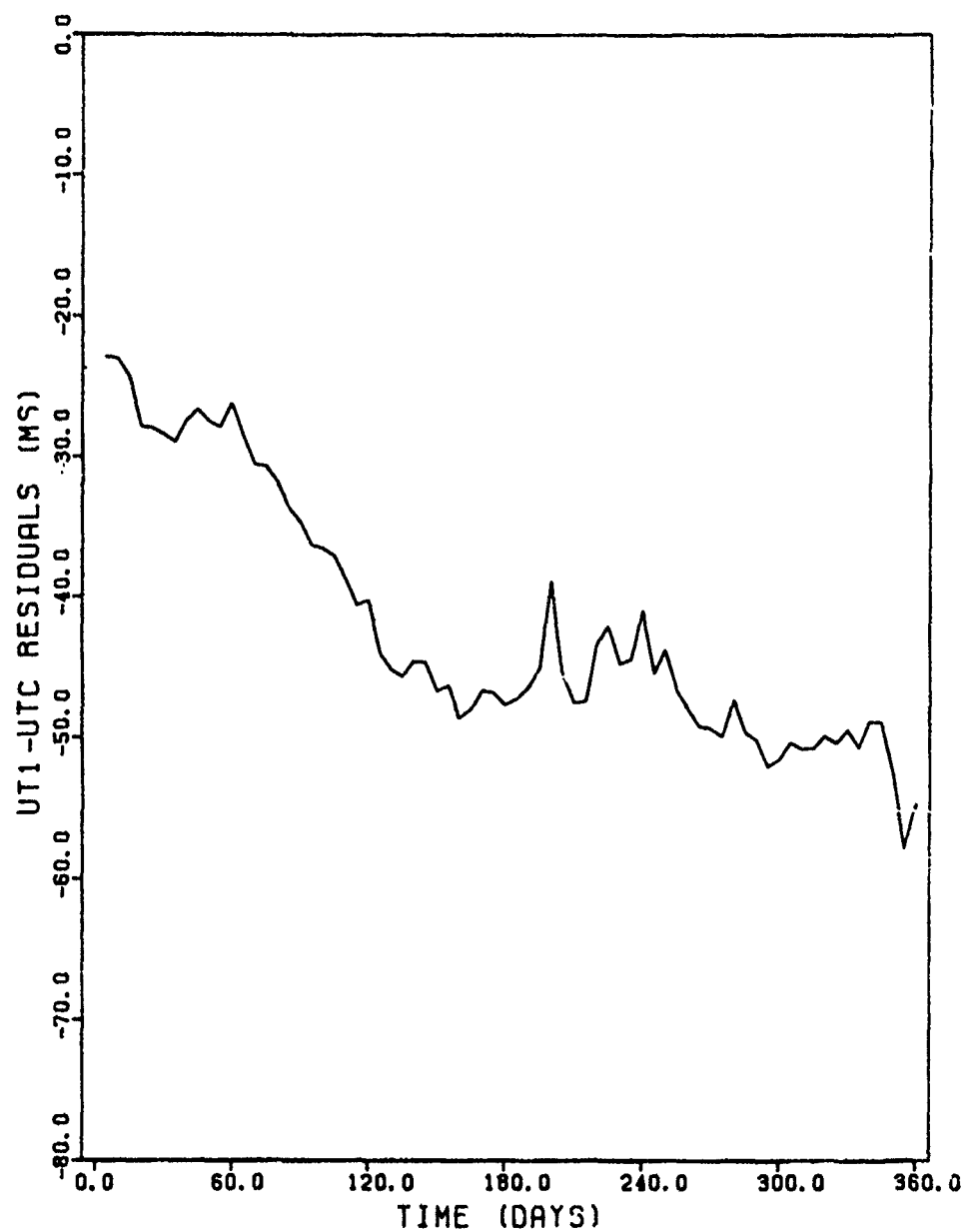
Figure 3.11.   BIH Fit for 1974-76, Prediction for 1977
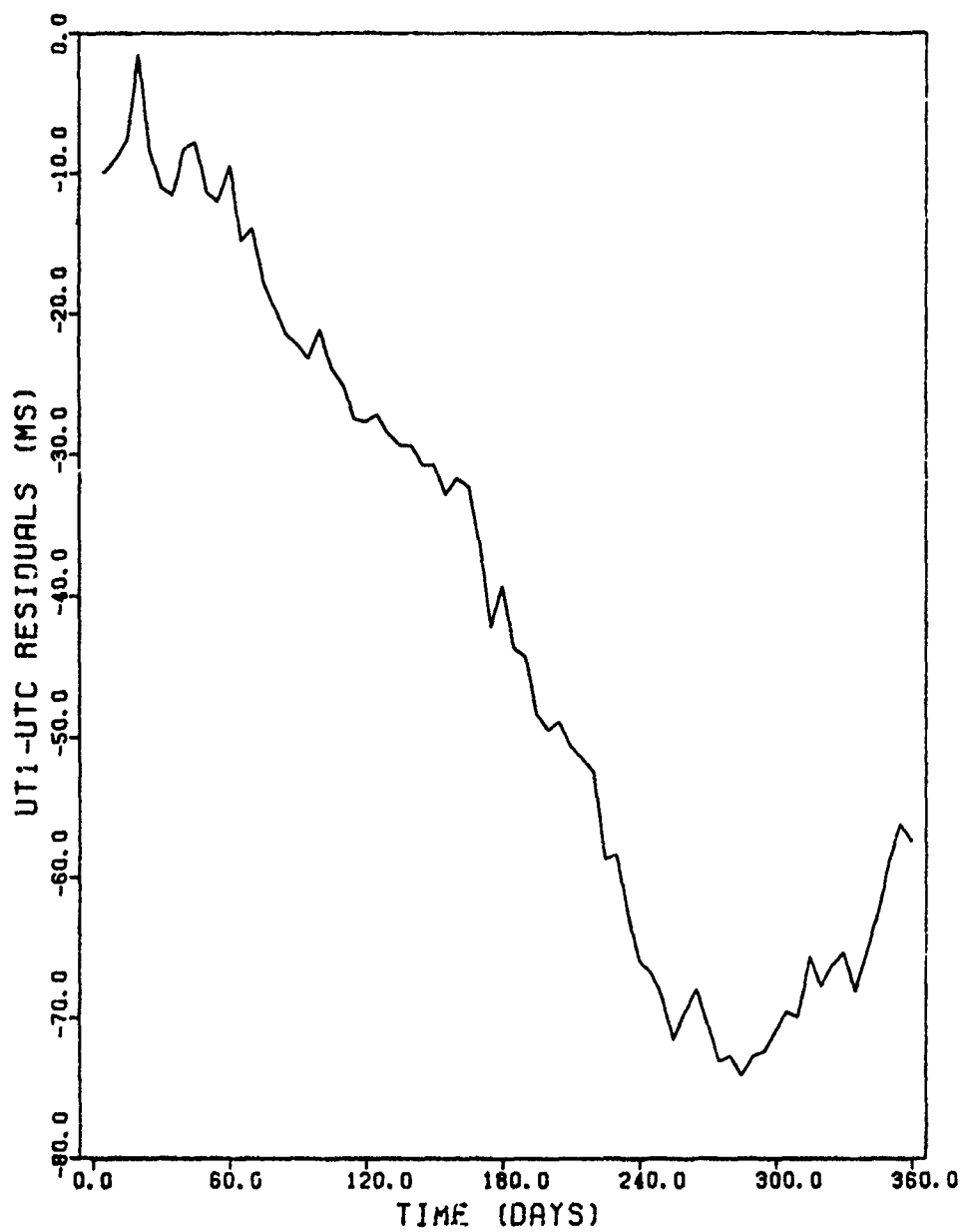
Figure 3.12.   BIH Fit for 1974.5-77.5, Prediction for
1977.5-78.5
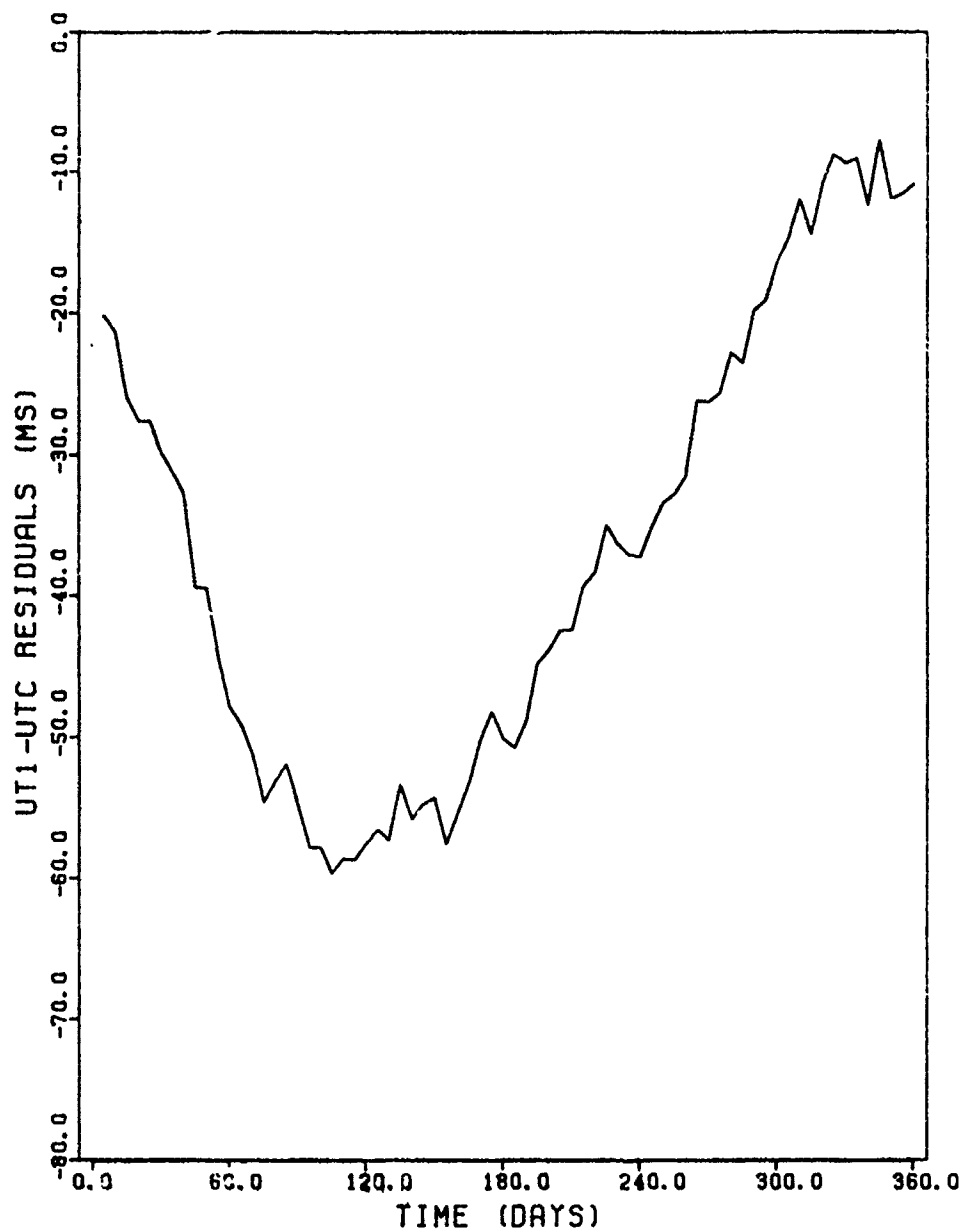
Figure 3.13. BIH Fit for 1975-77, Prediction for 1978
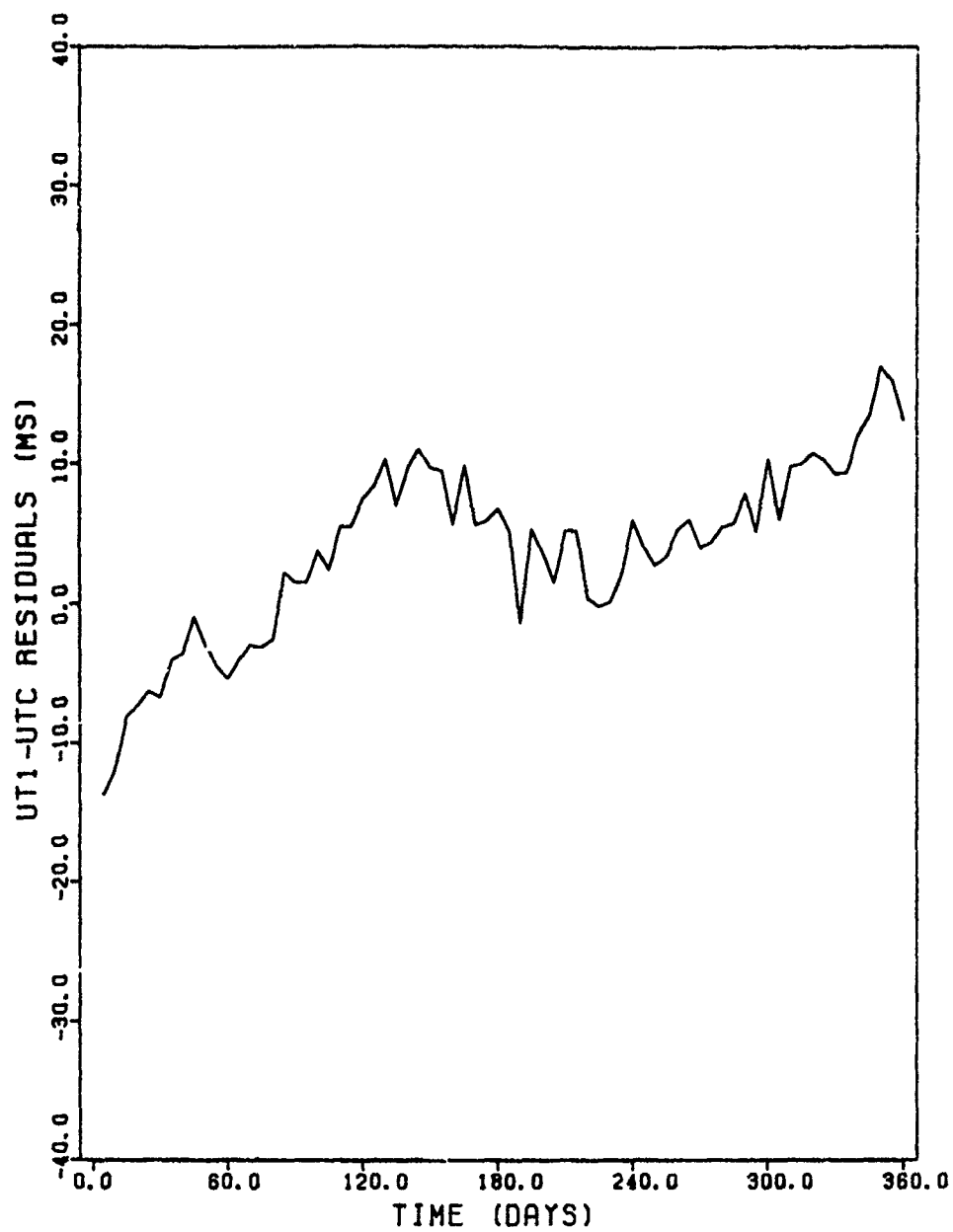
Figure 3.14. BIH Fit for 1975.5-78.5, Prediction for
1978.5-79.5
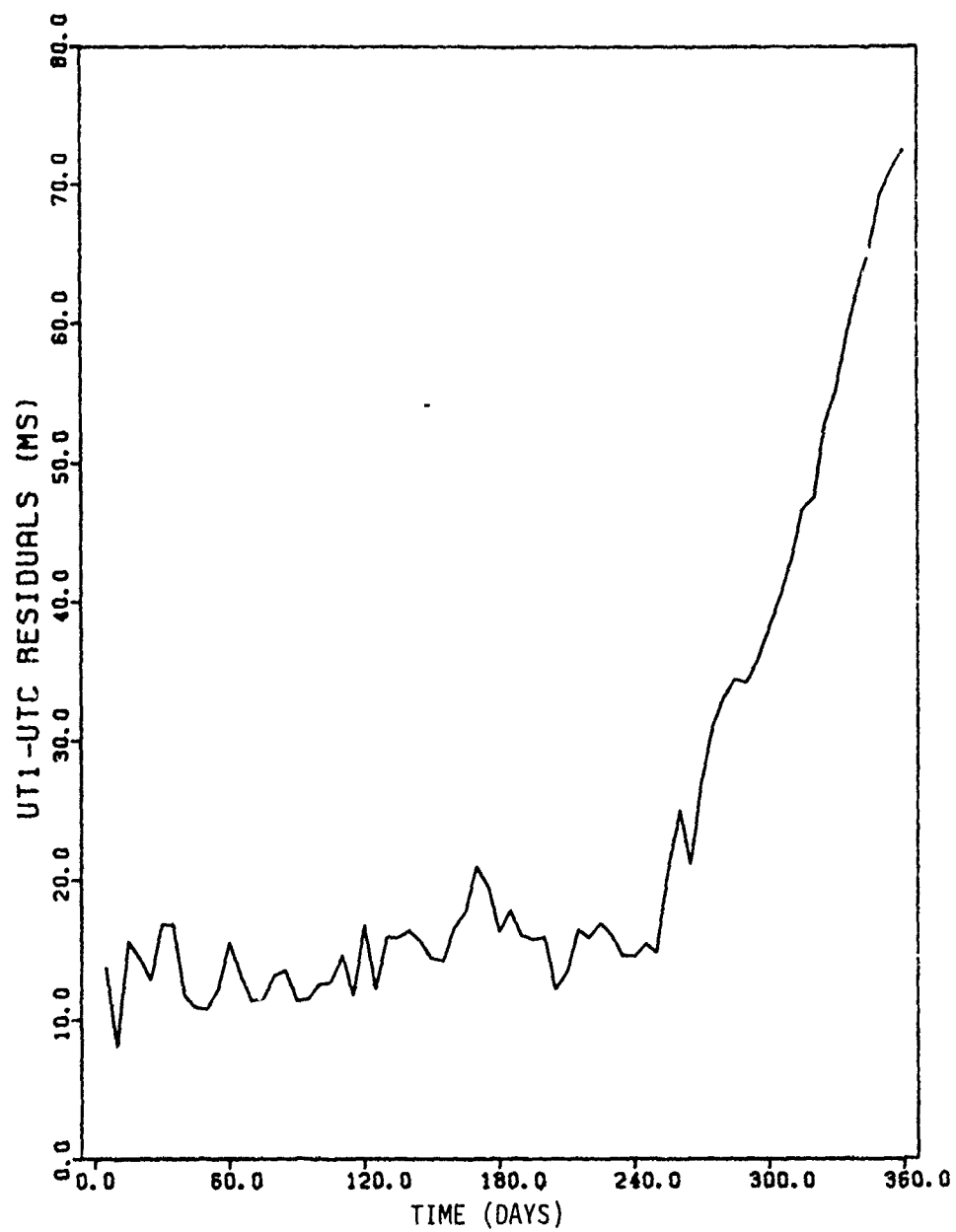
Figure 3.15. BIH Fit for 1976-78, Prediction for 1979

ms and several examples of large secular growth were observed.

From these data, it appears that errors of up to 70 ms arise when one-year BIH data is used to predict for six months but that three-year data spans allow predictions with 1σ errors of less than 40 ms to be made. Since 50 ms appears a reasonable limit to six-month UT1-UTC predictions, the effect of this error on GPS navigation will be assessed.

A UT1-UTC error of 50 ms corresponds to an angular error between the ECR and ECI coordinate frames of 3.65 μrad = .75 arcsec. At GPS altitude, this represents an apparent ephemeris error at the equator of 96.5 m. For GPS navigation, this is a large error compared to the desired accuracy but may not be as severe as other error sources over six-month operation. If degraded performance is allowable for extended autonomous operation, this error may be acceptable. In event this error must be reduced better understanding of earth rotation, periodic onboard model update or active GPS tracking of earth-based transmitters would be required.

3.4.6.2 Polar Motion Prediction

Both Meyerhoff [1978] and Zhu [1981] report that modeling of the moving coordinates of the geographic north pole to much better levels than the UT1-UTC error. Meyerhoff's 20-day pole positions showed x-only coordinate errors of approximately .02 and .01 arcsec, respectively, while Zhu reports 60-day average RSS

errors of .02 arcsec. Zhu suggests that this .02 arcsec error remains fairly constant for up to two years of prediction, thus polar motion is about three orders of magnitude less severe than earth rotation rate as an error source.

3.4.6.3 GPS Coordinate Systems

A GPS user receives satellite position information in the ECR coordinate system [Van Dierendonck, et al., 1980], while the MCS software determines the satellite state in an ECI coordinate system defined by mean equator and equinox of 1 January 1950 [General Dynamics, 1978] and uses the matrix product ABCD to transform from ECI to ECR coordinates. D is a rotation matrix containing luni-solar and planetary precession terms necessary to transform from the mean equator and equinox of 1 January 1950 to the mean equator and equinox of date. C is a matrix containing nutation terms necessary to transform from the mean equator and equinox of date to the true equator and equinox of date. The B matrix converts from the true of date inertial system to an earth-fixed system by rotating through the Greenwich Hour Angle plus UT1-UTC and nutation (equation of the eqinoxes) terms and, finally, the A matrix contains polar motion rotation terms.

The onboard estimation algorithm has a choice of these two coordinate systems in which to perform its ephemeris calculations. If the ECR frame is chosen, conversions of output are unnecessary,

but the equations of motion are complicated by

$$\bar{a}_{ECR} = \bar{a}_I - 2\,\bar{\omega} \times \bar{v} - \bar{\omega} \times \bar{\omega} \times \bar{r}$$

where $\bar{\omega}$ is the angular velocity of the earth. The errors in $\bar{\omega}$ are not easily modeled, as the slope of the UT1-UTC curves gives the earth rotation error; thus errors in the spacecraft acceleration are difficult to predict in the ECR frame. In addition, the reconstruction of past performance of the navigation filter is complicated by the time-varying nature of $\delta\,\omega$. For these reasons, it is recommended that the onboard algorithm use an inertial (mean of 1950.0) frame for the ephemeris calculations.

CHAPTER 4

GPS ERROR ANALYSIS

4.1 Introduction

A relative autonomous navigation application for PS spacecraft will include an observation filter and an onboard model for ephemeris prediction. This model of the satellite dynamics is used for propagating the spacecraft state and error covariance between filter updates. The propagation interval varies from the 1.5 second doppler averaging time to a possible one- or two-hour delay between updates.

The method chosen to determine the requirements for the onboard model is a mixture of analytical and numerical techniques. Satellite-to-satellite range and doppler observations from satellites moving in similar orbit planes cannot provide information concerning a common secular motion of all satellite planes, but should be able to accurately observe differential planar and in-plane motions. In this investigation, secular planar motion caused by the various perturbing forces is determined analytically through examination of equations of motion of the orbit elements and numerically through a consider covariance analysis, while the effects of errors in model parameters upon planar and in-plane motion is determined through consider analysis. Figure 4.1 depicts the process by which the model is selected and analyzed. The model

99
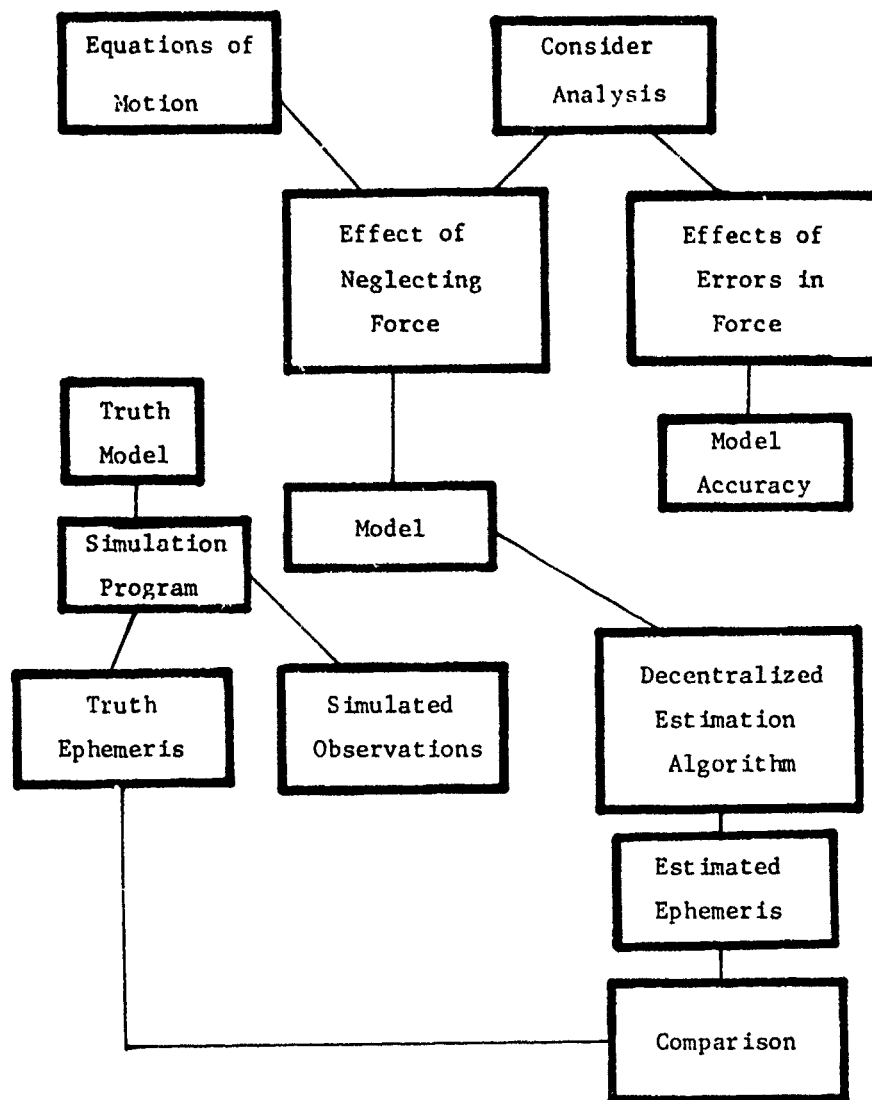
Figure 4.1.   Filter Model Selection and
              Evaluation Process

is then used in 18 decentralized estimation filters to propagate the state vectors of the 18 satellites. Observations produced by a high-order simulation program and corrupted by random measurement and clock noise are then processed by the estimation algorithm. The estimation output is compared to a truth ephemeris produced by the simulation program to determine the accuracy and stability of the proposed algorithm.

Since model error will be a prime consideration in the design of an onboard filter, this chapter starts with a discussion of the two prevailing techniques used to handle and quantify this error. The motion of GPS orbit planes is then analyzed, followed by a consider analysis of the expected relative navigation accuracy of the system. The objective of this chapter is to define a model to be used in the estimation algorithm proposed in Chapter 5, along with its expected performance.

4.2 Filter Divergence

As derived in Chapter 2, the state error covariance matrix, P , when propagated and updated by the Kalman filter equations (Eq. 2.4 and 2.8) gives an optimistic (low) value for the state error variance. In a filter where the state is being corrected through the inclusion of observations, this low value of P causes a low Kalman gain, K , which results in new data being ignored. If the true spacecraft state is given by the n-vector

$X(t)$ and an a priori estimate of this state is defined by $X^*(t)$, then define the state error by

$$x(t) = X(t) - X^*(t) \tag{4.1}$$

The nonlinear orbit determination problem, given by the state differential equation

$$\dot{X}(t) = F(X(t),t) \tag{4.2}$$

and the m-vector measurement equation at $t = t_i$

$$Y_i = G(X(t_i),t_i) + \epsilon_i \tag{4.3}$$

with $\epsilon_i \sim N(0,R_i)$, $R_i > 0$,

is then linearized by expressing $x(t)$ as a Taylor series expanded about the a priori estimate, $X^*(t)$ and Y_i as a Taylor series about $Y_i^* = G(X^*(t_i),t_i)$. The linear problem is then

$$\dot{x}(t) = A(t)x(t) \tag{4.4}$$

$$y_i = H_i \, x(t_i) + \epsilon_i$$

where

$$A(t) = \frac{\partial F(X(t),t)}{\partial X(t)}\bigg|_{X^*(t)} \tag{4.5}$$

$$H_i = \frac{\partial G(X(t_i),t_i)}{\partial X(t_i)}\bigg|_{X^*}(t_i) \tag{4.6}$$

An unbiased, minimum variance estimate of the state error

at $t = t_k$ is then given by Jazwinski [1970, p. 198] as

$$\hat{x}_k = \bar{x}_k + K_k(y_k - H_k\bar{x}_k) \tag{4.7}$$

where

$$\bar{x}_k = \phi(t_k, t_{k-1})\hat{x}_{k-1} \tag{4.8}$$

and $\phi(t_k, t_{k-1})$ is defined by Eq. (2.5).

Note that in Eq. (4.7), the propagated state error estimate, $\bar{x}_k$ is updated by observation residuals, y_k , multiplied by K_k so that if the covariance matrix, $\bar{P}$, drops to unrealistically low values, the gain $K_k = \bar{P}H^T(H\bar{P}H^T + R)^{-1}$ becomes small, and the updated state error $\hat{x}_k$ is not sensitive to the observations. This leads to the well-known symptom of filter divergence where residuals become large and, finally, the state error grows to values much larger than the error bounds expressed by the variances in P .

The cause of filter divergence is the assumption that reality is correctly modeled by the two sets of equations, $F(x(t),t)$ and $G(x(t_i),t_i)$ when, in fact, our knowledge of the real forces acting on a spacecraft and of the actual physics involved in a measurement process is quite limited. Even if we had perfect knowledge of the forces and measurements involved, the solutions to the state differential and measurement equations are only approximated on a digital computer. The two major errors, approximation of the equations solutions by finite series or

numerical integration (truncation error) and finite computer word length (round-off) would continue to give errors for $x(t)$ and y_i .

Filter divergence is not observed in pre-mission covariance analyses because observations are not being processed to produce state errors. A Monte Carlo analysis in which a more sophisticated model generates observations for use in a lower order filter can be used to evaluate this phenomenon. Covariance analysis results do, however, suffer from the effects of model error. The state error variance is optimistically low and desired information about the effect of unmodeled errors is not produced.

4.3 State Noise Covariance Analysis

To combat the problem of filter divergence or an unrealistic covariance matrix, estimation algorithms can employ state noise or model noise compensation [Jazwinski, 1970, pp. 244-247]. Instead of the "perfect" model assumed in Eq. (4.4), let us assume that our state differential equations are corrupted by a Brownian motion process such that

$$\dot{x}(t) = A(t)x(t) + B(t)d\beta(t) \qquad (4.9)$$

$$y_i = H_i x(t_i) + \epsilon_i$$

where $B(t)$ is a non-random matrix that maps the r-vector $d\beta(t)$ into the n space of $x(t)$ and

$$E[d\beta(t)] = 0 \tag{4.9}$$

$$E[d\beta(t)d\beta^T(t)] = Q(t)dt \qquad Q(t) > 0 \tag{4.10}$$

$$E[d\beta(t)d\beta^T(\tau)] = Q\delta(t-\tau) \qquad \delta = \text{dirac delta} \tag{4.11}$$

$$E[d\beta(t)\epsilon_i^T] = 0 \tag{4.12}$$

The state error is then propagated from t_k to t by

$$x(t) = \phi(t,t_k)x(t_k) + \int_{t_k}^{t} \phi(t,\tau)B(\tau)d\beta(\tau). \tag{4.13}$$

To propagate P, first look at the propagation of P without model noise.

$$\overline{P}(t) = \phi(t,t_k)P(t_k)\phi^T(t,t_k) \tag{4.14}$$

Differentiating,

$$\dot{\overline{P}}(t) = \dot{\phi}(t,t_k)P(t_k)\phi(t,t_k)$$

$$+ \phi(t,t_k)P(t_k)\dot{\phi}^T(t,t_k) \tag{4.15}$$

and substituting for $\dot{\phi}(t,t_k)$

$$\dot{\phi}(t,t_k) = A(t)\phi(t,t_k) \tag{4.16}$$

we arrive at the matrix Riccati equation:

$$\dot{\overline{P}}(t) = A(t)\phi(t,t_k)P(t_k)\phi^T(t,t_k)$$

$$+ \phi(t,t_k)P(t_k)\phi^T(t,t_k)A^T(t)$$

$$= A(t)\overline{P}(t) + \overline{P}(t)A^T(t). \tag{4.17}$$

Now, for the case of model noise, if $\hat{x}(t)$ is an unbiased estimator of the state error $x(t)$ and $t > t_k$ [Maybeck 1979, pp. 164-167],

$$\hat{x}(t) = E[x(t) \mid y_i \ , \quad i=1,\ldots,k] \tag{4.18}$$

and the covariance is defined as

$$P(t) = E[(x(t) - \hat{x}(t))(x(t) - \hat{x}(t))^T]$$

$$= E[\Delta x(t)\Delta x^T(t)] \tag{4.19}$$

where

$$\Delta x = x(t) - \hat{x}(t) = \phi(t,t_k)x(t_k)$$

$$+ \int_{t_k}^{t} \phi(t,\tau)B(\tau)d\beta(\tau) - \phi(t,t_{k-1})\hat{x}(t_{k-1})$$

$$= \phi(t,t_k)\Delta x(t_k) + \int_{t_k}^{t} \phi(t,\tau)B(\tau)d\beta(\tau) \tag{4.20}$$

then

$$\overline{P}(t) = E[\{\phi(t,t_k)\Delta x(t_k) + \int_{t_k}^{t} \phi(t,\tau)B(\tau)d\beta(\tau)\}$$

$$\{\phi(t,t_k)\Delta x(t_k) + \int_{t_k}^{t} \phi(t,\tau)B(\tau)d\beta(\tau)\}^T]$$

$$= E[\phi(t,t_k)\Delta x(t_k)\Delta x^T(t_k)\phi^T(t_k)]$$

$$+ E[\phi(t,t_k)\Delta x(t_k) \int_{t_k}^{t} d\beta^T(\tau)B^T(\tau)\phi^T(t,\tau)]$$

$$+ E[\int_{t_k}^{t} \phi(t,\tau)B(\tau)d\beta(\tau) \phi(t,t_k)\Delta x(t_k)]$$

$$+ [\int_{t_k}^{t}\int_{t_k}^{t} \phi(t,\tau)B(\tau)d\beta(\tau)d\beta^T(s)B^T(s)\phi^T(t,s)]. \qquad (4.21)$$

Now, assuming that $\Delta x(t_k)$ and $d\beta(\tau)$ for $\tau \geq t_k$ are uncorrelated, i.e.,

$$E[\Delta x(t_k)d\beta^T(\tau), \quad \tau \geq t_k] = 0 \qquad (4.22)$$

and noting that $\phi(t,\tau)$ and $G(\tau)$ are non-random, and that

$$E[d\beta(\tau)d\beta(s)] = Q\delta(\tau-s) , \qquad (4.23)$$

$$\overline{P}(t) = \phi(t,t_k)P(t_k)\phi^T(t,t_k)$$

$$+ \int_{t_k}^{t} \phi(t,\tau)B(\tau)Q(\tau)B^T(\tau)Q^T(t,\tau)d\tau \qquad (4.24)$$

Differentiating by Leibnitz rule and using Eq. (4.16),

$$\dot{\overline{P}}(t) = A(t)\phi(t,t_k)P(t_k)\phi^T(t,t_k) + \phi(t,t_k)P(t_k)\phi^T(t,t_k)A^T(t)$$

$$+ \phi(t,\tau)B(\tau)Q(\tau)B^T(\tau)\phi^T(t,\tau)|_{\tau=t_k}^{\tau=t}$$

$$+ \int_{t_k}^{t} [A(t)\phi(t,\tau)B(\tau)Q(\tau)B^T(\tau)\phi^T(t,\tau)$$

$$+ \phi(t,\tau)B(\tau)Q(\tau)B^T(\tau)\phi^T(t,\tau)A^T(t)]d\tau$$

$$\dot{\overline{P}}(t) = A(t)\overline{P}(t) + \overline{P}(t)A^T(t) + B(t)Q(t)B^T(t) \qquad (4.25)$$

Eq. (4.25) shows that, since $Q(t) > 0$, the covariance grows between t_k and t_{k+1} by the integral of $B(t)Q(t)B^T(t)$, where the matrix Q describes the error variance of the state differential equation model error. This technique of augmenting the P matrix by a Q matrix is in common use in filter algorithms. The Space Sextant software incorporates the Q matrix formulation [Martin-Marietta, 1981] and it is used in the GPS navigation algorithm proposed in Chapter 5.

4.4 Sequential Consider Covariance Formulation

The state noise compensation method described in Section 4.3 prevents filter divergence when proper values for state noise are used in the Q matrix. However, it has three disadvantages when used for covariance analyses. First, the values describing state differential equation noise tend to be arrived at in an ad hoc fashion since the actual errors are unknown, just as the actual force acting on the spacecraft over time is unknown. Second, and more important from an error analysis viewpoint, is the difficulty in isolating and evaluating the effect of specific errors in the state model on the error covariance. Third, it is impractical to analyze the effect of estimating a parameter that is causing large errors, because the entire filter must then be redesigned.

To overcome these difficulties, consider analysis has come

into widespread use. This technique allows the effect of errors in model parameters upon the dynamic state to be considered. Bierman [1977, pp. 162-171] describes a batch processor in which the state vector is partitioned into a set of variables and parameters that are to be estimated and a set of parameters whose effect is only to be considered. After processing a fictitious set of noisy observations, his algorithm then propagates the entire covariance through desired time intervals to determine the state error in the future.

In the GPS scenario, however, observations would be processed onboard in a sequential filter, thus the sequential covariance analysis proposed by Maybeck [1979, pp. 325-336] is used. This method assumes that a high-order "truth model" is available that adequately represents the real world. It is given by the linearized continuous differential equation

$$\dot{\xi}_t(t) = A_t(t)\xi_t(t) + G_t(t)w_t(t) \tag{4.28}$$

where $\dot{\xi}_t(t)$ is an n_t vector and $w_t(t)$ is an S_t vector zero-mean white Gaussian noise sequence, with

$$E[\xi_t(t_o)] = 0 \tag{4.29}$$

$$E[\xi_t(t_o)\xi_t^T(t_o)] = P_{t_o} \tag{4.30}$$

Discrete measurements available from this model are obtained by

$$y_t(t_i) = H_t(t_i)\xi_t(t_i) + \epsilon_t(t_i) \tag{4.31}$$

with

$$E[\epsilon_t(t_i)] = 0 \tag{4.32}$$

$$E[\epsilon_t(t_i)\epsilon_t^T(t_j)] = \left.\begin{array}{l} R_t(t_i) \\ 0 \end{array}\right\} \begin{array}{l} t_i = t_j \\ t_i \neq t_j \end{array} \tag{4.33}$$

For consider analysis, the state vector ξ_t contains both the spacecraft dynamic state and constant model parameters. The dynamic state, which is of interest at each time t, is separated by $\xi_t(t)$ by

$$x_t(t) = C_t\xi_t(t). \tag{4.34}$$

After arranging ξ_t in a manner consistent with the desired outcome, the C_t matrix can be partitioned into a $p \times p$ identity matrix and a $p \times n_t\text{-}p$ null matrix.

The "truth model" is then used as a basis with which to compare several reduced order candidate linear "filter models," each described by the n-vector differential equation

$$\dot{\hat{\xi}}(t) = F(t)\hat{\xi}(t) \tag{4.35}$$

with

$$E[\hat{\xi}(t_o)] = 0 \tag{4.36}$$

$$E\left[\hat{\xi}(t_o)\hat{\xi}^T(t_o)\right] = P_o \tag{4.37}$$

and updated by measurements modeled by

$$\mathcal{Y}(t_i) = H(t_i)\hat{\xi}(t_i) + \epsilon(t_i) \tag{4.38}$$

with

$$E\left[\epsilon(t_i)\right] = 0 \tag{4.39}$$

$$E\left[\epsilon(t_i)\epsilon^T(t_j)\right] = \left.\begin{array}{l} R(t_i) \\ 0 \end{array}\right\} \begin{array}{l} t_i = t_j \\ t_i \neq t_j \end{array} \tag{4.40}$$

The Kalman filter for these filter models is the same as described in Section 4.2. Again, only a subset of this state vector contains dynamic terms, thus

$$x(t) = C\xi(t) \tag{4.41}$$

where C is a p x p identity matrix plus a p x n-p null matrix.

To compare these two models, form the augmented state vector

$$\xi_a(t) = \begin{bmatrix} \xi_t(t) \\ \hat{\xi}(t) \end{bmatrix} \tag{4.42}$$

with

$$P_a(t_o) = E\left[\xi_a(t_o)\xi_a^T(t_o)\right] = \begin{bmatrix} P_{t_o} & 0 \\ 0 & P_o \end{bmatrix} \tag{4.43}$$

This augmented state is propagated by

$$\overline{\xi}_a(t_k) = \phi_a(t_k, t_{k-1})\hat{\xi}_a(t_{k-1}) \tag{4.44}$$

where $\phi_a(t_k, t_{k-1})$ is an $(n_t+n) \times (n_t+n)$ state transition matrix that satisfies

$$\dot{\phi}_a(t, t_{k-1}) = A_a(t)\phi_a(t, t_{k-1}) \tag{4.45}$$

with

$$\phi_a(t_{k-1}, t_{k-1}) = I \tag{4.46}$$

and

$$A_a(t) = \begin{bmatrix} A_t(t) & 0 \\ 0 & A(t) \end{bmatrix} \tag{4.47}$$

Since the state vectors $\xi_t(t)$ and $\hat{\xi}(t)$ contain both dynamic and constant terms and the consider analysis produces a time history of state errors due to these terms, it is convenient to represent ϕ_a by its components. The two dynamic state transition matrices are

$$\phi_t(t_k, t_{k-1}) = \frac{\partial x_t(t_k)}{\partial x_t(t_{k-1})} \tag{4.48}$$

and

$$\phi(t_k, t_{k-1}) = \frac{\partial x(t_k)}{\partial x(t_{k-1})} \tag{4.49}$$

while the two state parameter transition matrices are

$$\psi_t(t_k,t_{k-1}) = \frac{\partial x_t(t_k)}{\partial C_t^* \xi_t(t_{k-1})} \tag{4.50}$$

and

$$\psi(t_k,t_{k-1}) = \frac{\partial x(t_k)}{\partial C^* \hat{\xi}(t_{k-1})} \tag{4.51}$$

where C_t^* and C^* select the parameters contained in ξ_t and $\hat{\xi}$.

The augmented state covariance is moved forward in time via

$$\overline{P}_a(t_k) = \phi_a(t_k,t_{k-1})P_a(t_{k-1})\phi_a^T(t_k,t_{k-1}) \tag{4.52}$$

Measurement processing gives the state measurement update:

$$\hat{\xi}_a(t_k) = M_a(t_k)\overline{\xi}_a(t_k) \tag{4.53}$$

where

$$M_a(t_k) = \begin{bmatrix} I & 0 \\ K(t_k)H_t(t_k) & [I-K(t_k)H(t_k)] \end{bmatrix} \tag{4.54}$$

and $H_t(t_k)$ contains partials of the measurement with respect to the entire truth model state.

The covariance is updated by

$$P_a(t_k) = M_a(t_k)\overline{P}_a(t_k)M_a^T(t_k)$$
$$+ K_a(t_k)R_t(t_k)K_a^T(t_k) \tag{4.55}$$

where

$$K_a(t_k) = \begin{bmatrix} 0 \\ K(t_k) \end{bmatrix} \qquad (4.56)$$

Note that the covariance of interest is actually

$$P_\eta(t) = E[\eta_t(t)\eta_t^T(t)] \qquad (4.57)$$

where

$$\eta(t) = x(t) - x_t(t) \qquad (4.58)$$

This covariance is obtained from $P_a(t)$ by

$$P_\eta(t) = C_a P_a(t) C_a^T \qquad (4.59)$$

where

$$C_a = [-C_t \mid C] \qquad (4.60)$$

If $x(t)$ consists of $\bar{r}$ and $\bar{v}$, then P_η contains the sum of the 6×6 upper left submatrices of P_t and P .

This approach to state covariance analysis assumes that the filter operates independently of the higher order truth model and that the errors in the truth model given by P_{t_o} are realistic. If this is true, $P_\eta(t)$ will represent the actual errors exhibited by the filter in use. As in the state noise compensation technique, however, the actual error of a dynamic or geometric parameter may not be known. In this study, normalized partials are used to

determine the sensitivity of the state to a unit error in each of the parameters.

4.5 Application to GPS Autonomous Navigation

COVSEQ is a computer program devised to implement the sequential consider covariance analysis method for a GPS satellite navigation receiver. Variables and parameters estimated or considered in the program are given in Table 4.1.

The program makes use of the propagation capabilities of the University of Texas Orbit Processor (UTOPIA) to obtain a user satellite file containing the spacecraft state $(\overline{r}(t), \overline{v}(t))$ and partial derivatives, $\phi_a(t,t_o)$ for the several parameters available in UTOPIA. Since UTOPIA does not produce partials for the state with respect to lunar and solar mass and position errors, these partials, along with all geometric measurement partials, are computed in COVSEQ. UTOPIA produces $\phi(t,t_0)$ and $\psi(t,t_0)$, while COVSEQ requires $\phi(t_{j+1},t_j)$ and $\psi(t_{j+1},t_j)$. This converrsion is described in Appendix A. The output of COVSEQ is a time history of the error covariance, P_n, after a set of GPS range and/or integrated doppler observations is processed at each desired step. The error covariance is propagated according to Eq. (4.52) and updated at each observation time by Eq. (4.55).

TABLE 4.1

COVSEQ VARIABLES AND PARAMETERS

Name	Estimate	Consider	Source of Partials	Typical 1σ Value or Scale Value
User $\bar{r}$, $\bar{v}$	Yes	No	UTOPIA	10 m, .002 m/s
Range, Range-Rate	No	Yes	COVSEQ	3.4 m, .05 m/s
c_{nm}, S_{nm}	Yes	Yes	UTOPIA	10^{-6}
Radial Acceleration	Yes	Yes	UTOPIA	10^{-6} m/s^2
Tangential Acceleration	Yes	Yes	UTOPIA	10^{-6} m/s^2
Normal Acceleration	Yes	Yes	UTOPIA	10^{-6} m/s^2
Solar Radiation Pressure	Yes	Yes	UTOPIA	1% (.015)
Atmospheric Drag	Yes	Yes	UTOPIA	0 for GPS
GPS Radial Position	Yes	Yes	COVSEQ	2 m periodic
GPS Tangential Position	Yes	Yes	COVSEQ	10 m periodic + drift
GPS Normal Position	Yes	Yes	COVSEQ	6 m periodic
User Clock Bias	Yes	Yes	COVSEQ	10^{-8} sec
User Clock Drift	Yes	Yes	COVSEQ	1×10^{-12} sec/sec
GPS Clock Bias	Yes	Yes	COVSEQ	10^{-8} sec
GPS Clock Drift	Yes	Yes	COVSEQ	1×10^{-12} sec/sec

4.5.1 Pseudo-Range Observation Partials

Measurements available to the GPS vehicle include pseudo-range and integrated doppler counts. For the L_3 crosslink, the pseudo-range model is given in Eq. (3.1) and state and consider partials are:

$$H_x(t_k) = \left[\frac{x - x_{g_i}}{\rho_i} \quad \frac{y - y_{g_i}}{\rho_i} \quad \frac{z - z_{g_i}}{\rho_i} \quad 0 \quad 0 \quad 0 \quad \dots \right.$$

$$\left. \dots \quad \frac{1}{c} \frac{\partial \overline{\rho}_i}{\partial \Delta t_u} \quad \frac{1}{c} \frac{\partial \overline{\rho}_i}{\partial \Delta f_u} \quad \frac{1}{c} \frac{\partial \overline{\rho}_i}{\partial \overline{r}_{s_i}} \quad \frac{1}{c} \frac{\partial \overline{\rho}_i}{\partial \Delta t_{s_i}} \quad \frac{1}{c} \frac{\partial \overline{\rho}_i}{\partial \Delta f_{s_i}} \right] \tag{4.61}$$

where $\overline{\rho}_i$, Δt_u, and Δt_{s_i} are defined in Section 3.2 and the other geometric partials are given by

$$\frac{1}{c} \frac{\partial \overline{\rho}_i}{\partial \Delta f_u} = t - t_o \tag{4.62}$$

= sensitivity of observation to a user clock frequency bias

$$\frac{\partial \overline{\rho}_i}{\partial \overline{r}_{s_i}} = \left[\frac{\partial \overline{\rho}_i}{\partial x_{s_i}} \quad \frac{\partial \overline{\rho}_i}{\partial y_{s_i}} \quad \frac{\partial \overline{\rho}_i}{\partial z_{s_i}} \right]$$

$$= - \left[H_{x_1} \quad H_{x_2} \quad H_{x_3} \right] \left[T_{ECI}^{RTN} \right] \tag{4.63}$$

= sensitivity of observation to GPS ephemeris errors

expressed in a GPS-centered RTN coordinate system

$$\frac{1}{c}\frac{\partial \bar{\rho}_i}{\partial \Delta t_{s_i}} = -1 \qquad (4.64)$$

= sensitivity of observation to a GPS clock phase bias

$$\frac{1}{c}\frac{\partial \bar{\rho}_i}{\partial \Delta f_{s_i}} = -(t - t_o) \qquad (4.65)$$

= sensitivity of observation to a GPS clock frequency bias

4.5.2 Doppler Measurement Model

When a signal of frequency f_g is transmitted by a moving source from t_1 to t_2 and received by a moving receiver between τ_1 and τ_2, the received frequency, f_r, differs from f_g due to the well-known doppler shift. When the received frequency is compared to a known oscillator output, f_u, the resulting difference is then integrated to produce the doppler count:

$$N = \int_{\tau_1}^{\tau_2} (f_u - f_r)d\tau$$

$$= \int_{\tau_1}^{\tau_2} f_u d\tau - \int_{\tau_1}^{\tau_2} f_r d\tau , \qquad (4.66)$$

but f_r undergoes the same number of oscillations during $\tau_2 - \tau_1$ as does f_g between t_2 and t_1 , thus

$$N = \int_{\tau_1}^{\tau_2} f_u d\tau - \int_{t_1}^{t_2} f_g \, d\tau \, . \tag{4.67}$$

Now assuming that f_u and f_g are the result of stable oscillators such that they are constant during the intervals used and noting that τ and t are related by

$$\tau = t + \frac{\rho}{c} \tag{4.68}$$

where ρ is the geometric range and c the speed of light $(c \sim 3.0 \times 10^8 \text{ m/s})$, the doppler count is then

$$N = f_u(\tau_2 - \tau_1) - f_g(t_2 - \tau_1) + \frac{f_g}{c}(\rho_2 - \rho_1)$$

$$= (f_u - f_g)(\tau_2 - \tau_1) + \frac{f_g}{c}(\rho_2 - \rho_1) \tag{4.69}$$

Since Eq. (4.69) was obtained for perfect frequency standards, it must be modified to include errors in frequency, even though they are small for GPS clocks. Expressing the true oscillator output as a nominal frequency, f^*, plus a first-order term, Δf, Eq. (4.69) becomes

$$N = (f_u^* - f_g^*)(\tau_2 - \tau_1) + (\Delta f_u - \Delta f_g)(\tau_2 - \tau_1)$$

$$+ \left[\frac{f_g^* + \Delta f_g}{c} \right](\rho_2 - \rho_1). \tag{4.70}$$

Noting that for GPS-to-GPS communication $f_u^* = f_g^*$, and multiplying both sides by $\frac{c}{f_g^*}$,

$$\frac{cN}{f_g^*} = c \left[\frac{\Delta f_u}{f_g^*} - \frac{\Delta f_g}{f_g^*} \right] (\tau_2 - \tau_1) + \left[1 + \frac{\Delta f_g}{f_g^*} \right] (\rho_2 - \rho_1) \qquad (4.71)$$

Now, f_g^* for L_3 is approximately 10^9 Hz, while the frequency stability, $\Delta f/f$ is on the order of 10^{-12}, thus $\frac{\Delta f}{f} \ll 1$. Note also that $\frac{cN}{f_g^*}$ represents a delta range measurement, thus

$$\Delta \rho \doteq c(\delta f_u - \delta f_g)(\tau_2 - \tau_1) + \rho_2 - \rho_1 \qquad (4.72)$$

where $\delta f = \frac{\Delta f}{f}$.

4.5.3 Doppler Partial Derivatives

The partial derivatives of $\Delta \rho$ can be computed at either τ_1 or τ_2. Assuming that the receiver integrates from τ_1 to τ_2 and then estimates the spacecraft state at τ_2, the observation-state partial derivatives are:

a. Position and Velocity

$$\frac{\partial \Delta \rho}{\partial X(\tau_2)} = \frac{\partial \rho(\tau_2)}{\partial X(\tau_2)} - \frac{\partial \rho(\tau_1)}{\partial X(\tau_1)} \frac{\partial X(\tau_1)}{\partial X(\tau_2)}$$

$$= \left[\frac{-\rho_x}{\rho} \ \frac{-\rho_y}{\rho} \ \frac{-\rho_z}{\rho} \ 0 \ 0 \ 0 \right]_{\tau_2}$$

$$- \left[\frac{-\rho_1}{\rho} \ \frac{-\rho_2}{\rho} \ \frac{-\rho_3}{\rho} \ 0 \ 0 \ 0 \right]_{\tau_1} \phi(\tau_1, \tau_2) \qquad (4.73)$$

where $\phi(\tau_1, \tau_2)$ is the state transition matrix from τ_1 to τ_2 .

b. User Clock Bias and Drift

$$\frac{\partial \Delta \rho}{\partial \Delta t_u} = 0 \qquad\qquad (4.74)$$

$$\frac{\partial \Delta \rho}{\partial \delta \dot{r}_u} = \tau_2 - \tau_1 \qquad\qquad (4.75)$$

c. GPS Clock Bias and Drift

$$\frac{\partial \Delta \rho}{\partial \Delta t_s} = 0 \qquad\qquad (4.76)$$

$$\frac{\partial \Delta \rho}{\partial \delta \dot{r}_g} = -(\tau_2 - \tau_1) \qquad\qquad (4.77)$$

4.6 Model Determination

4.6.1 Geopotential Coefficients

The major geopotentiaal source of secular motion of satellite planes is the well-known J_2 perturbation. J_2 mathematically models the equatorial bulge and causes a regression of the nodes given by

$$\dot{\Omega}_{J_2} = -\frac{3}{2} J_2 \left[\frac{R_e}{a(1-e^2)} \right]^2 n \cos i \qquad\qquad (4.78)$$

where

   R_e = equatorial radius of the earth

   a = orbit semi-major axis

   e = orbit eccentricity

   n = orbit mean motion

i = orbit inclination

The effect of neglecting J_2 is shown in Figure 4.2, where it is seen that the error normal to the original plane of 873.6 km builds up over 60 days.

The other main geopotential perturbations are due to terms which are resonant with the 12-hour orbit period. These terms (1/2 and 1/4) do not cause large short-term (less than one day) out-of-plane motions but can lead to along-track errors large enough to affect user navigation accuracy. Figures 4.3 through 4.8 show the error growth due to neglecting these terms, while Figure 4.9 shows the worst-case out-of-plane error due to neglecting C,S 3/2. The in-plane error plots also include the error due to propagating initial position and velocity errors. This error reaches 38.459 km, and when it is removed from the analysis, the remaining in-plane and cross-track errors are as shown in Table 4.2.

TABLE 4.2

CONTRIBUTIONS DUE TO NEGLECTING
GEOPOTENTIAL TERMS

Neglected Term	Maximum Error After 60 Days (km)	Contribution of Geopotential (km)	Out-of-Plane Motion (m)
J_2	2064.340	1925.871	873608.0
C,S 2/2	44.669	6.214	17.6
C,S 3/2	167.363	128.897	355.0
C,S 5/2	39.038	0.569	0.0
C,S 7/2	38.4595	1×10^{-6}	0.0
C,S 4/4	53.3249	21.086	0.0
C,S 6/4	38.4637	0.005	0.0
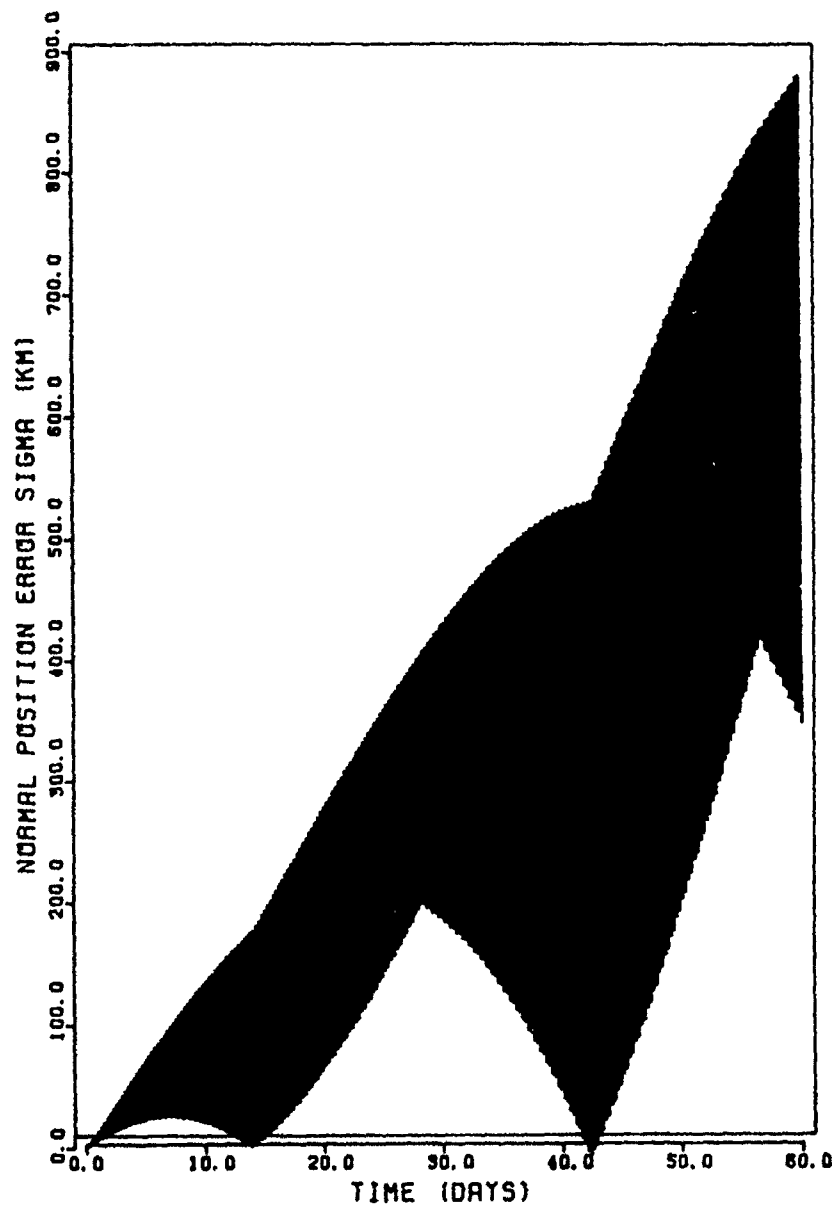
Figure 4.2. Predicted Normal Position Error with
                J$_2$ Neglected.
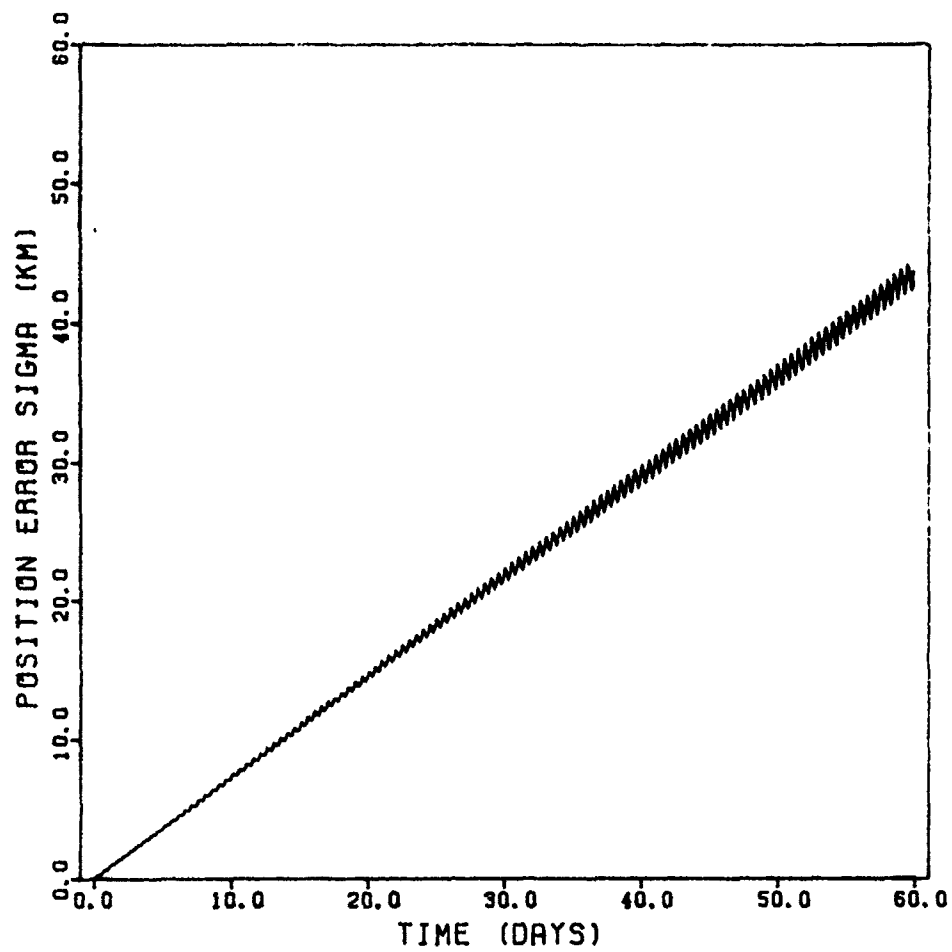
Figure 4.3. Predicted Position Error with C_{22} and S_{22} Neglected.
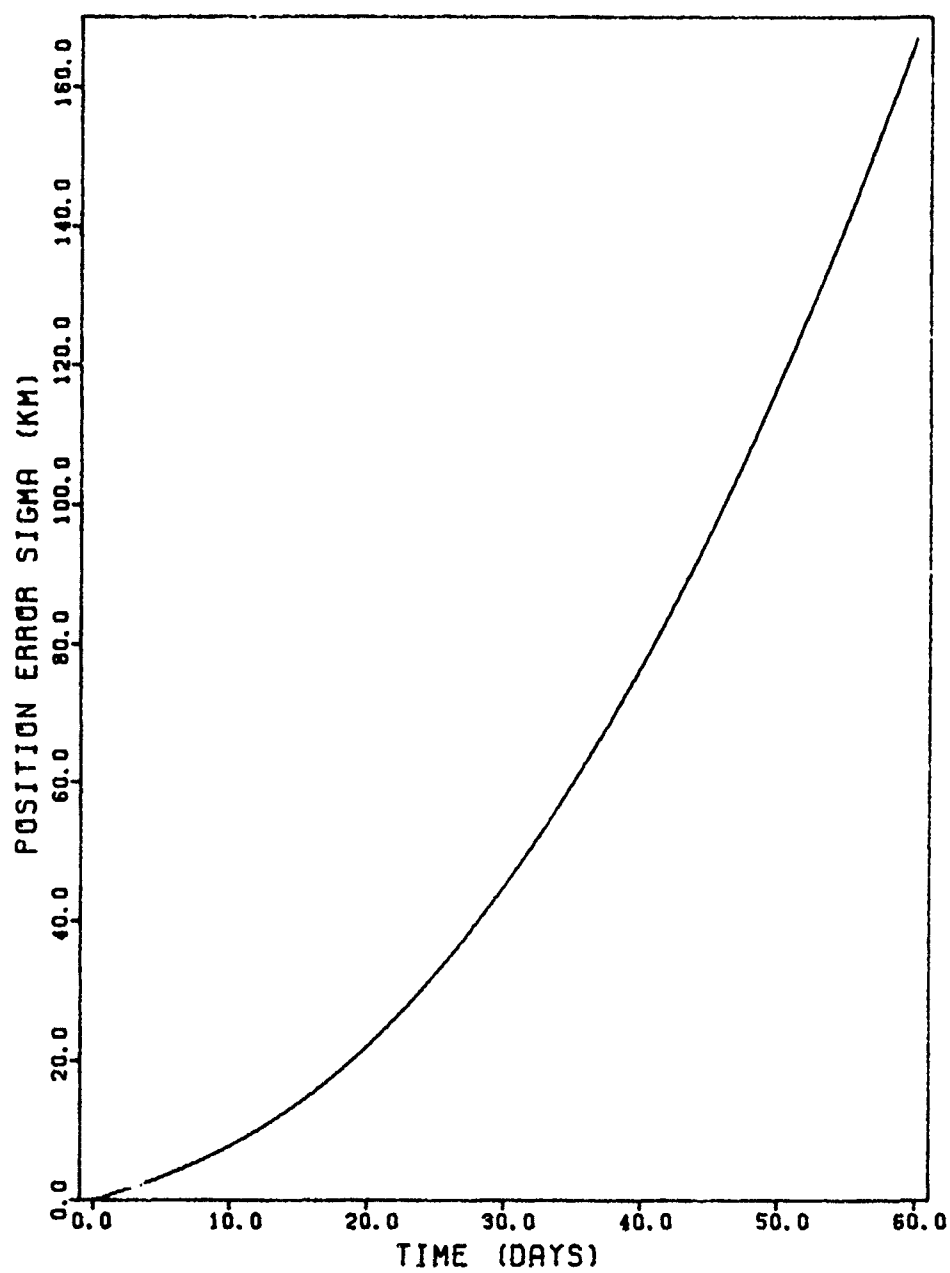
Figure 4.4. Predicted Position Error with C_{32} and S_{32} Neglected.
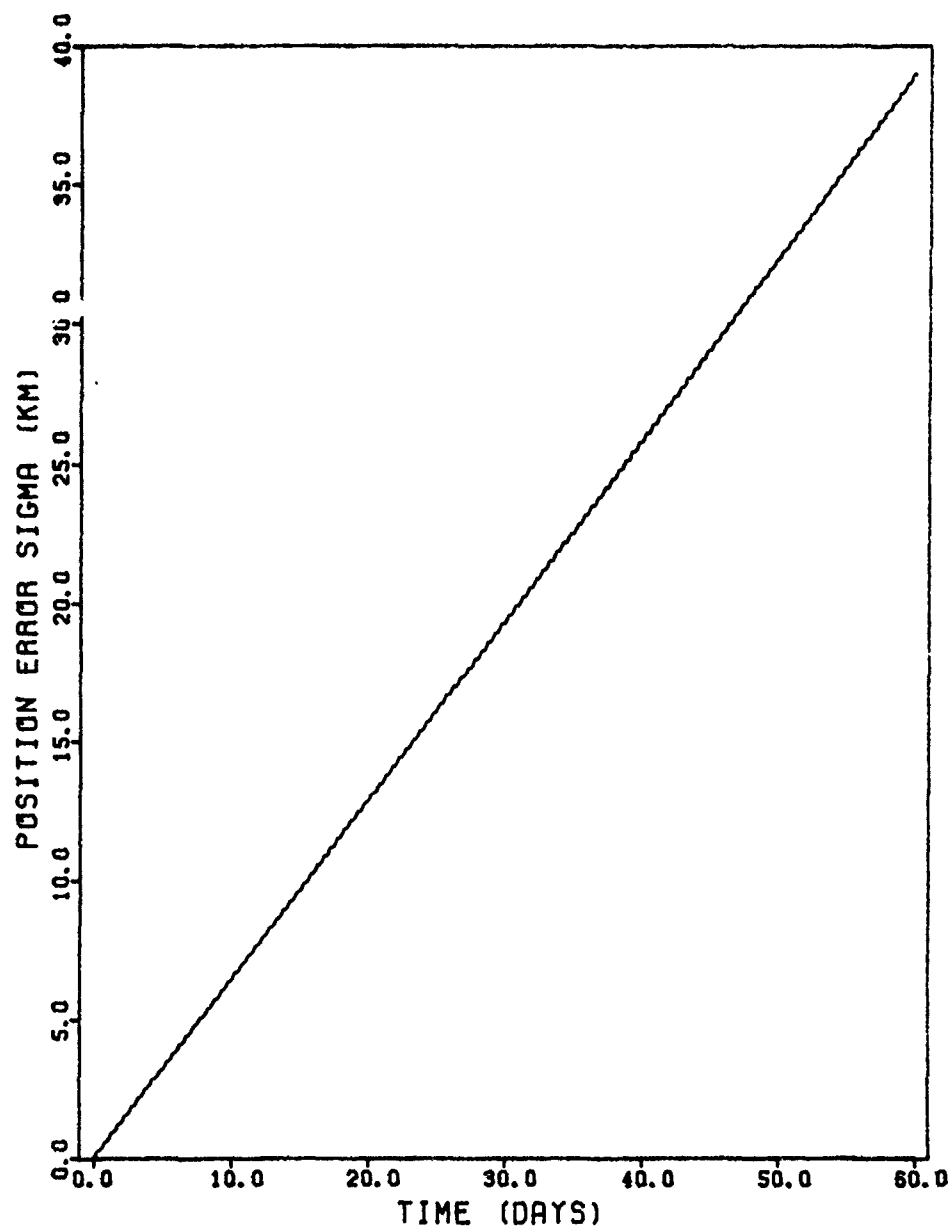
Figure 4.5. Predicted Position Error with C_{52} and S_{52} Neglected.
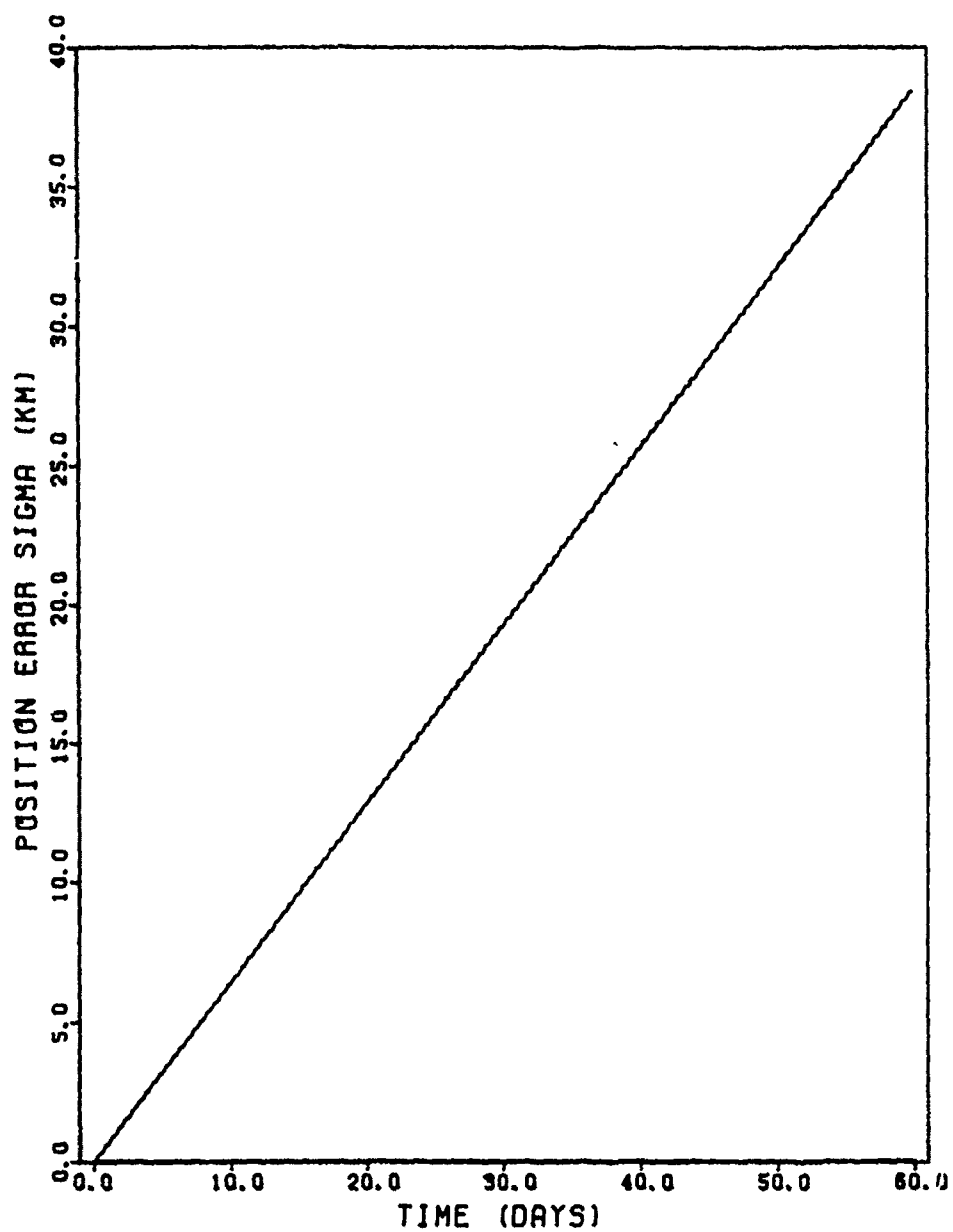
Figure 4.6.   Predicted Position Error with C_{72} and S_{72} Neglected.
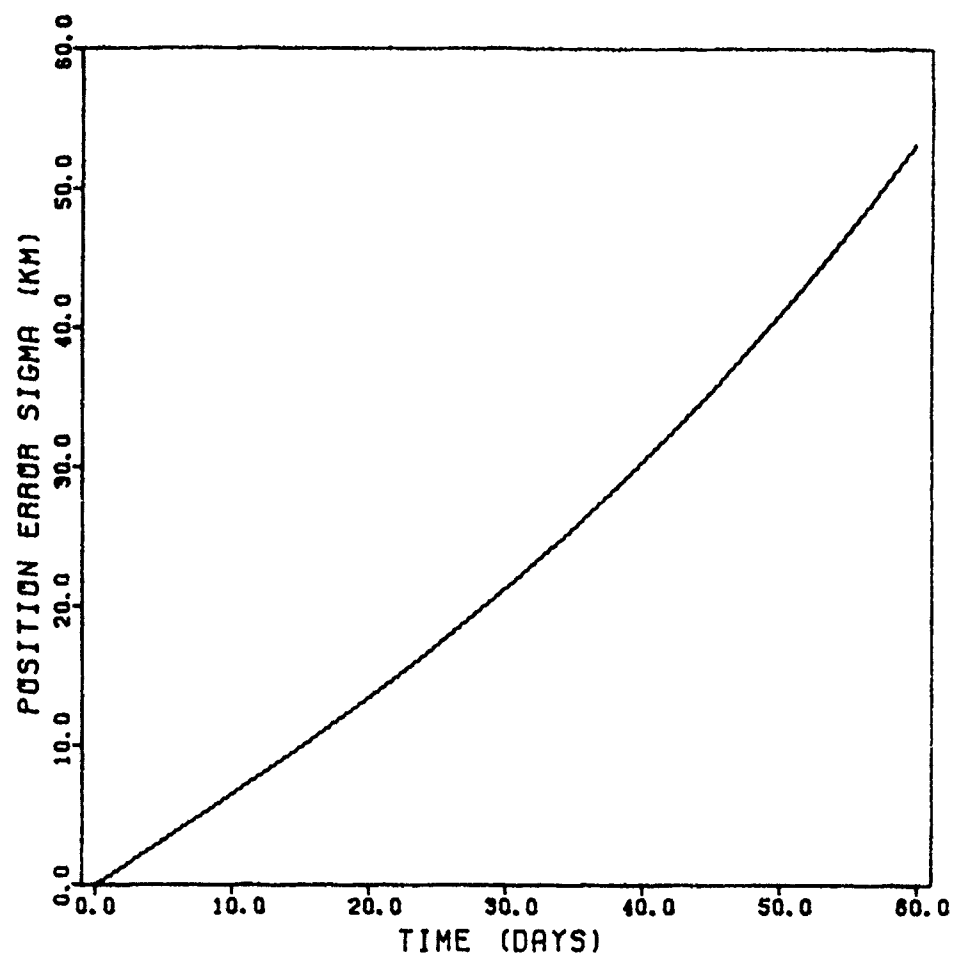
Figure 4.7. Predicted Position Error with C_{44} and S_{44} Neglected.
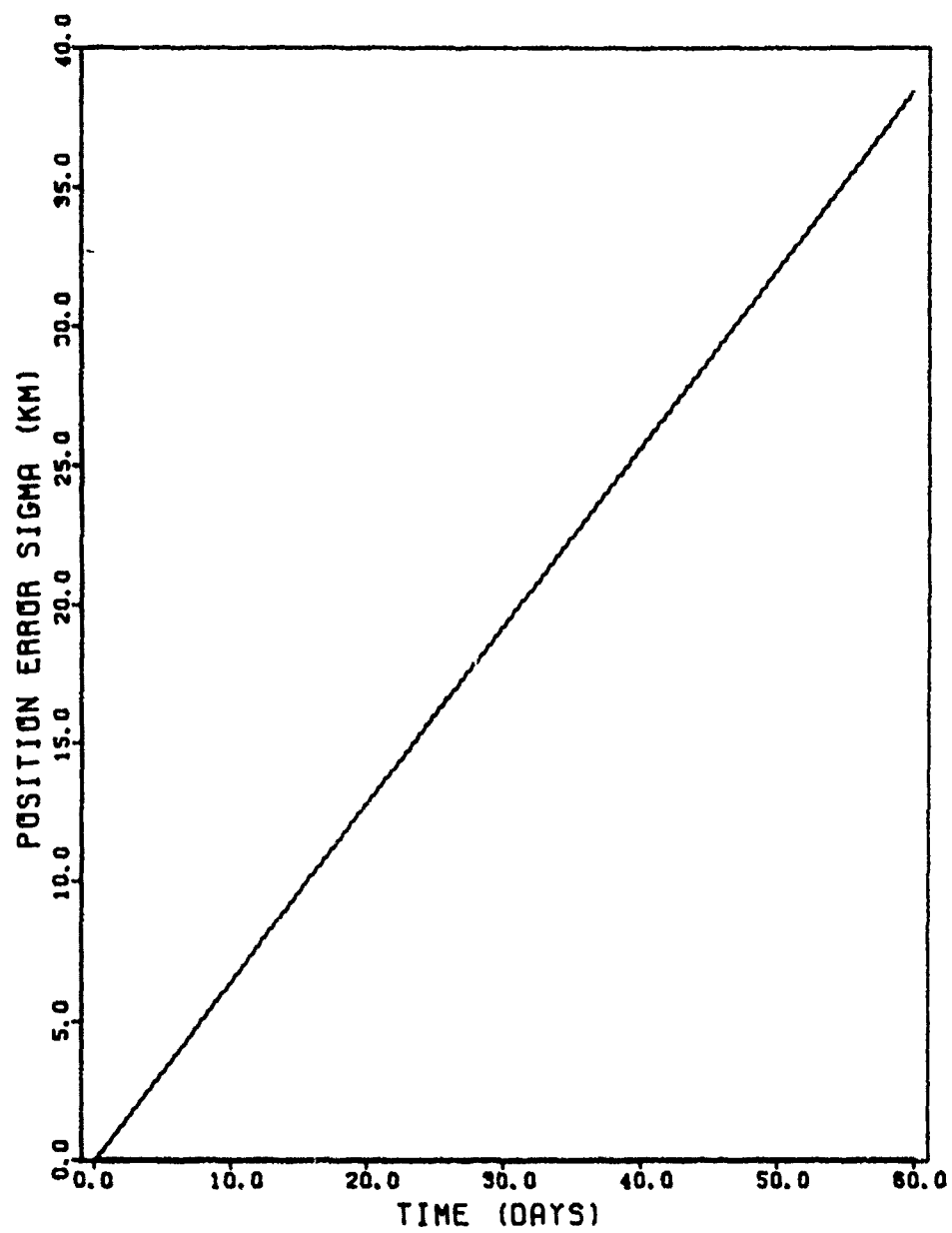
Figure 4.8. Predicted Position Error with C_{64} and S_{64} Neglected
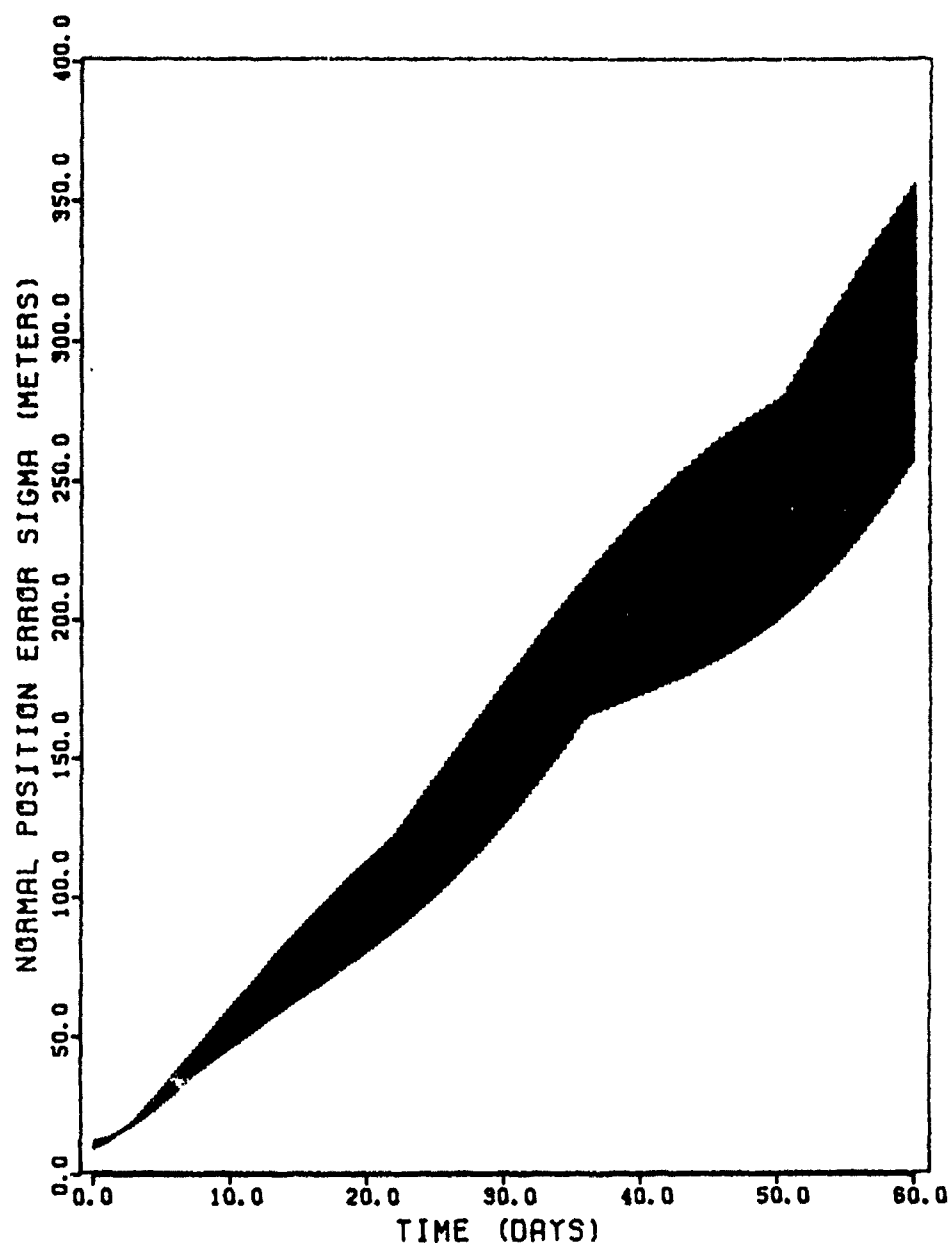
Figure 4.9.   Predicted Normal Position Error with
C_{32} and S_{32} Neglected.

These results show that a model used to predict over time intervals longer than one hour should include J_2 and C,S 3/2 and 4/4 terms, while predictions of approximately 10 m accuracy over one hour can be achieved with J_2 and C,S 3/2. Note that the out-of-plane motion due to the J_2-induced regression of the nodes is the major secular planar effect and that C,S 3/2 cause a smaller but significant motion of the orbit plane.

4.6.2 Solar Radiation Pressure

The effect of neglecting solar radiation pressure is shown in Figure 4.10, with the maximum error being 2606.9 m. For this case, the effects are almost entirely in-plane, but periodic planar movement can be determined from equations as given by Geyling and Westerman [1971, p. 123] as

$$\dot{i} \simeq - \frac{F_p \sin \alpha \sin i_o (\sin \theta_2 - \sin \theta_1)}{n^2 \, m \, r_o} \tag{4.79}$$

and

$$\dot{\Omega} \simeq \frac{F_p \sin \alpha \, (\cos \theta_2 - \cos \theta_1)}{n^2 \, m \, r_o} \tag{4.80}$$

where the sun is assumed to be in the equatorial plane at an angle α from the satellite ascending node, and

$$F_p = 4.74 \times 10^{-6} \, (1 + \eta) \, A \text{ newtons} \tag{4.81}$$
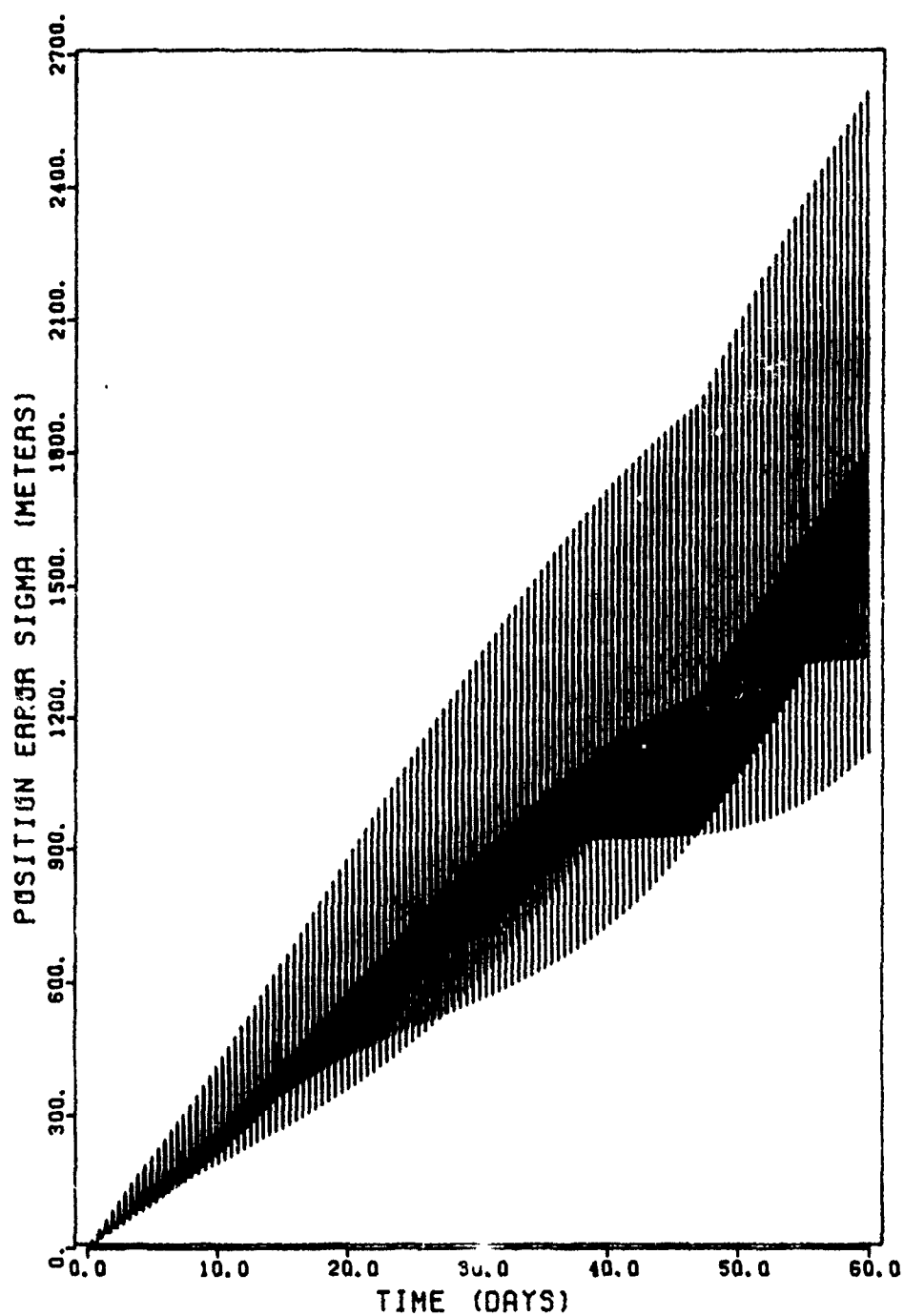
Figure 4.10. Predicted Position Error with Solar
Radiation Pressure Neglected.

for a satellite of mass m, cross-sectional area A, reflectivity η and radius r_o that enters eclipse at θ_1 and exists at θ_2.

This motion only occurs when vehicles are eclipsed by the earth, so the onboard model must include eclipse computations. The fairly large in-plane error caused by neglecting solar radiation pressure is more significant than a similar sized geopotential effect, because solar parameters are highly variable, whereas geopotential terms may be regarded as constant. It is this variability that requires the solar reflectivity to be estimated by the onboard filter.

4.6.3 N-Body Effects

The acceleration of a satellite near the earth due to the presence of a third body is given by Geyling and Westerman [1971, p. 113] as

$$\bar{a}^p = \frac{-\mu_p}{r_p^3} \left[\bar{r} - \frac{3\bar{r}_p(\bar{r} \cdot \bar{r}_p)}{r_p^2} \right] \qquad (4.82)$$

where μ_p and r_p refer to the perturbing body, and r refers to the satellite with motion referenced to the earth. When transformed to orbital elements and averaged over one satellite orbit, the results show a periodic effect in orbit inclination and a secular change in the ascending node of

$$\Delta\Omega_{ave} = -\frac{3\mu_p r^3}{2\mu_e r_p^3} \pi \cos i_o \quad \text{rad/orbit} \qquad (4.83)$$

For GPS orbits, these rates due to the sun and moon are

$$\Delta\Omega_{sun} = -5 \times 10^{-6} \text{ rad/orbit} \tag{4.84}$$

$$\Delta\Omega_{moon} = -1 \times 10^{-5} \text{ rad/orbit} \tag{4.85}$$

and after only one month (60 orbits), the cross-track position error at the node is 24 km.

Note that $\Delta\Omega_{ave}$, to first order, depends only on orbit inclination and radius; thus, each GPS satellite will experience the same effect, i.e., the whole constellation will precess and the results will not be observable from satellite-to-satellite tracking. Therefore, lunar and solar gravity must be modeled in the onboard propagation software. As for the planets, their effects are at least 4 orders of magnitude below the sun's [Geyling and Westerman, 1971, p. 113]; thus, 6-month errors of less than 15 m would be seen.

4.7 Relative Navigation Accuracy

To predict the performance of a model when used in a relative navigation filter, the consider analysis program is run in a filter mode in which observations are assumed to be processed from each visible satellite every 60 minutes. Model errors include earth geopotential terms, as given in Table 3.3, and solar radiation pressure, as shown in Table 4.2. This table also shows the observation, satellite ephemeris and clock errors simulated.

When errors in model parameters, other satellite positions

and clock biases are considered and observations processed, the position error stays below 7 m for 60 days (Figure 4.11). However, as shown in Figure 4.12, when errors due to a clock drift of 10^{12} sec/sec are included, the error grows to 2.391 km. Estimating both bias and drift along with the vehicle state brings the maximum error down to 40.8 m as depicted in Figure 4.13.

4.8 Consider Analysis Summary

The model suggested for the GPS autonomous navigation algorithm includes lunar and solar gravity and the earth geopotential through J_2 and C,S 3/2 and requires that solar radiation pressure and each GPS vehicle clock bias and drift be estimated. Including these terms in the consider analysis, plus errors described in Tables 3.2 and 4.1 for relevant terms, gives an overall one-sigma accuracy of 40.8 meters over 60 days.
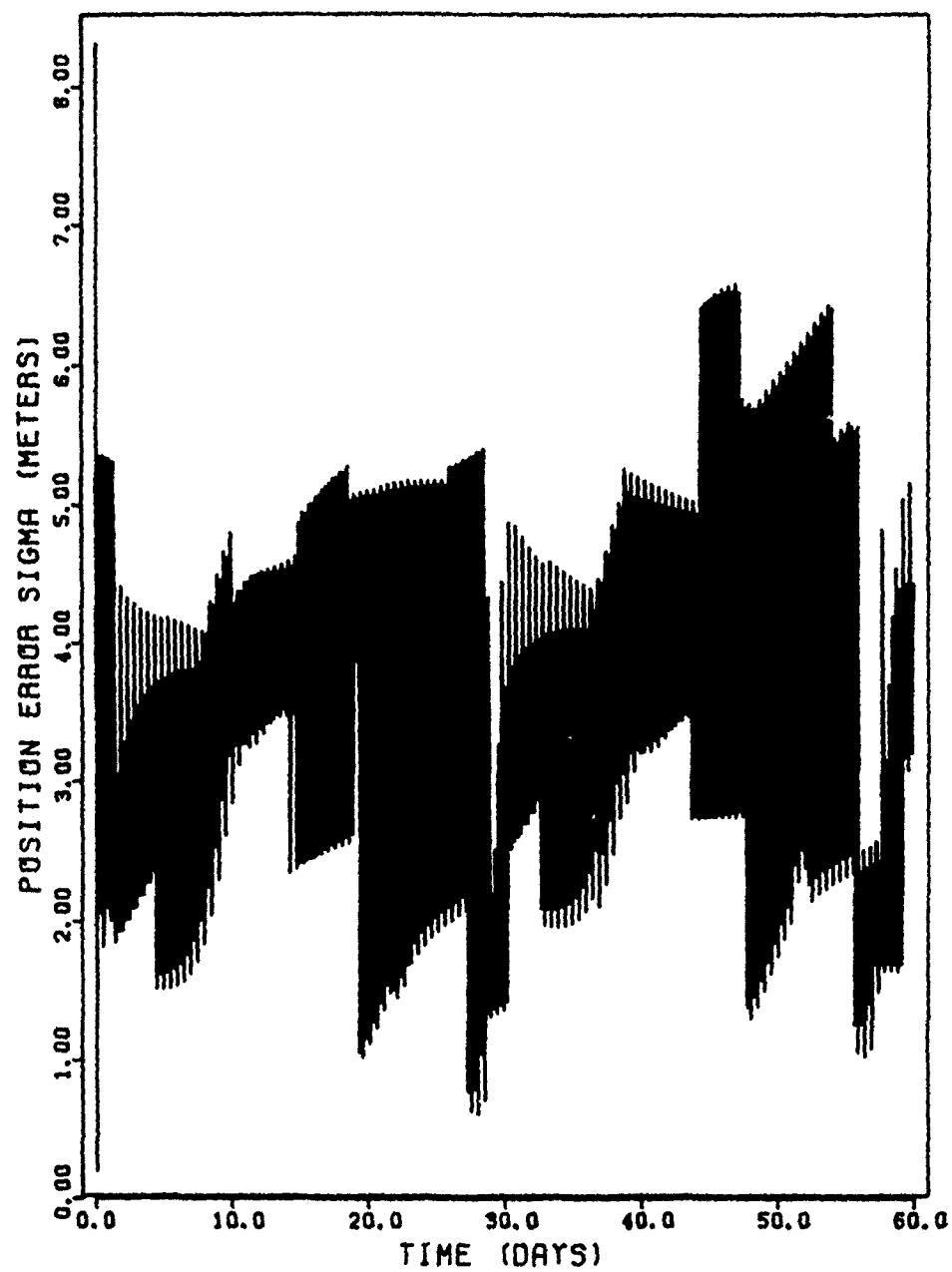
Figure 4.11. Estimated Position Error with Clock Bias Neglected
Using Range and Doppler Observations
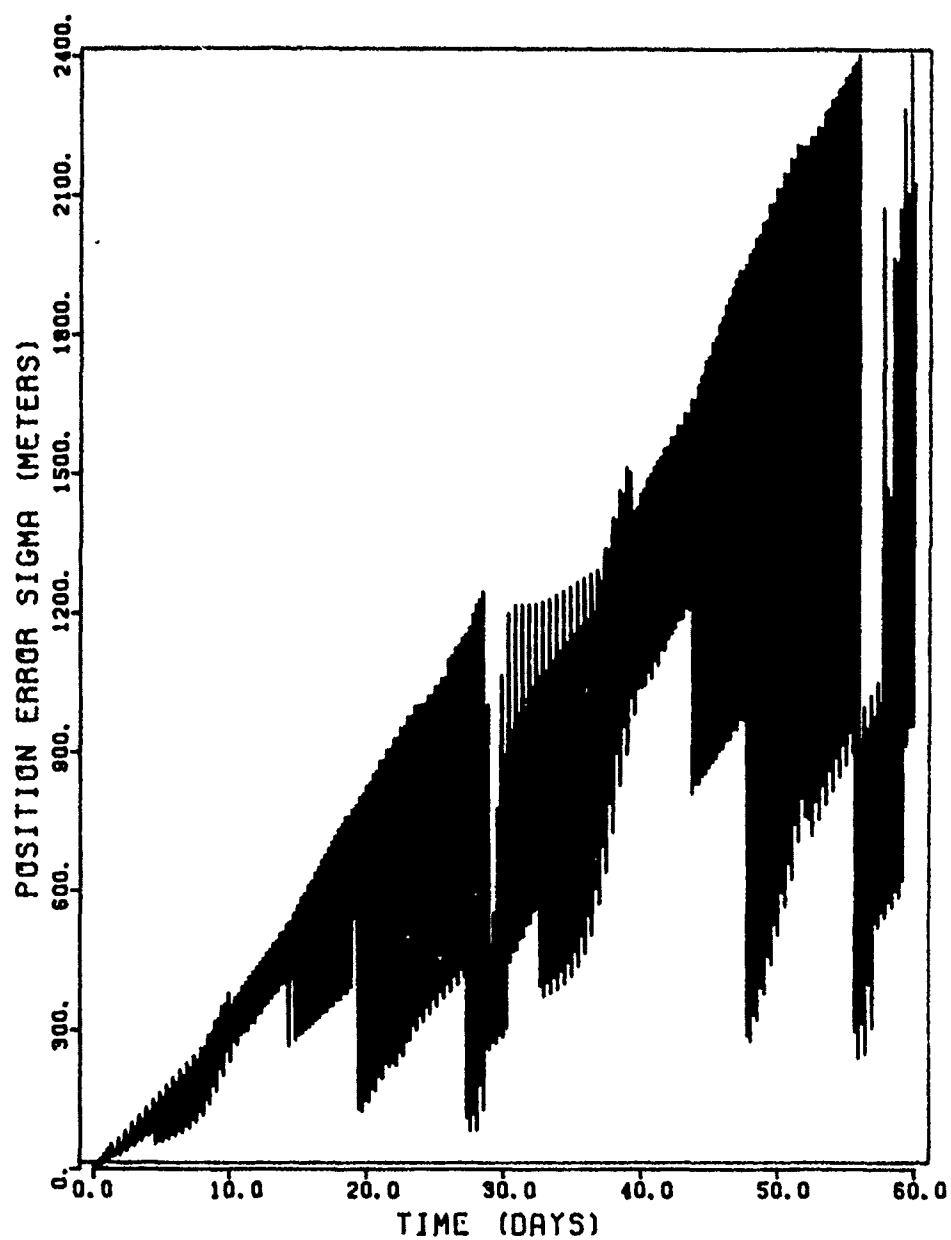
Figure 4.12.   Estimated Position Error with Clock Bias
and Drift Neglected Using Range and Doppler
Observations.
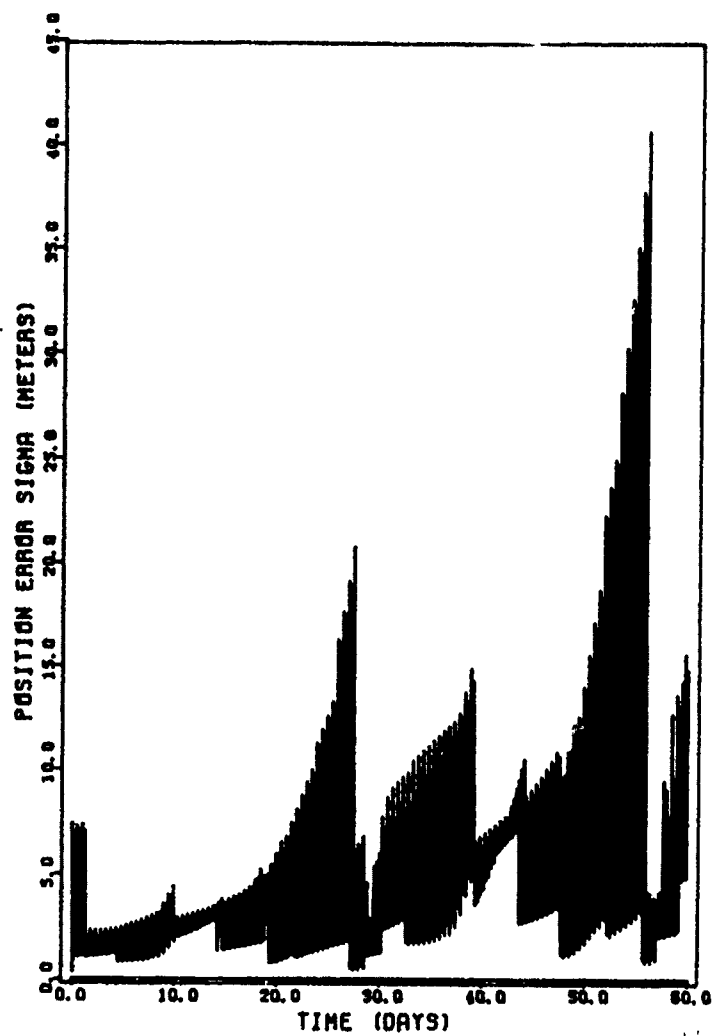
Figure 4.13. Estimated Position Error with Clock Bias and Drift
Estimated Using Range and Doppler Observations

CHAPTER 5

GPS NAVIGATION FILTER

5.1 <u>Introduction</u>

The onboard navigation filter that each GPS vehicle uses to determine its navigation state is a compromise between numerical accuracy, size, complexity and speed. Since current microprocessors do not have the word length or speed of mainframe processors, the filter must be designed to fit into a limited storage and time environment. As in the previous sections, it is assumed that each visible GPS satellite is tracked every 36 seconds and that the pseudo-range and integrated doppler observations are smoothed by a local curve-fitting procedure to produce one pair of observations per satellite each 60 minutes. A sequential filter then processes up to 14 pairs of range and doppler measurements and updates the navigation state each hour.

An alternate approach to the sequential filter is to collect smoothed observations for several hours and process them via a batch algorithm at the end of the observation span. This requires the covariance matrix and state to be propagated over much longer intervals, however, and would require more accuracy and sophistication in the dynamic model. This approach is worthy of study, but this analysis assumes a form of the extended Kalman sequential filter (EKF) to minimize propagation intervals. Other

studies have been performed on satellite navigation algorithms, e.g., Tapley, et. al. [1981], and square root formulations of the EKF have proven stable, efficient and accurate for autonomous navigation using GPS signals. The results of Tapley, et al., are directly applicable to the GPS autonomous navigation problem since they studied estimation algorithms, dynamic models and numerical integrators for onboard navigation of LANDSAT-D-type satellites. The main differences are that GPS is higher (semi-major axis - 26575 km vs. 7087 km) and that the onboard filter is actually a local filter solving a part of a global problem. The local filter aspect is addressed in Section 5.3.

5.2 Filter Model

The dynamic model selected for the GPS navigation filter algorithm differs from the LANDSAT-D model in that the higher altitude puts the satellite out of the atmospheric drag regime and into the area where solar radiation pressure and luni-solar gravity terms become significant. As noted in Section 4.6.3, lunar and solar gravity effects are unobservable in satellite-to-satellite tracking if the satellites are in the same orbits, and accurate models for these effects must be included in the dynamic model. Fortunately, lunar and solar ephemerides can be predicted accurately, and their masses are known to high enough accuracy that their gravitational effects can be modeled instead of estimated in

the filter.

Solar radiation pressure, however, is not as well modeled, and the satellite coefficient of reflectivity, η , and its rate, $\dot{\eta}$, must be estimated along with the satellite position, velocity, clock bias and drift, as discussed in Chapter 4.

The state vector for GPS #1 is then

$$X = \begin{bmatrix} \overline{r} \\ \overline{v} \\ C\Delta t_o \\ C\Delta f/f \\ \eta \\ \dot{\eta} \end{bmatrix} = \begin{bmatrix} x_1 \\ x_2 \\ x_3 \\ x_4 \\ x_5 \\ x_6 \\ x_7 \\ x_8 \\ x_9 \\ x_{10} \end{bmatrix} \tag{5.1}$$

5.2.1 Dynamic Equations

The dynamic model used to propagate the state by the nonlinear vector differential equation

$$\dot{X}(t) = F(X(t),t)$$

is

$$F(X(t),t) = \begin{bmatrix} \overline{v} \\ \overline{a}_e + \overline{a}_s + \overline{P}_s + \overline{P}_m + \overline{\epsilon}_a \\ C\Delta f/f \\ \epsilon_c \\ \dot{\eta} \\ 0 \end{bmatrix} \tag{5.2}$$

where

$\overline{a}_e$ = gravitational acceleration of the earth

$\overline{a}_s$ = acceleration due to solar radiation

$\overline{P}_s$ = perturbing acceleration due to the sun

$\overline{P}_m$ = perturbing acceleration due to the moon

and the stochastic forcing noises have the following statistics

$$E\left[\epsilon(t)\right]_\ell = 0 \tag{5.3}$$

$$E\left[\epsilon(t)\epsilon^T(\tau)\right]_\ell = q_\ell \delta(t-\tau) \tag{5.4}$$

where ℓ denotes the 3×1 vector acceleration process noise, $\overline{\epsilon}_a$, or the scalar clock frequency drift noise, ϵ_c.

The nonlinear state differential equations are linearized about a nominal state vector to produce

$$\dot{x}(t) = A(t)\, x(t) \tag{5.5}$$

where

$$A(t) = \frac{\partial F(X(t),t)}{\partial X(t)}\bigg|_{X(t)=X^*(t)} \tag{5.6}$$

$$= \begin{bmatrix}
\frac{\partial \bar{v}}{\partial \bar{r}} & \frac{\partial \bar{v}}{\partial \bar{v}} & \frac{\partial \bar{v}}{\partial cs} & \frac{\partial \bar{v}}{\partial \eta} & \frac{\partial \bar{v}}{\partial \dot{\eta}} \\[2mm]
\frac{\partial \bar{a}}{\partial \bar{r}} & \frac{\partial \bar{a}}{\partial \bar{v}} & \frac{\partial \bar{a}}{\partial cs} & \frac{\partial \bar{a}}{\partial \eta} & \frac{\partial \bar{a}}{\partial \dot{\eta}} \\[2mm]
\frac{\partial cr}{\partial \bar{r}} & \frac{\partial cr}{\partial \bar{v}} & \frac{\partial cr}{\partial cs} & \frac{\partial cr}{\partial \eta} & \frac{\partial cr}{\partial \dot{\eta}} \\[2mm]
\frac{\partial ce}{\partial \bar{r}} & \frac{\partial ce}{\partial \bar{v}} & \frac{\partial ce}{\partial} & \frac{\partial ce}{\partial \eta} & \frac{\partial ce}{\partial \dot{\eta}} \\[2mm]
\frac{\partial \dot{\eta}}{\partial \bar{r}} & \frac{\partial \dot{\eta}}{\partial \bar{v}} & \frac{\partial \dot{\eta}}{\partial cs} & \frac{\partial \dot{\eta}}{\partial \eta} & \frac{\partial \dot{\eta}}{\partial \dot{\eta}} \\[2mm]
0 & 0 & 0 & 0 & 0
\end{bmatrix}$$

where cr is the clock rate, ce is the clock error and cs is the clock state. For this application,

$$A(t) = \begin{bmatrix}
0(3\times3) & I(3\times3) & 0(3\times2) & 0(3\times1) & 0(3\times1) \\[2mm]
A_{21}(3\times3) & 0(3\times3) & 0(3\times2) & A_{24}(3\times1) & 0(3\times1) \\[2mm]
0(1\times3) & 0(1\times3) & A_{33}(1\times2) & 0 & 0 \\[2mm]
0(3\times3) & 0(3\times3) & 0(3\times2) & 0(3\times1) &
\end{bmatrix}$$

The entries of A are described in the following sections.

5.2.2 Geopotential Model

As discussed in Section 4.6.1, earth geopotential terms, with the exception of J_2 and C,S 3/2 cause along-track secular and periodic perturbations that are small during the one-hour

propagation interval and are observable in satellite-to-satellite tracking. The effects of J_2 are large and include both tangential and normal excursions and are thus unobservable to the navigation system. They must be included in the dynamic model, which becomes

$$\overline{a}_e = \begin{bmatrix} -\mu \, x_1/r^3 \, (1 + \alpha) \\ -\mu \, x_2/r^3 \, (1 + \alpha) \\ -\mu \, x_3/r^3 \, (1 + \beta) \end{bmatrix} \tag{5.7}$$

where

$$r = \sqrt{x_1^2 + x_2^2 + x_3^2} \tag{5.8}$$

$$\alpha = 1.5 \, J_2 \, \frac{R_e^2}{r^2} \, (1 - 5 \, x_3^2/r^2) \tag{5.9}$$

$$\beta = 1.5 \, J_2 \, \frac{R_e^2}{r^2} \, (3 - 5 \, x_3^2/r^2) \tag{5.10}$$

$$J_2 = .001083 \tag{5.11}$$

For the dynamic model given above,

$$A_{21_e} = \begin{bmatrix} a_{11_e} & a_{12_e} & a_{13_e} \\ a_{12_e} & a_{22_e} & a_{23_e} \\ a_{13_e} & a_{23_e} & a_{33_e} \end{bmatrix} \tag{5.12}$$

where

$$a_{11_e} = \frac{-\mu}{r^3}\left(1 - 3x_1^2/r^2\right)\left(1 + \alpha\right) + \frac{3J_2R_e^2}{r^7}\, x_1^2\left(1 - 10x_3^2/r^2\right) \quad (5.13)$$

$$a_{12_e} = \left(3\mu x_1 x_2/r^5\right)\left(1 + \alpha\right) + \frac{3J_2R_e^2}{r^7}\, x_1 x_2\left(1 - 10x_3^2/r^2\right) \quad (5.14)$$

$$a_{13_e} = \left(3\mu x_1 x_3/r^5\right)\left(1 + \alpha\right) + \frac{3J_2R_e^2}{r^7}\, x_1 x_3\left(6 - 10x_3^2/r^2\right) \quad (5.15)$$

$$a_{22_e} = \frac{\mu}{r^3}\left(1 - 3x_2^2/r^2\right)\left(1 + \alpha\right) + \frac{3J_2R_e^2}{r^7}\, x_2^2\left(1 - 10x_3^2/r^2\right) \quad (5.16)$$

$$a_{23_e} = \left(3\mu x_2 x_3/r^5\right)\left(1 + \alpha\right) + \frac{3J_2R_e^2}{r^7}\, x_2 x_3\left(6 - 10x_3^2/r^2\right) \quad (5.17)$$

$$a_{33_e} = \frac{-\mu}{r^3}\left(1 - 3x_3^2/r^2\right)\left(1 + \beta\right) + \frac{3J_2R_e^2}{r^7}\, x_3^2\left(8 - 10x_3^2/r^2\right) \quad (5.18)$$

The acceleration due to C,S 3/2 is computed by rotating the satellite position vector to the ECR coordinate, computing satellite latitude (ϕ) and longitude (λ), and taking the gradient of the 3/2 geopential term:

$$U_{32} = \frac{\mu}{r}\left(\frac{R_e}{r}\right)^3 P_{32}(\sin\phi)$$

$$\left[C_{32}\cos 2\lambda + S_{32}\sin 2\lambda\right] \quad (5.19)$$

where C_{32} and S_{32} are the spherical harmonic coefficients and $P_{32}(\sin\phi)$ is the Legendre Associated Function of degree 3 and order 2 for the argument $\sin\phi$. P_{lm} can be computed recursively

from the equation

$$P_{\ell m}(\sin \phi) = P_{\ell-2,m} + (2\ell-1) \cos \phi \, P_{\ell-1,m-1} \tag{5.20}$$

where $P_{\ell m} = 0$ if $m > \ell$. Thus, $P_{32}(\sin \phi)$ is obtained from

$$P_{32}(\sin\phi) = 0 + 5 \cos \phi \, P_{22} \tag{5.21}$$

$$P_{22}(\sin\phi) = 3 \cos \phi \, P_{11} \tag{5.22}$$

where

$$P_{11}(\sin\phi) = \cos \phi \, . \tag{5.23}$$

Thus,

$$P_{32}(\sin\phi) = 15 \cos^3 \phi \tag{5.24}$$

Entries of A_{21_e} for C,S 3/2 are not computed since the perturbation due to these terms are so much smaller than for J_2 and would thus affect the orbit over relatively long prediction times.

5.2.3 Solar Radiation Model

In this analysis, the same solar radiation model is used in the onboard filter as is employed in UTOPIA. The acceleration due to radiation pressure is given by McMillan [1973] as

$$\bar{a}_s = p_s \, r_s^2 \, (1 + \eta) \, \frac{A}{m} \, \frac{\bar{r}_{vs}}{r_{vs}^3} \, \gamma \tag{5.25}$$

where

p_s = solar radiation pressure on a black body

r_s = sun's distance from earth

η = satellite surface reflectivity

A = satellite effective area

m = satellite mass

$\overline{r}_{vs}$ = sun-satellite radius vector = $\overline{r} - \overline{r}_s$

γ = shadow indicator

For a spherical earth and cylindrical shadow,

$$\gamma = 0 \quad \text{if} \quad \overline{r} \cdot \frac{\overline{r}_s}{r} < 0 \quad \text{and} \quad (r^2 - r_e^2)^{1/2} < r_e \tag{5.26}$$

$$\gamma = 1 \quad \text{otherwise} \tag{5.27}$$

The partial derivative matrix is

$$A_{21_s} = \begin{bmatrix} a_{11_s} & a_{12_s} & a_{13_s} \\ a_{12_s} & a_{22_s} & a_{23_s} \\ a_{13_s} & a_{23_s} & a_{33_s} \end{bmatrix} \tag{5.28}$$

where

$$a_{11_s} = p_s r_s^2 (1+\eta) \frac{A\gamma}{m r_{vs}^3} \left[1 - 3\frac{(x-x_s)^2}{r_{vs}^2} \right] \tag{5.29}$$

$$a_{12_s} = -3 p_s r_s^2 (1+\eta) \frac{A\gamma}{m} \frac{(x-x_s)(y-y_s)}{r_{vs}^5} \tag{5.30}$$

$$a_{13_s} = -3p_s r_s^2 (1+n) \frac{A\gamma}{m} \frac{(x-x_s)(z-z_s)}{r_{vs}^5} \tag{5.31}$$

$$a_{22_s} = p_s r_s^2 (1+n) \frac{A\gamma}{mr_{vs}^3} \left[1 - 3\frac{(y-y_s)^2}{r_{vs}^2} \right] \tag{5.32}$$

$$a_{23_s} = -3p_s r_s^2 (1+n) \frac{A\gamma}{m} \frac{(y-y_s)(z-z_s)}{r_{vs}^5} \tag{5.33}$$

$$a_{33_s} = p_s r_s^2 (1+n) \frac{A\gamma}{mr_{vs}^3} \left[1 - 3\frac{(z-z_s)^2}{r_{vs}^2} \right] \tag{5.34}$$

A_{24_s} is then a vector given by

$$A_{24_s} = p_s rs \frac{A\overline{r}_{vs}}{mr_{vs}^3} \gamma \tag{5.35}$$

5.2.4 Lunar-Solar Gravity

The perturbations due to lunar and solar gravity are given by

$$P_s = -\mu_s \left[\frac{\overline{r}_s}{r_s^3} + \frac{\overline{\Delta}}{\Delta^3} \right] \tag{5.36}$$

where

$\overline{r}_s$ = vector from earth to sun

$\overline{\Delta} = \overline{r} - \overline{r}_s$

$$\mu_s = GM_s$$

and

$$\bar{F}_m = -\mu_m \left[\frac{\bar{r}_m}{r_m^3} + \frac{\bar{\Delta}}{\Delta^3} \right] \tag{5.37}$$

where

$\bar{r}_m$ = vector from earth to moon

$\bar{\Delta} = \bar{r} - \bar{r}_m$

$\mu_m = GM_m$

The vectors $\bar{r}_s$ and $\bar{r}_m$ are computed by assuming Keplerian orbits for the earth and moon and solving Kepler's equation for each time point. The partial derivatives of $\bar{F}_s$ and $\bar{P}_m$ can Then be obtained by a straightforward differentiation of Eqs. (5.35) and (5.36).

5.3 Decentralized Filtering

The problem of estimating the state vector of each of 18 GPS satellites from satellite-to-satellite pseudo-range and doppler information is a global estimation problem, since the measurement errors are a function of other satellite position errors as well as ranging system errors. To solve this problem on a global scale would require a "supervisor" system with knowledge of all spacecraft and measurement errors. If, at the other extreme, the situation is

handled by 18 decentralized processors, each solving the local estimation problem with no cognizance of the other spacecraft errors, an unstable solution results. Any GPS position error outside the range expected by the a priori measurement covariance, R , would quickly lead to filter divergence in the other processors.

This situation is similar to that faced by the Joint Tactical Information Dissemination System (JTIDS) in its aircraft relative navigation mode as described by Kerr and Chin [1980]. Since the two problems are alike in that each vehicle's state is independent of the others but measurements involve information exchange among the members, it is possible to cast GPS autonomous navigation as a relative navigation problem and apply known techniques of decentralized filtering.

Applying the methods described by Kerr and Chin to the GPS problem, the system state error is described by a linear differential equation of dimension 18 $n_i \times 1$, where n_i is the dimension of each spacecraft state

$$\dot{\underline{x}}(t) = F(t)\, \underline{x}(t) + \underline{w}(t). \tag{5.38}$$

This system can be expressed as the collection $\left\{ S_i , \ i=1, 2,\ldots,18 \right\}$ of separate dynamic systems:

$$S_i : \dot{x}_i(t) = F_i(t)\, x_i(t) + w_i(t) \tag{5.39}$$

having interconnected discrete measurements available to the ith

satellite:

$$y_i(t_k) = H(t_k)\underline{x}(t_k) + v_i(t_k)$$

$$= \left[\hat{\tilde{H}}_i(t_k) \mid \hat{H}_i(t_k)\right] \begin{bmatrix} M_i(t_k) \\ L_i(t_k) \end{bmatrix} \underline{x}(t_k) + v_i(t_k) \qquad (5.40)$$

where $M_i(t_k)$ is the projection operator from R^n to R^{n_i}, i.e.

$$x_i(t_k) = M_i(t_k)\,\underline{x}(t_k) \qquad\qquad\qquad (5.41)$$

and $L_i(t_k)$ selects those components of $\underline{X}(t_k)$ that appear in $\partial G(X(t_k,t_k)/\partial x_i(t_k)$. Thus

$$y_i(t_k) = \tilde{H}(t_k)x_i(t_k) + \hat{H}_i(t_k)L_i(t_k)\underline{x}(t_k) + v_i(t_k) \qquad (5.42)$$

and $L_i(t_k)\underline{x}(t_k)$ contains no component of $x_i(t_k)$ directly.

It is assumed that $w_i(t)$ and $v_i(t_k)$ are zero-mean white noise processes that are uncorrelated with $w_j(t)$, $v_j(t)$ and $x_j(0)$ for $j \neq i$.

Looking at the specific example of GPS-GPS pseudo-range, assume that vehicle i is tracking vehicles 1-3 at $t = t_k$. The measurement matrix, H_i for a satellite state vector of dimension 10, containing $\bar{r}$, $\bar{v}$, clock bias, clock drift, reflectivity and its rate is

$$H_i = \begin{bmatrix} \dfrac{x_{1_i} - x_{1_1}}{\rho_1} & \dfrac{x_{2_i} - x_{2_1}}{\rho_1} & \dfrac{x_{3_i} - x_{3_1}}{\rho_1} & 0 & 0 & 0 & 1 & 0 & 0 & 0 \\[2ex] \dfrac{x_{1_i} - x_{1_2}}{\rho_2} & \dfrac{x_{2_i} - x_{2_2}}{\rho_2} & \dfrac{x_{3_i} - x_{3_2}}{\rho_2} & 0 & 0 & 0 & 1 & 0 & 0 & 0 \\[2ex] \dfrac{x_{1_i} - x_{1_3}}{\rho_3} & \dfrac{x_{2_i} - x_{2_3}}{\rho_3} & \dfrac{x_{3_i} - x_{3_3}}{\rho_3} & 0 & 0 & 0 & 1 & 0 & 0 & 0 \end{bmatrix} \quad (5.43)$$

for

$$X_i = \begin{bmatrix} \bar{r} & \bar{v} & c\Delta t_o & \dfrac{c\Delta f}{f_o} & \eta & \dot{\eta} \end{bmatrix}^T \quad (5.44)$$

5.3.1 Decentralized Filter Algorithms

As discussed by Kerr and Chin, the Surely Locally Unbiased (SLU) [Sanders, et al., 1973] and the Sequentially Partitioned Algorithm (SPA) devised by Shah [1971] are stable solutions to the relative navigation problem. While the SLU filter is unbiased, it requires that the rank of $\hat{H}$ be less than the row dimension. This is not satisfied for the pseudo-range observation (and for integrated doppler), thus the SLU algorithm is not applicable.

According to Kerr and Chin, the SPA filter has been shown to be asymptotically stable, but it is not analytically unbiased. They state, however, that this potential problem can be handled adequately and recommend the SPA as the algorithm for JTIDS navigation processors. Biased solutions are, however, a potential problem area in GPS navigation and must be investigated.

5.3.2 Derivation of the Sequentially Partitioned Algorithm

Following Kerr and Chin [1981] with appropriate modifications for GPS, define the local system

$$x_i(k+1) = \phi_i(k+1,k)x_i(k) + w_i(k) \tag{5.45}$$

with observations

$$
\begin{aligned}
y_i(k) &= H(k)\underline{x}(k) + v_i(k) \\
&= \tilde{H}_i(k)x_i(k) + \hat{H}_i(k)\sum_{\substack{j=1 \\ j \neq i}}^{18} L_{ij}(k)x_j(k) + v_i(k).
\end{aligned}
\tag{5.46}
$$

where

$\underline{x}(t_k)$ = $p \cdot n_i \times 1$ vector for p satellites with n_i states each

$x_i(t_k)$ = $n_i \times 1$ state vector for satellite i

L_{ij} = $m \times n_j$ submatrix relating m observations from satellite j to satellite i

$$H(k) = \frac{\partial G(\underline{x}(t_k),t_k)}{\partial \underline{x}(t_k)} \tag{5.47}$$

$$\tilde{H}_i(k) = \frac{\partial G(\underline{x}(t_k),t_k)}{\partial x_i(t_k)} \tag{5.48}$$

$$\hat{H}_i(k) = \frac{\partial G(\underline{x}(t_k),t_k)}{\partial [\underline{x}(t_k)-x_i(t_k)]} \tag{5.49}$$

Now, define the state estimation errors

$$e_i(k|k) = x_i(k) - \hat{x}_i(k) \tag{5.50}$$

and

$$e_i(k|k-1) = x_i(k) - \bar{x}_i(k) \tag{5.51}$$

where

$$\hat{x}_i(k) = E[x_i(k)|y(k)] \tag{5.52}$$

and

$$\bar{x}_i(k) = \phi_i(t_k, t_{k+1}) \, \hat{x}_i(k-1). \tag{5.53}$$

Then

$$y_i(k) = \tilde{H}_i(k)x_i(k) + \hat{H}_i(k) \sum_{\substack{j=1 \\ j \neq 1}}^{18} L_{ij}(k)\bar{x}_j(k) + v_i^*(k) \tag{5.54}$$

where

$$v_i^*(k) = v_i(k) + \hat{H}_i(k) \sum_{\substack{j=1 \\ j \neq 1}}^{18} L_{ij}(k)e_j(k|k-1) \tag{5.55}$$

Now, assuming

1. $\bar{x}_j(k)$ is known for $j \neq i$, $j = 1, 2, \ldots, 18$

2. $e_j(k|k)$, $e_j(k|k-1)$ are Gaussian and white for $j = 1, 2, \ldots, 18$, $j \neq i$,

3. $v_i(k)$ is Gaussian white measurement noise

then the Kalman filter can be applied [Singh and Titli, 1978] to provide

$$R_i^*(k) \equiv E\left[v_i^*(k)v_i^{*T}(k)\right] \tag{5.56}$$

$$= R_i(k) + \hat{H}_i(k)\left[\sum_{\substack{j=1 \\ j\neq 1}}^{18} L_{ij}(k)\,\overline{P}_j(k)\,L_{ij}^T(k)\right]\hat{H}_i^T(k)$$

where

$$\overline{P}_j(k) = E\left[e_j(k|k-1)e_j^T(k|k-1)\right]. \tag{5.57}$$

The state error at t_{k+1} is updated by

$$\hat{x}_i(k+1) = \overline{x}_i(k+1) + \tilde{K}_i(k+1)\left[\,y_i(k+1) - \tilde{H}_i(k+1)\overline{x}_i(k+1)\right.$$

$$\left. - \hat{H}_i(k+1)\sum_{\substack{j=1 \\ j\neq 1}}^{18} L_{ij}(k+1)\overline{x}_j(k+1)\right] \tag{5.58}$$

where

$$\tilde{K}_i(k+1) = \overline{P}_i(k+1)\tilde{H}_i^T(k+1)\,[\tilde{H}_i(k+1)\overline{P}_i(k+1)\tilde{H}_i^T(k+1)$$

$$+ R_i^*(k+1)]^{-1} \tag{5.59}$$

and the state error covariance is updated by Joseph's form

$$P_i(k+1) = \left[I-\tilde{K}_i(k+1)\tilde{H}_i(k+1)\right]\overline{P}_i(k+1)\left[I-\tilde{K}_i(k+1)\tilde{H}_i(k+1)\right]^T$$

$$+ \tilde{K}(k+1)R_i^*\tilde{K}_i^T(k+1) \tag{5.60}$$

In the extended filter where the state correction is added to the state after each measurement update,

$$\hat{X}_i(k+1) = \overline{X}_i(k+1) + \hat{x}_i(k+1) \qquad (5.61)$$

where

$$\hat{x}_i(k+1) = K_i(k+1)y_i(k+1) . \qquad (5.62)$$

Comparing the SPA to consider covariance analysis, it is seen that, for no interconnection in the dynamic model, the SPA is a consider filter in which errors in GPS vehicles' positions and clocks are considered.

5.3.3 Sequential Processing of Pseudo-Range Observations

For the case of GPS i obtaining pseudo-range observations from one satellite (j) at a time in a sequential receiver, assuming

$$X_i^T = \left[\overline{r} \ \overline{v} \ \Delta t_i \ \frac{\Delta f_i}{f} \ n_i \dot{n}_i \right]$$

$$H_i(k) = \left[\frac{-(x_{1_j}-x_{1_i})}{\rho} \ \frac{-(x_{2_j}-x_{2_i})}{\rho} \ \frac{-(x_{3_j}-x_{3_i})}{\rho} \ 0 \ 0 \ 0 \ -1 \ 0 \ 0 \ 0 \ldots \right.$$

$$\left. \ldots 0 \ 0 \ldots \frac{(x_{1_j}-x_{1_i})}{\rho} \ \frac{(x_{2_j}-x_{2_i})}{\rho} \ \frac{(x_{3_j}-x_{3_i})}{\rho} \ 0 \ 0 \ 0 \ -1 \ 0 \ 0 \ 0 \ldots \right]$$

$$(5.63)$$

with zeroes for all partials with respect to X_ℓ, $\ell \neq i$ or j. This vector is then separated into

$$\bar{H}_i(k) = \left[\frac{-(x_{1_j} - x_{1_i})}{\rho} \quad \frac{-(x_{2_j} - x_{2_i})}{\rho} \quad \frac{-(x_{3_j} - x_{3_i})}{\rho} \quad 0 \ 0 \ 0 \ -1 \ 0 \ 0 \ 0 \right]$$

$$= \left[\ \bar{h}_1 \quad \bar{h}^2 \quad \bar{h}_3 \ 0 \ 0 \ 0 \ \bar{h}_7 \ 0 \ 0 \ 0 \ \right] \tag{5.64}$$

and

$$\hat{H}_i(k) = \left[\ -\bar{h}_1 \quad -\bar{h}_2 \quad -\bar{h}_3 \ 0 \ 0 \ 0 \ -\bar{h}_7 \ 0 \ 0 \ 0 \ \right] \tag{5.65}$$

The L matrix for this situation is

$$L_{i\ell} = \left[\ 0 \ \right] \quad \text{for} \quad \ell \neq j \tag{5.66}$$

and

$$L_{ij} = \begin{bmatrix} 1 & & & & & & \\ & 1 & & & & & 0 \\ & & 1 & 0 & & & \\ & & & 0 & 0 & & \\ & & & & 0 & 1 & \\ & & & & & 0 & 0 \\ 0 & & & & & & 0 \end{bmatrix} \tag{5.67}$$

Now, define

$$\alpha = \hat{H}_i(k) \left| \sum_{\substack{\ell=1 \\ \ell \neq i}}^{N} L_{i\ell} \ \bar{P}_\ell \ L_{i\ell}^T \right| \hat{H}_i^T(k)$$

$$= [\bar{h}_1 \ \bar{h}_2 \ \bar{h}_3 \ 0 \ 0 \ 0 \ \bar{h}_7 \ 0 \ 0 \ 0] \ L_{ij} \bar{P}_j L_{ij}^T [\bar{h}_1 \ \bar{h}_2 \ \bar{h}_3 \ 0 \ 0 \ 0 \ \bar{h}_7 \ 0 \ 0 \ 0]^T$$

$$= \tilde{h}_1^2 \overline{P}_{11_j} + \tilde{h}_2^2 \overline{P}_{22_j} + \tilde{h}_3^2 \overline{P}_{33_j} + \tilde{h}_7^2 \overline{P}_{77_j}$$

$$+ 2 \left(\tilde{h}_1 \tilde{h}_2 \overline{P}_{12_j} + \tilde{h}_1 \tilde{h}_3 \overline{P}_{13_j} + \tilde{h}_2 \tilde{h}_3 \overline{P}_{23_j} \right.$$

$$\left. + \tilde{h}_1 \tilde{h}_7 \overline{\overline{P}}_{17_j} + \tilde{h}_2 \tilde{h}_7 \overline{P}_{27_j} + \tilde{h}_3 \tilde{h}_7 \overline{P}_{37_j} \right) \qquad (5.68)$$

then

$$R_i^*(k) = R_i(k+1) + \alpha \qquad (5.69)$$

5.3.4 Sequential Processing of Doppler Observations

When processing integrated doppler measurements in a sequentially partitioned algorithm, the measurement matrix is

$$
H_i(k) = \left[\frac{-(x_{1_j}-x_{1_i})}{\rho} \quad \frac{-(x_{2_j}-x_{2_i})}{\rho} \quad \frac{-(x_{3_j}-x_{3_i})}{\rho} \quad 0\ 0\ 0\ 0\ \tau\ 0\ 0\ldots \right.
$$

$$
\left. \frac{(x_{1_j}-x_{1_i})}{\rho} \quad \frac{(x_{2_j}-x_{2_i})}{\rho} \quad \frac{(x_{3_j}-x_{3_i})}{\rho} \quad 0\ 0\ 0\ 0\ -\tau\ 0\ 0\ldots 0\right]_{\tau_2}
$$

$$
- \left[\frac{-(x_{1_j}-x_{1_i})}{\rho} \quad \frac{-(x_{2_j}-x_{2_i})}{\rho} \quad \frac{-(x_{3_j}-x_{3_i})}{\rho} \quad 0\ 0\ 0\ 0\ \tau\ 0\ 0\ldots\right.
$$

$$
\left. \frac{(x_{1_j}-x_{1_i})}{\rho} \quad \frac{(x_{2_j}-x_{2_i})}{\rho} \quad \frac{(x_{3_j}-x_{3_i})}{\rho} \quad 0\ 0\ 0\ 0\ -\tau\ 0\ 0\ldots 0\right]_{\tau_1} \phi(\tau_1,\tau_2)
$$

$$(5.70)$$

where τ is the receiver time tag and $\tau_2 = t_k$. For the short time interval, $\tau_2 - \tau_1 = 1.5$ sec , thus

$$
\phi(\tau_1,\tau_2) \simeq I \tag{5.71}
$$

and

$$
H_i(k) \simeq [(\tilde{h}_1(\tau_2)-\tilde{h}_1(\tau_1))\ (\tilde{h}_2(\tau_2)-\tilde{h}_2(\tau_1)
$$

$$
(\tilde{h}_3(\tau_2)-\tilde{h}_3(\tau_1))\ 0\ 0\ 0\ 0\ \tilde{h}_8\ 0\ 0\ 0\ldots(\tilde{h}_1(\tau_1)-\tilde{h}_1(\tau_2))
$$

$$
(\tilde{h}_2(\tau_1)-\tilde{h}_2(\tau_2)(\tilde{h}_3(\tau_1)-\tilde{h}_3(\tau_2))\ 0\ 0\ 0\ 0\ -\tilde{h}_8\ 0\ 0\ldots] \tag{5.72}
$$

where

$$\tilde{h}_8 = \tau_2 - \tau_1 .\qquad(5.73)$$

As in the case with pseudo-range observations, this vector (for one observation) can be separated into

$$\tilde{H}_i(k) = [(\tilde{h}_1(\tau_2) - \tilde{h}_1(\tau_1))\ (\tilde{h}_2(\tau_2) - \tilde{h}_2(\tau_1))$$
$$(\tilde{h}_3(\tau_2) - \tilde{h}_3(\tau_1))\ 0\ 0\ 0\ 0\ \tilde{h}_8\ 0\ 0\ ]\qquad(5.74)$$

and

$$\hat{H}_i(k) = [-(\tilde{h}_1(\tau_2) - \tilde{h}_1(\tau_1)) - (\tilde{h}_2(\tau_2) - \tilde{h}_2(\tau_1))$$
$$-(\tilde{h}_3(\tau_2) - \tilde{h}_3(\tau_1))\ 0\ 0\ 0\ 0\ -\tilde{h}_8\ 0\ 0\ ]\qquad(5.75)$$

with

$$L_{i\ell} = [\ 0\ ]\quad \ell \neq j\qquad(5.76)$$

$$L_{ij} = \begin{bmatrix} 1 & & & & & & 0 \\ & 1 & & & & & \\ & & 1 & 0 & & & \\ & & & 0 & 0 & & \\ & & & & 0 & 1 & \\ & & & & & 0 & \\ 0 & & & & & & 1 & 0 & 0 \end{bmatrix}\qquad(5.77)$$

Now, define

$$\beta = \hat{H}_i(k) \left[\sum_{\substack{\ell=1 \\ \ell \neq i}}^{N} L_{i\ell} \overline{P}_\ell L_{i\ell}^T \right] \hat{H}_i^T(k)\qquad(5.78)$$

and

$$\Delta \tilde{h}_i = \tilde{h}_i(\tau_2) - \tilde{h}_i(\tau_1) \ . \tag{5.79}$$

Then

$$\tilde{\beta} = \Delta\tilde{h}_1^2 \overline{P}_{11_j} + \Delta\tilde{h}_2^2 \overline{P}_{22_j} + \Delta\tilde{h}_3^2 \overline{P}_{33_j} + \tilde{h}_8^2 \overline{P}_{88_j}$$

$$+ 2\left(\Delta\tilde{h}_1 \Delta\tilde{h}_2 \overline{P}_{12_j} + \Delta\tilde{h}_1 \Delta\tilde{h}_2 \overline{P}_{13_j} + \Delta\tilde{h}_2 \Delta\tilde{h}_3 \overline{P}_{23_j}\right.$$

$$\left. + \Delta\tilde{h}_1 \tilde{h}_8 \overline{P}_{18_j} + \Delta\tilde{h}_2 \tilde{h}_8 \overline{P}_{28_j} + \Delta\tilde{h}_3 \tilde{h}_8 \overline{P}_{38_j}\right) \tag{5.80}$$

and

$$R_i^*(k+1) = R_i(k+1) + \beta \ . \tag{5.81}$$

Note that the transmission of data from satellite j now requires

$$\overline{P}_j = \begin{bmatrix} \overline{P}_{11} & \overline{P}_{12} & \overline{P}_{13} & \overline{P}_{17} & \overline{P}_{18} \\ & \overline{P}_{22} & \overline{P}_{23} & \overline{P}_{27} & \overline{P}_{28} \\ & & \overline{P}_{33} & \overline{P}_{37} & \overline{P}_{38} \\ & & & \overline{P}_{77} & \overline{P}_{88} \end{bmatrix} \tag{5.82}$$

5.4 Numerical Results

The Sequentially Partitioned Algorithm was included in a computer program (GPSNAV) that solves for corrections to the state

vector defined by Eq. (5.1) for each of the 18 GPS spacecraft. The original program employed a U-D filter as described in Appendix B, however, numerical instability in the propagation of the P matrix on the Cyber computer led to the decision to use a standard EKF formulation with Joseph's form of covariance update and propagation via the state transition matrix.

Each spacecraft receives range and doppler from all other visible satellites each 60 minutes. It also receives the covariance information defined in Eq. (5.82) at the time of transmission from each of the other vehicles. Range and doppler information was generated from a UTOPIA model incorporating an 8×8 earth geopotential, solar and lunar gravity, solar radiation pressure and clock bias and drift errors using the force models discussed in Chapter 4 with parameter and initial state errors as given in Table 5.1.

TABLE 5.1
UTOPIA-GPSNAV COMPARISON

Model	UTOPIA	GPSNAV
Geopotential	Thru C,S 8/8	J_2; C,S 3/2
Solar Radiation	Eq. (5.25) conical shadow	Eq. (5.25) cylindrical shadow
Lunar-Solar Ephemeris	JPL DE-96	Two body
Model Error		
μ	--	0
J_2	--	3.4×10^{-2} %
C,S 3/2		3.4×10^{-7} %
Initial State Error		
$\bar{r}_o$	--	0
$\bar{v}_o$	--	0
$\sigma_{\bar{r}}$	--	10 m
$\sigma_{\bar{v}}$	--	.002 m/s
Initial State Values		
η	.22	.22
$\dot{\eta}$	0	0
σ_η	--	10^{-5}
$\sigma_{\dot{\eta}}$	--	0
$\sigma_{c\Delta t}$	--	3×10^{-5}
$\sigma_{c\Delta f/f}$	10^{-3}	3×10^{-6}

Range errors of $1\sigma = 2.0$ m and doppler errors of $1\sigma = .001$ m/s   were

added.

The model incorporated in the SPA filter is a reduced order geopotential consisting of J_2 and C and S 3/2 plus solar and lunar gravity and solar radiation pressure. The filter estimates all of the terms in Eq. (5.1) and has the capability to include model noise (Q matrix) terms for acceleration and clock errors.

The program was run in a perfect clock mode in which clock errors were neither added to the data nor estimated by the filter. The results for satellite #1 (Fig. 5.1) show that the corrections to $\bar{r}$ and the position variance stay below 5 m, while the observation residuals are on the order of 10-15 m and that the solution appears stable for the four-day run.

When clock errors are included in the data, however, the results in Figure 5.2 show unstable results after about 80 hours. This run includes no model noise for clock parameters. When a clock drift noise term of 10^{-12} m/s is included in the noise compensation matrix (Fig. 5.3), the solution is stable for approximately 17 days with corrections on the order of 5 m and observation residuals of 10 m being seen.

When a four-day filter-determined ephemeris is compared with the UTOPIA ephemeris, it is seen that the in-plane components agree to within 40 m (Figs. 5.4 and 5.5) with a small secular trend (2 m/day) apparent in the along-track direction. Out-of-plane errors, however, grow secularly at approximately 20 m/day. This
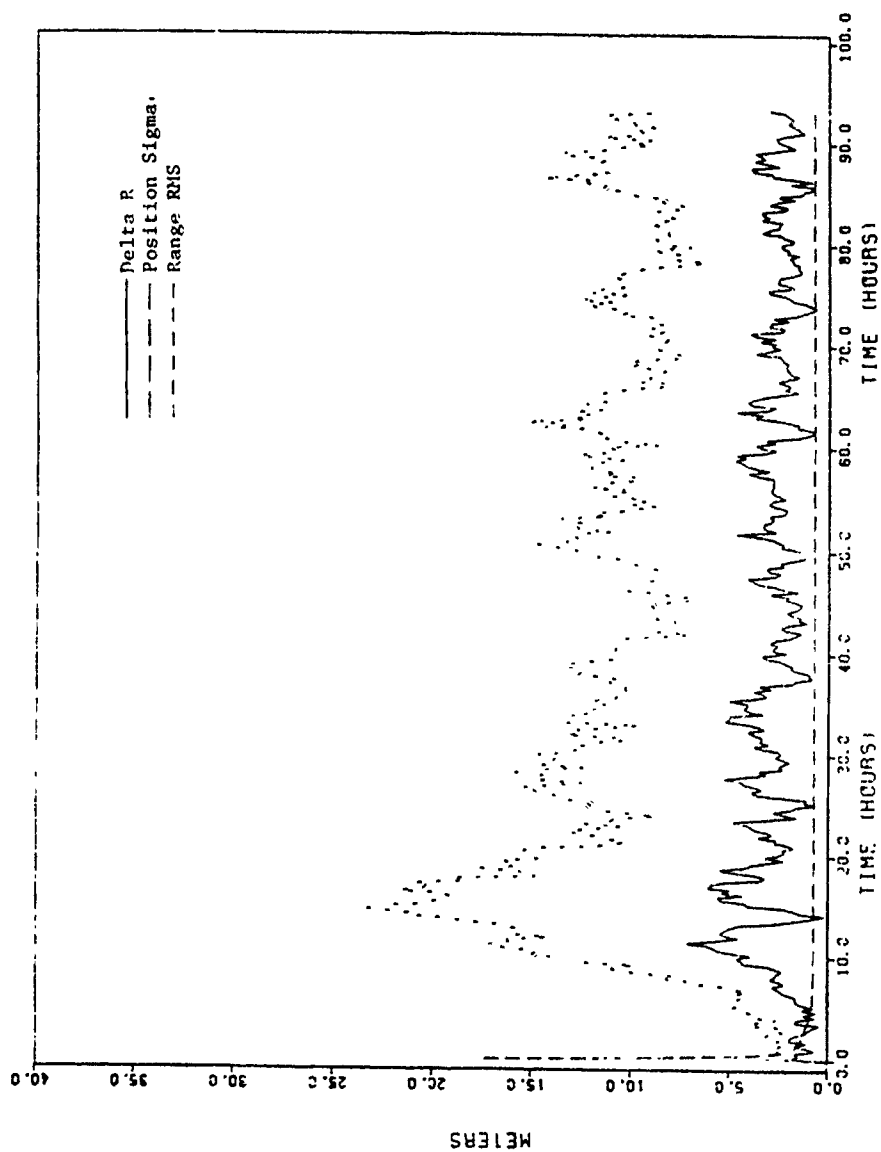
Figure 5.1. Estimator Run for Satellite No. 1; No Clock Errors
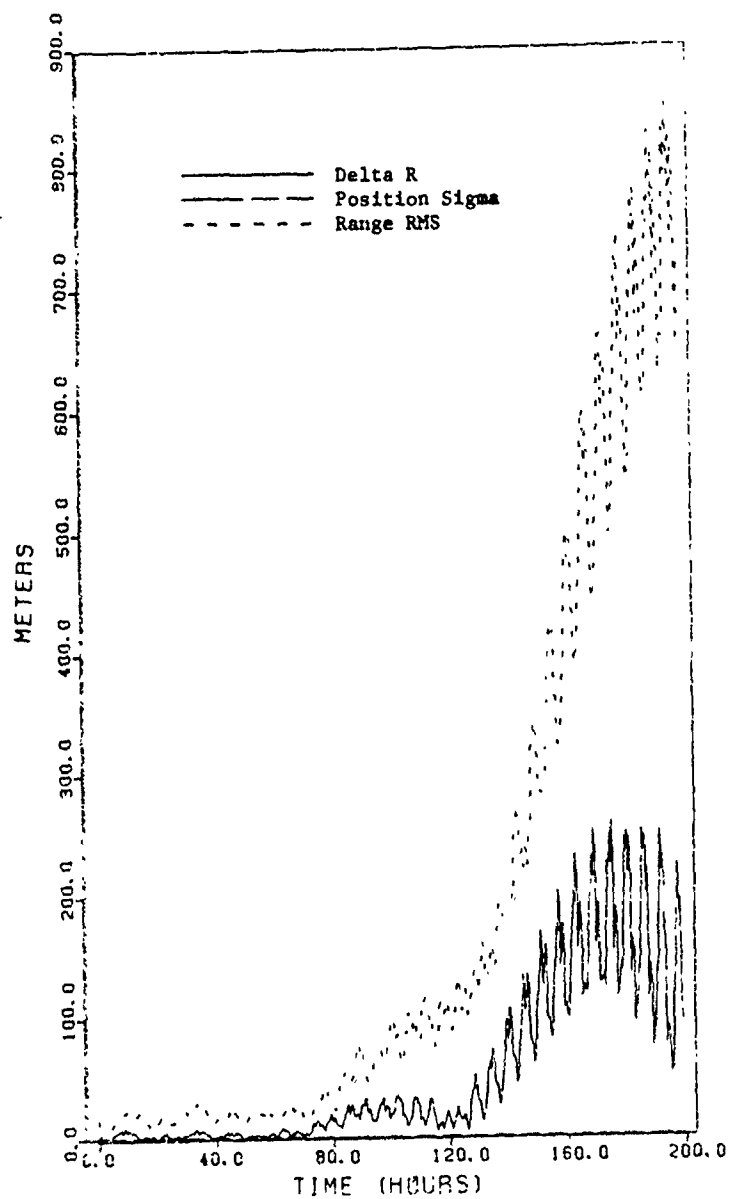
Figure 5.2. Estimator Run for Satellite No. 1
Clock Errors in Data
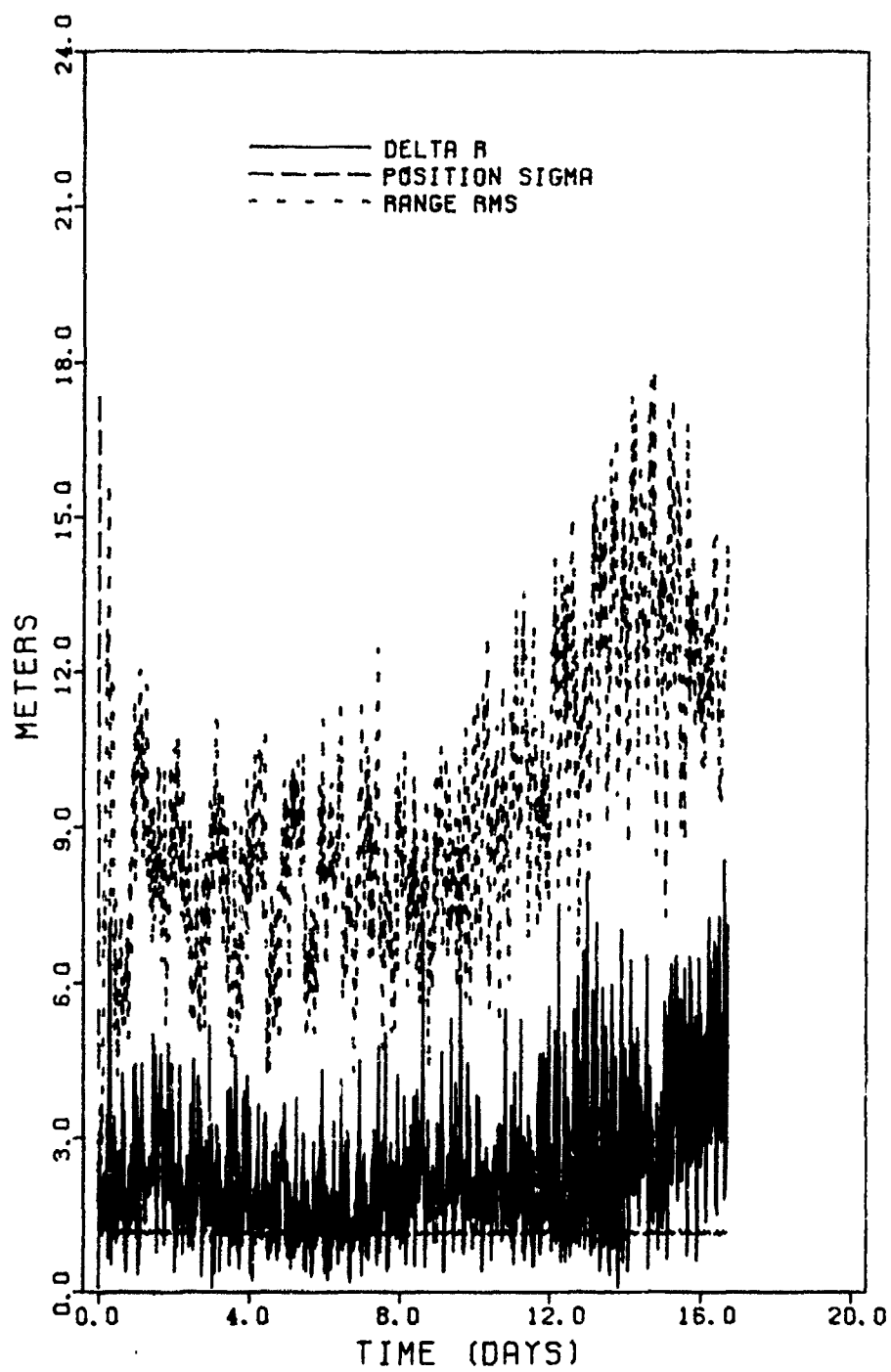
Figure 5.3. Estimator Run for Satellite No. 1; Clock Errors in Data and in Q Matrix
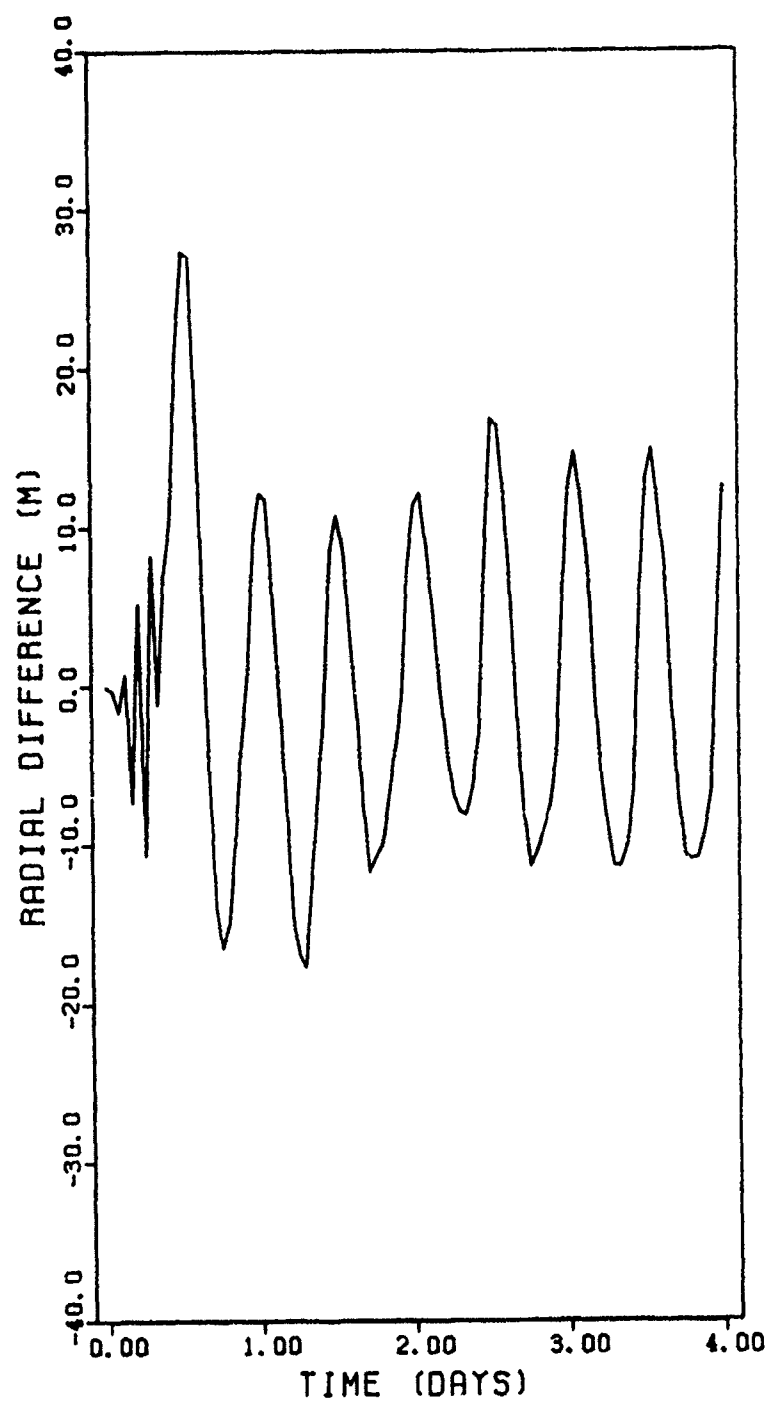
Figure 5.4. Radial Position Difference Between Estimator and UTOPIA
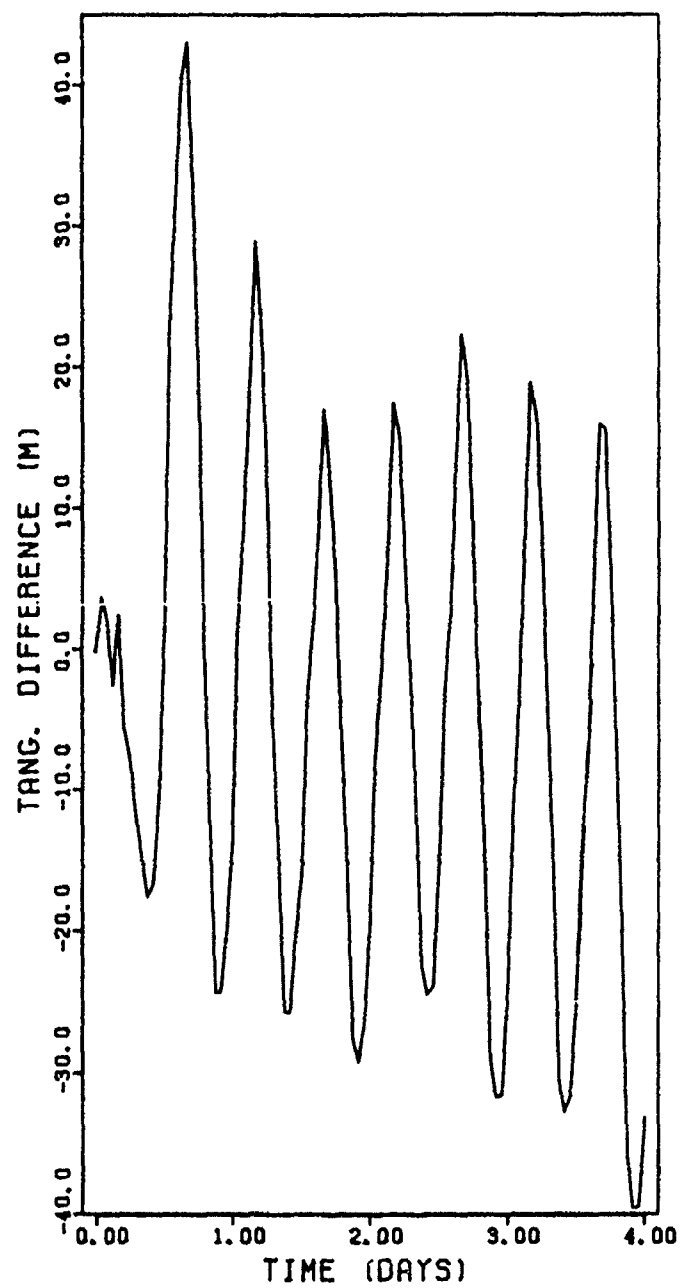
Figure 5.5. Tangential Position Difference Between
Estimator and UTOPIA

difference may be due to a combination of integrator/model differences between UTOPIA and errors, an inability of the filter to determine adequately the cross-track component of the vehicle's clock error, or biasing of the filter algorithm. When clock errors are removed from the data and the filters assume perfect clocks, the error growth is reduced to 11 m/day (Fig. 5.6), thus almost 50 percent of the error is due to the clocks. Since neither of the observable components (radial and tangential) show significant biases, this very limited test indicates that the problem discussed in Section 5.3.1 may not be significant.

If this secular trend continues, the total cross-track error would grow to 1.2 km after 60 days, but only a small percentage of the error would appear in the user-GPS line of sight. However, the importance of this error growth is not its magnitude but the fact that any onboard orbit determination scheme based upon satellite-to-satellite tracking will not observe similar planar motion. To solve this problem, either the model must be tuned to the specific application through much more extensive analysis and testing, or the navigation system must be augmented by a GPS transmitter in a different altitude orbit or on the surface of the earth or moon. A transmitter on the earth would solve this problem, plus it would allow the navigation algorithm to determine the earth-satellite orientation.
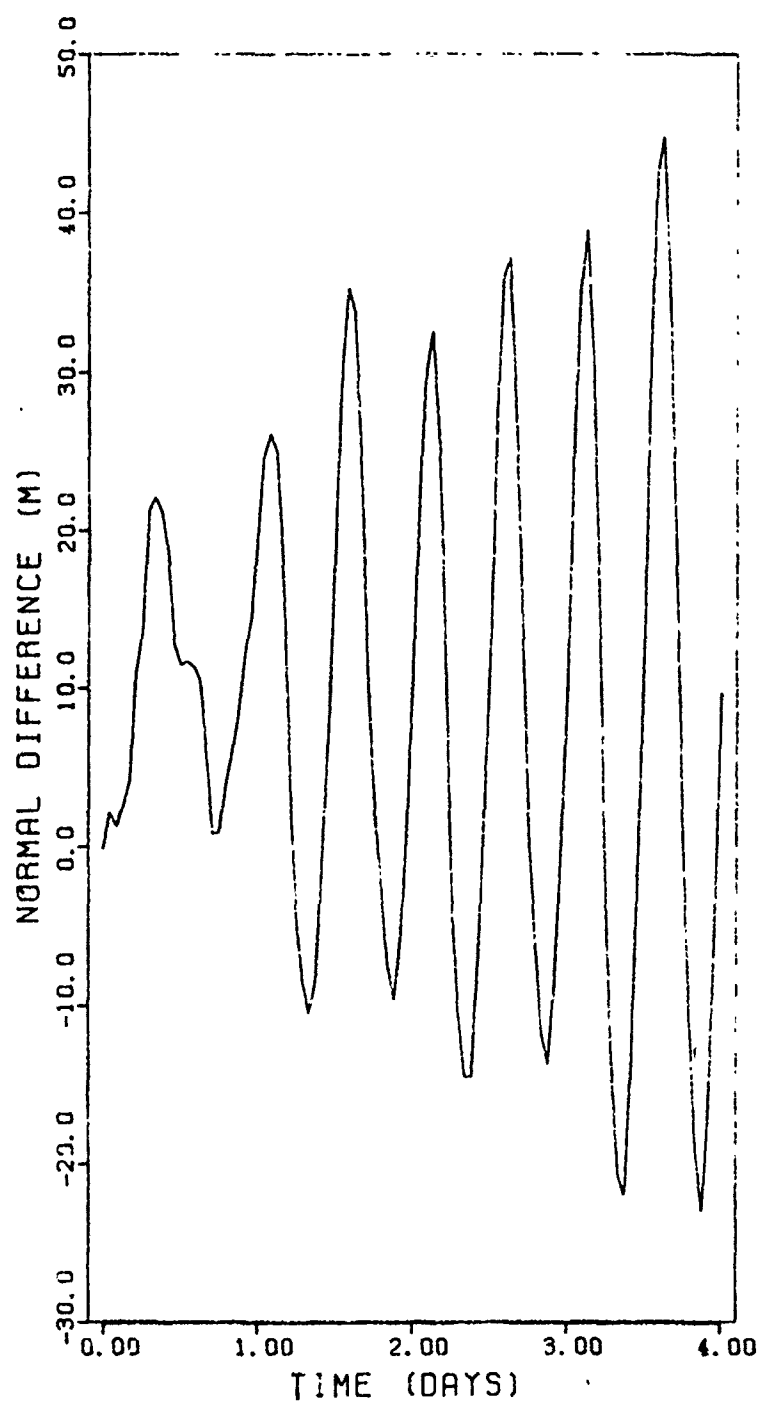
Figure 5.6.   Normal Position Difference Between Estimator
and UTOPIA; No Clock Errors in Data

CHAPTER 6

CONCLUSIONS AND RECOMMENDATIONS

6.1 Conclusions

The conclusions drawn from the discussion in the previous sections can be summarized as follows.

1. When compared with the space sextant, current design solid-state matrix star sensors coupled with current horizon sensors yield a factor of 16 worse navigation accuracy.

2. If matrix sensors can be used to measure the earth horizon by star refraction to a precision comparable to the star position measurement, they can provide better navigation accuracies than the space sextant. A critical factor in this scheme is the fact that, for a constant tangent height error, apparent horizon sensor error quickly drops to levels near or below the original actual sensor error as altitude increases. A key factor limiting refraction determination of earth horizon is the accuracy to which atmospheric density can be predicted.

3. Since matrix sensors can be derated to match less stringent program requirements, they can be used to provide angular information with a precision varying from >20 arcsec to <1 arcsec with corresponding navigation accuracy.

172

4. The space sextant has a greater ability to recover from loss of attitude control than do the fixed sensors.

5. Atmospheric refraction uncertainties contribute approximately 1500 m to the error in the determination of ray tangency altitude.

6. For navigation requirements of 50 m or less, the GPS receiver is recommended. It is possible that a SHAD and/or a matrix sensor may produce real accuracies of <50 m, but an analysis of all relevant error sources is required to verify this conjecture.

7. An onboard navigation system for GPS based upon satellite-to-satellite data transmission is feasible. However, this system is inherently unable to determine similar motion of all orbital planes and the earth. While earth angular position can be predicted to about 50 ms over six months, this error, in addition to planar motion, would cause errors normal to the satellite plane to reach approximately 1.3 km.

8. The Sequentially Partitioned Algorithm provides a stable solution for each satellite's state vector, including clock parameters, as long as model noise compensation is used. Preliminary results do not show a tendency toward biasing.

6.2 <u>Recommendations</u>

These recommendations are made following the previous study.

1. Development of the matrix sensor technology should be continued.

2. Investigation of the feasibility of performing improved horizon determination from star refraction measurements should parallel sensor development. Current and future refraction data should be used to improve atmospheric density modeling. This is critical to the success of navigation by matrix sensors.

3. Further refinements should be made in the analysis of the matrix sensor measurement to include all error sources affecting the measurement and its reduction to a navigation measurement.

4. Further studies of GPS cross-link navigation should be conducted to include:

   a. A more detailed evaluation of filter performance with respect to model and clock parameters.

   b. Evaluation of navigation performance when augmented by an additional transmitter in space, on earth and on the

moon.

c. The feasibility of including navigation information in the L_3 cross-link.

d. U-D filter performance when used with the SPA algorithm.

APPENDIX A

CONVERSION OF BATCH PARTIAL DERIVATIVES TO SEQUENTIAL

The University of Texas Orbit Processor (UTOPIA) produces precise estimates of position and velocity for spacecraft using several types of observations, including laser range and altimeter height. The basic batch and sequential algorithms are described by McMillan [1973] and Wilson [1976].

A relatively recent addition to UTOPIA is the capability of producing partials of the spacecraft state at observation times (inertial $\bar{r}(t_i)$ and $\bar{v}(t_i)$) with respect to the state and several model parameters at some user-defined epoch. These model parameters include $\mu_\oplus$, the spherical expansion coefficients (C_{lm}, S_{lm}), atmospheric drag, solar radiation pressure and unknown spacecraft accelerations in the RTN coordinate system. The purpose of the partials is to allow the program to interface with the JPL consider covariance analysis program COVAN to produce a consider covariance matrix at epoch (t_o) after processing simulated observations at t_i, $i=1,...,k$. UTOPIA does not simulate satellite-to-satellite range or doppler observations nor does it produce a sequential form of the ϕ and ψ matrices required for long-term sequential analysis of the GPS autonomous navigation problem.

It is possible, however, to convert the batch or epoch forms of these matrices to a sequential form by the following

176

algorithm:

A.1 Conversion from $\phi(t_{j+1}, t_o)$ to $\phi(t_{j+1}, t_j)$

Given the sequences $\phi(t_o, t_o)$, $\phi(t_1, t_o)$, $\phi(t_2, t_o)...\phi(t_{j+1}, t_o)$ and $\psi(t_o, t_o)$, $\psi(t_1, t_o)$, $\psi(t_2, t_o)...\psi(t_{j+1}, t_o)$, we desire the sequences $\phi(t_o, t_o)$, $\phi(t_1, t_o)$, $\phi(t_2, t_1)...\phi(t_{j+1}, t_j)$ and $\psi(t_o, t_o)$, $\psi(t_1, t_o)$, $\psi(t_2, t_1)...\psi(t_{j+1}, t_j)$. Suppose a state vector ξ is composed of variables X and parameters Z, then

$$\phi(t_i, t_j) = \left. \frac{\partial X(t_i)}{\partial X(t_j)} \right|_{\xi^*} \tag{A.1}$$

$$\psi(t_i, t_j) = \left. \frac{\partial X(t_i)}{\partial Z(t_j)} \right|_{\xi^*} \tag{A.2}$$

Note that

$$\phi(t_i, t_j) = \frac{\partial X(t_i)}{\partial X(t_o)} \frac{\partial X(t_o)}{\partial X(t_j)}$$

so, for $i = j+1$, the sequential form of ϕ is

$$\phi(t_{j+1}, t_j) = \phi(t_{j+1}, t_o) \, \phi(t_o, t_j)$$

$$= \phi(t_{j+1}, t_o) \, \phi^{-1}(t_j, t_o). \tag{A.3}$$

This conversion of ϕ from epoch to sequential requires the inversion of a 6 x 6 matrix at each step. This can be avoided when the spacecraft force is conservative, and thus only a function of

position, by using the symplectic property of the A matrix. Recalling that

$$\dot{\phi}(t,t_o) = A(t)\phi(t,t_o) \tag{A.4}$$

where (see Chapter 2)

$$A(t) = \frac{\partial F(X,t)}{\partial X}\bigg|_{X*} . \tag{2.3}$$

If F is defined as in Eq. (2.3) then the A matrix is of the form

$$A(t) = \begin{bmatrix} A_{11} & A_{12} \\ A_{21} & A_{22} \end{bmatrix} \begin{bmatrix} 0 & I \\ \dfrac{\partial F}{\partial \overline{r}} & \dfrac{\partial F}{\partial \overline{v}} \end{bmatrix} \tag{A.5}$$

where A_{ij} are 3 x 3 submatrices of $A(t)$. If the perturbation, and hence the total force, is independent of velocity, Eq. (A.5) reduces to

$$A(t) = \begin{bmatrix} 0 & I \\ \dfrac{\partial F}{\partial \overline{r}} & 0 \end{bmatrix} . \tag{A.6}$$

Define $\overline{r} = \begin{bmatrix} x_1 \\ x_2 \\ x_3 \end{bmatrix}$, then

$$\frac{\partial F}{\partial \tilde{r}} = \begin{bmatrix} \frac{-\mu}{r^3} + \frac{3\mu x_1^2}{r^5} + \frac{\partial \tilde{P}_1}{\partial x_1} & \frac{3\mu x_1 x_2}{r^5} + \frac{\partial \tilde{P}_1}{\partial x_2} & \frac{3\mu x_1 x_3}{r^5} + \frac{\partial \tilde{P}_1}{\partial x_3} \\[2mm] \frac{3\mu x_1 x_2}{r^5} + \frac{\partial \tilde{P}_2}{\partial x_1} & \frac{-\mu}{r^3} + \frac{3\mu x_2^2}{r^5} + \frac{\partial \tilde{P}_2}{\partial x_2} & \frac{3\mu x_2 x_3}{r^5} + \frac{\partial \tilde{P}_2}{\partial x_3} \\[2mm] \frac{3\mu x_1 x_3}{r^5} + \frac{\partial \tilde{P}_3}{\partial x_1} & \frac{3\mu x_2 x_3}{r^5} + \frac{\partial \tilde{P}_3}{\partial x_2} & \frac{-\mu}{r^3} + \frac{3\mu x_3^2}{r^5} + \frac{\partial \tilde{P}_3}{\partial x_3} \end{bmatrix} \qquad (A.7)$$

and, if $\tilde{P}$ is a conservative force, then

$$\nabla \times \tilde{P} = 0 \qquad (A.8)$$

where

$$\nabla = \frac{\partial}{\partial x_1} \hat{i} + \frac{\partial}{\partial x_2} \hat{j} + \frac{\partial}{\partial x_3} \hat{k}.$$

For Eq. (A.8) to hold,

$$\frac{\partial \tilde{P}_1}{\partial x_2} = \frac{\partial \tilde{P}_2}{\partial x_1}$$

$$\frac{\partial \tilde{P}_1}{\partial x_3} = \frac{\partial \tilde{P}_3}{\partial x_1} \qquad (A.9)$$

$$\frac{\partial \tilde{P}_2}{\partial x_3} = \frac{\partial \tilde{P}_3}{\partial x_2}$$

and the submatrix $\dfrac{\partial F}{\partial \tilde{r}}$ is symmetric.

The symplectic property of $A(t)$ then states that if $A(t)$ can be expressed as

$$A(t) = \begin{bmatrix} A_{11} & A_{12} \\ A_{21} & A_{22} \end{bmatrix} \quad (A.10)$$

with

$$A_{11} = -A_{22}^T$$

$$A_{12} = A_{12}^T \quad (A.11)$$

$$A_{21} = A_{21}^T$$

then

$$\phi(t,t_o) = \begin{bmatrix} \phi_{11} & \phi_{12} \\ \phi_{21} & \phi_{22} \end{bmatrix} \quad (.\ 12)$$

and

$$\phi(t_o,t) = \phi^{-1}(t,t_o) = \begin{bmatrix} \phi_{22}^T & -\phi_{12}^T \\ -\phi_{21}^T & \phi_{11}^T \end{bmatrix}. \quad (A.13)$$

As discussed in Goldstein [1980], the state transition matrix for a conservative system is a canonical transformation in time and, therefore, satisfies the symplectic condition. The use of this property can then replace the matrix inversion in Eq. (A.3) with a simple rearranging via Eq. (A.13). If the perturbing force is not

conservative, as in the case of atmospheric drag, then the $\phi(t,t_o)$ matrix must be inverted numerically.

A.2 Conversion of $\psi(t_{j+1},t_o)$ to $\psi(t_{j+1},t_j)$

To compute the sequential form of ψ, note the following relationships for constant z,

$$x(t_1) = \phi(t_1,t_o)x(t_o) + \psi(t_1,t_o)z_o \tag{A.14}$$

$$x(t_2) = \phi(t_2,t_o)x(t_o) + \psi(t_2,t_o)z_o \tag{A.15}$$

$$x(t_2) = \phi(t_2,t_1)x(t_1) + \psi(t_2,t_1)z_o \tag{A.16}$$

and substitute Eq. (A.14) for $x(t_1)$ in Eq. (A.16)

$$x(t_2) = \phi(t_2,t_1)\phi(t_1,t_o)x(t_o) + \phi(t_2,t_1)\psi(t_1,t_o)z_o$$

$$+ \psi(t_2,t_1)z_o$$

$$= \phi(t_2,t_o)x(t_o) + \phi(t_2,t_1)\psi(t_1,t_o)z_o + \psi(t_2,t_1)z_o \tag{A.17}$$

Subtract Eq. (A.15)

$$0 = \phi(t_2,t_1)\psi(t_1,t_o)z_o + \psi(t_2,t_1)z_o - \psi(t_2,t_o)z_o \tag{A.18}$$

then the equation for $\psi(t_2,t_1)$ is

$$\psi(t_2,t_1) = \psi(t_2,t_o) - \phi(t_2,t_1)\psi(t_1,t_o) \tag{A.19}$$

or, in general,

$$\psi(t_{j+1}, t_j) = \psi(t_{j+1}, t_o) - \phi(t_{j+1}, t_j)\psi(t_j, t_o) \tag{A.20}$$

Eqs. (A.3) and (A.20) are used in conjunction with a UTOPIA run to produce a file containing the user spacecraft state, ϕ and ψ matrices for each time step desired during the period of interest.

APPENDIX B

THE U-D FILTER

The GPS onboard navigation filter is required to perform high-precision calculations even though it is operating on a microprocessor. Since typical spaceborne processors use small word lengths (16 or 32 bits), techniques must be used to improve the numerical precision and stability of the filter. Several techniques have been devised, all using some form of the square root of the covariance. Maybeck [1979] and Tapley, et al. [1980] provide descriptions of the various algorithms, and the analysis by Tapley, et al., shows that the U-D algorithm by Bierman [1977] had the lowest total numerical operations, while potentially maintaining stability in short word length machines. The U-D algorithm is recommended for GPS navigation applications, so it was tested here in the autonomous navigation role. The filter described in this report includes model noise compensation (Q matrix) for the reasons discussed in Section 4.2. While consider covariance techniques are appropriate for pre-launch studies, the added complexity and core storage required by the consider parameters make it inefficient for real-time application.

As described by Tapley and Peters [1980], the covariance matrix $P(t_k)$ can be factored into

183

$$P_k = U_k \ D_k \ U_k^T \tag{B.1}$$

where U is an upper triangular unitary matrix (with ones on the diagonal) and D is a diagonal matrix. It is well known that this factorization exists and is unique, even though the matrices U and D are not unique [Maybeck, 1979, p. 392].

B.1 U-D Propagation via the State Transition Matrix

The matrix P_k is then propagated to time t_{k+1} by the state transition method described in Section 4.3. If the state noise matrix, $Q(\tau)$, is diagonal and is expressed in the state vector space, then $B(\tau) = I$ and

$$
\begin{aligned}
P_{k+1} &= \phi(t_{k+1},t_k)P_k\phi^T(t_{k+1},t_k) + \int_{t_k}^{t_{k+1}} \phi(t_{k+1},\tau)Q(\tau)\phi^T(t_{k+1},\tau)d\tau \\
&= \phi(t_{k+1},t_k)U_kDU_k^T\phi^T(t_{k+1},t_k) \\
&\quad + \int_{t_k}^{t_{k+1}} \phi(t_{k+1},\tau)Q(\tau)\phi^T(t_{k+1},\tau)d\tau
\end{aligned} \tag{B.2}
$$

where

$$\dot{\phi}(t,t_k) = A(t)\phi(t,t_k) \ , \quad \phi(t_k,t_k) = I \tag{B.3}$$

and

$$A(t) \equiv \left. \frac{\partial F(X(t),t)}{\partial X(t)} \right|_{X*(t)} \tag{B.4}$$

To propagate U and D, form the augmented matrices

$$W_{k+1} = \left[\phi(t_{k+1}, t_k)U_k \mid C_{k+1} \right] \tag{B.5}$$

and

$$\tilde{D}_k = \begin{bmatrix} D_k & 0 \\ 0 & Q_k/\Delta t \end{bmatrix} \tag{B.6}$$

where

$$C_{k+1} = \int_{t_k}^{t_{k+1}} \phi(t_{k+1}, \tau)d\tau \tag{B.7}$$

$$\Delta t = t_{k+1} - t_k \tag{B.8}$$

Now W_{k+1} will not be upper triangular, but $\overline{U}_{k+1}$ and $\overline{D}_{k+1}$ can be obtained by a modified Gram-Schmidt orthogonalization on W_{k+1} weighted by K_k such that

$$\overline{P}_{k+1} = \overline{U}_{k+1}\overline{D}_{k+1}\overline{U}_{k+1}^T = \overline{W}_{k+1}D_k\overline{W}_{k+1}^T \tag{B.9}$$

Note that this method requires the integration of the $n \times n$ $\dot{\phi}$ equation and the $n \times n$ C_{k+1} integral, plus the triangularization of $\overline{W}_{k+1}$.

B.2 U-D Propagation via $\dot{U}$ and $\dot{D}$

To improve the U-D propagation efficiency, Tapley and Peters propose integrating the U-D form of the matrix Riccati

equation

$$\dot{\overline{P}}(t) = A(t)\overline{P}(t) + \overline{P}(t)A^T(t) + Q(t) .$$

(B.10)

If

$$\overline{P} = \overline{U}\ \overline{D}\ \overline{U}^T$$

(B.11)

and

$$\overline{Q} = Q/2$$

(B.12)

then

$$\dot{\overline{P}} = \dot{\overline{U}}\ \overline{D}\ \overline{U}^T + \overline{U}\ \dot{\overline{D}}\ \overline{U}^T + \overline{U}\ \overline{D}\ \dot{\overline{U}}^T$$

(B.13)

and

$$\dot{\overline{U}}\ \overline{D}\ \overline{U}^T + \overline{U}\ \dot{\overline{D}}\ \overline{U}^T = A\ \overline{P} + \overline{P}\ A^T + \overline{Q} + \overline{Q} .$$

(B.14)

Rearranging,

$$(\dot{\overline{U}}\ \overline{D} + \overline{U}\ \frac{\dot{\overline{D}}}{2} - \overline{Q}\ \overline{U}^{-T} - A\ \overline{U}\ \overline{D})\ \overline{U}^T$$

$$+ U\ (\overline{D}\ \dot{\overline{U}}^T + \frac{\dot{\overline{D}}}{2}\ \overline{U}^T - \overline{U}^{-1}\ \overline{Q} - \overline{D}\ \overline{U}^T\ A^T) = 0 .$$

(B.15)

Define

$$E(t) = (\dot{\overline{U}}\ \overline{D} + \overline{U}\ \frac{\dot{\overline{D}}}{2} - \overline{Q}\ \overline{U}^{-1} - A\ \overline{U}\ \overline{D})\ \overline{U}^T$$

(B.16)

then $E(t) + E^T(t) = 0$ and Eq. (B.15) can be simplified to

$$\left(\dot{\overline{U}}\,\overline{D} + \overline{U}\,\dot{\overline{\frac{D}{2}}} - A\,\overline{U}\,\overline{D}\right) U^T = \overline{Q} + E(t) \equiv \tilde{E}(t) \tag{B.17}$$

The elements of $E(t)$ can be specified to maintain the triangular form of U during the integration by defining the matrices:

$$T \equiv A\,\overline{U}\,\overline{D} \tag{B.18}$$

$$M \equiv \dot{\overline{U}}\,\overline{D} + \overline{U}\,\dot{\overline{\frac{D}{2}}} - T \tag{B.19}$$

Then

$$M^T = \tilde{E} = \overline{Q} + E \tag{B.20}$$

For $\overline{U}$ and $\dot{\overline{U}}$ to be upper triangular, there are $n(n-1)/2$ unknowns in the skew symmetric matrix $\tilde{E}$. The products $\dot{\overline{U}}\,\overline{D}$ and $\overline{U}\,\dot{\overline{D}}$ are upper triangular creating $n(n+1)/2$ unknowns. The whole system (Eq. (B.20) then has $\frac{n(n-1)}{2} + \frac{n(n+1)}{2} = n \times n$ unknowns, the same as P, which can be uniquely determined. The elements of Eq. (B.20) are

$$\begin{bmatrix} m_{11} & m_{21} & \cdots & m_{n1} \\ \cdot & m_{22} & & m_{n2} \\ \cdot & & & \vdots \\ \cdot & & \cdot & \\ m_{1,n-1} & & \cdot & m_{n,n-1} \\ -t_{1n} & -t_{2n} & \cdots & m_{nn} \end{bmatrix} \begin{bmatrix} \overline{u}_{12} & \cdots & & 0 \\ \overline{u}_{13} & & & \cdot \\ \cdot & & \cdot & \\ \cdot & & \cdot & 0 \\ \overline{u}_{1n} & \cdots & & u_{n-1,n1} \end{bmatrix}$$

$$= \begin{bmatrix} \tilde{q}_{11} & -e_{21} & \cdots & -e_{n,1} \\ e_{12} & \tilde{q}_{22} & & \cdot \\ \cdot & & & \cdot \\ \cdot & & \ddots & \cdot \\ e_{1,n-1} & & \cdot & -e_{n,n-1} \\ e_{1n} & e_{2n} & \cdots & \tilde{q}_{nn} \end{bmatrix}$$

and the solution to this equation for M is obtained noting that

$$m_{nn} = \bar{q}_{nn} \tag{B.21}$$

$$t_{n-1,n} + m_{nn}\, u_{n-1,n} = e_{n,n-1} \tag{B.22}$$

$$m_{n,n-1} = -e_{n,n-1} \tag{B.23}$$

and that Equations (B.22) and (B.23) can be solved for the two unknowns $m_{n,n-1}$ and $e_{n,n-1}$. This process then proceeds backwards up through the M matrix until M and E have been determined:

$\dot{\bar{U}}$ and $\dot{\bar{D}}$ are then obtained from

$$\dot{\bar{U}}\,\bar{D} + \bar{U}\,\frac{\dot{\bar{D}}}{2} = M + T \tag{B.24}$$

or

$$m_{ij} + t_{ij} = \sum_{k=1}^{n} \dot{\bar{u}}_{ik}\,\bar{d}_{kj} + \sum_{k=1}^{n} \frac{\bar{u}_{ik}\dot{\bar{d}}_{kj}}{2}$$

$$= \dot{\bar{u}}_{ij} \, \bar{d}_{jj} + \frac{\bar{u}_{ij} \, \dot{\bar{d}}_{jj}}{2} \, . \tag{B.25}$$

$$(j = 1,\ldots,n)(i = 1,\ldots,j)$$

For $i = j$, $\bar{u}_{ij} = 1$, so $\dot{\bar{u}}_{ij} = 0$ and Eq. (B.24) becomes

$$\dot{\bar{d}}_{ii} = 2(m_{ii} + t_{ii}) \quad (i = 1,\ldots,n) \tag{B.26}$$

which provides the solution for the diagonal matrix $\dot{\bar{D}}$

Since $\bar{U}$ is upper triangular, terms for which $i > j$ are zero, thus the only case left is for $i < j$, which gives

$$\dot{\bar{u}}_{ij} = \left[m_{ij} + t_{ij} - u_{ij} \, \frac{\dot{\bar{d}}_{jj}}{2} \right] / \bar{d}_{jj} \tag{B.27}$$

$$(i = 1,\ldots,j-1) \quad (j = 2,\ldots,n)$$

Eqs. (B.26) and (B.27) are then used in the derivative subroutine of a numerical integrator to provide $\bar{U}(t)$ and $\bar{D}(t)$. Note that UDU^T is never formed in the propagation algorithm.

B.3 U-D Measurement Update

The Kalman measurement update to the covariance matrix for a scalar observation at $t = t_{k+1}$ is

$$P = (I - KH)\bar{P} = \bar{P} - KH\bar{P} \tag{B.28}$$

where

$$K = \overline{P} H^T (H \overline{P} H^T + R)^{-1} \tag{B.29}$$

and

$$H = \frac{\partial G(X(t_{k+1}), t_{k+1})}{\partial X(t_{k+1})} \bigg|_{X^*(t_{k+1})} \tag{B.30}$$

P can be factored [Maybeck, 1979] as

$$UDU^T = \overline{U} \, \overline{D} \, \overline{U}^T - (1/\alpha)(\overline{U} \, \overline{D} \, \overline{U}^T H^T) \, H \, \overline{U} \, \overline{D} \, \overline{U}^T$$

$$= \overline{U} \left[\overline{D} - (1/\alpha)(\overline{D} \, \overline{U}^T H^T)(\overline{D} \, \overline{U}^T H^T)^T \right] \overline{U}^T . \tag{B.31}$$

where

$$\alpha = H\overline{P}H^T + R \tag{B.32}$$

Now, define the vectors

$$f = \overline{U}^T H^T \tag{B.33}$$

$$v = \overline{D} f = \overline{D} \, \overline{U}^T H^T \tag{B.34}$$

and Eq. (B.31) becomes

$$UDU^T = \overline{U} \left[\overline{D} - (1/\alpha) v \, v^T \right]^T U^T \tag{B.35}$$

where $v \, v^T$ and $\overline{D} - (1/\alpha) v \, v^T$ are now symmetric n x n matrices. Applying the decomposition algorithm to $\overline{D} - (1/\alpha) v \, v^T$ yields a

unit upper triangular matrix, U^+, and a diagonal matrix, D^+. Then

$$UDU^T \approx (\bar{U}\ U^+)D^+(\bar{U}\ U^+)^T \qquad (B.36)$$

and

$$U = \bar{U}\ U^+ \qquad (B.37)$$

$$D = D^+ \qquad (B.38)$$

The factor $1/\alpha$ still contains the product HPH^T; however, by calculating U and D in a recursive manner, the explicit formation of P is avoided. The method also gives the Kalman gain, K, in a recursive form. The Kalman state update algorithm then proceeds as follows:

Set $\alpha_o = R$ $\qquad (B.39)$

Compute

$$f_i = h_i + \sum_{\ell=i+1}^{n} h_\ell \bar{u}_{\ell i} \qquad (B.40)$$

$$v_i = \bar{d}_{ii}\ f_i \qquad (B.41)$$

$$\alpha_i = \alpha_{i-1} + f_i\ v_i \qquad (B.42)$$

$$d_i = \bar{d}_i\ \alpha_{i-1}/\alpha_i \qquad (B.43)$$

$$b_i = v_i \qquad (B.44)$$

$$p_i = -f_i/\alpha_{i-1} \tag{B.45}$$

$$u_{j_i} = \bar{u}_{ji} + b_j \, p_i \quad (j=1,2,\ldots,i-1) \tag{B.46}$$

$$b_j = b_j + u_{j_i} \, v_i \quad (j=1,2,\ldots,i-1) \tag{B.47}$$

The new vector B, is then used to compute the Kalman gain

$$K = B/\alpha_n \tag{B.48}$$

and

$$\hat{x}(t_{k+1}) = \bar{x}(t_{k+1}) + K \left[y_{k+1} - H_{k+1} \hat{x}(t_{k+1}) \right] . \tag{B.49}$$

Note that this formulation still computes the components of the matrix $P = UDU^T$ when it is recursively solving for f_i , v_i and α_i . This is true of all square root filters, even though the product is usually hidden in the recursion relations.

REFERENCES

Anderle, R. J., "The Global Positioning System," Philosophical Transactions of the Royal Society of London, A294, 395-406, p. 185-196, 1980.

The Astronautical Almanac, U. S. Government Printing Office, 1983.

Aviation Week and Space Technology, "Military Official Stresses Need for Survivable Space Systems," Vol. 116, No. 3, pp. 22-23, January 18, 1982.

Ball Aerospace Systems Division, Boulder, CO, "Solid State Detector Star Tracker Development at Ball Aerospace Systems Division," Briefing Charts, July 1981.

Ballentine, W. A., "DOD/NASA Gemini Experiment Summary," Gemini Summary Conference, February 1-2, 1967, NASA SP-138, pp. 307, 1967.

Barnes, J. A. and S. Jarvis, Jr., "Efficient Numerical and Analog Modeling of Flicker Noise Processes," Tech. Note 604, National Bureau of Standards, Boulder, CO, 1971.

Barr, J., "Use of ITS in Ephemeris Calculations," IONDS Technical Memo #81-9, September 23, 1981.

Bierman, G. J., Factorization Methods for Discrete Sequential Estimation, Academic Press, New York, 1977.

Book, S. A., W. F. Brady and P. K. Mazaika, "The Nonuniform GPS

Constellation," Paper No. CH1597-4180, IEEE Position Location
and Navigation Symposium, Dayton, OH, 1980.

Brogan, W. L. and J. L. Lemay, "Autonomous Orbit Determination at
Synchronous Altitude," AAS Paper 68-129, September 3, 1968.

Bureau International de l'Heure, Annual Report, Paris, France, 1975,
1976, 1977, 1978, 1979, 1980, 1981.

Chambers, R. J., "Earth Limb Determination Using MADAN," Aerospace
Corporation Memorandum 81-M-109, June 1, 1981.

Chao, C. C., "A Preliminary Investigation of GPS Autonomous
Navigation," Aerospace Corp., ATM81 (1476-03) 1, March 1, 1981.

Clynch, J. R., "Effects of Weather Variations on the SHAD System: A
Preliminary Study," Applied Research Laboratories Report No.
79-57, The University of Texas at Austin, November 1979.

Clynch, J. R., "Refraction of a Star Grazing the Atmosphere: The
Gaussian Approximation," Applied Research Laboratories, The
University of Texas at Austin, May 1981.

Clynch, J. R., "Effects of Weather Variations on the SHAD System,"
Applied Rearch Laboratories Report No. 81-32, The University of
Texas at Austin, July 1981.

Ellis, J. F. and G. A. Creswell, "Interferometric Attitude
Determination with the Global Positioning System," Journal of
Guidance and Control, Vol. 2, No. 6, pp. 522-527, Nov-Dec 1978.

Fang, B. T., "Geometric Dilution of Precision in Global Positioning
System Navigation," Journal of Guidance and Control, Vol. 4,

No. 1, pp. 92-94, Jan-Feb 1981.

Ferguson, J. R., Jr. and G. T. Kroncke, "Dumping Momentum Magnetically on GPS Satellites," Journal of Guidance and Control, Vol. 4, pp. 87-90, Jan-Feb 1980.

Fowler, R. W., "Briefing on Earth Horizon Sensors," Los Angeles AFS, Calif., June 23, 1981.

Fuchs, A. J., W. H. Wooden, II, and A. C. Long, "Autonomous Satellite Navigation with the Global Positioning System," AAS/AIAA Astrodynamics Specialist Conference, Wyoming, September 7-9, 1977.

General Dynamics Electronics Division, San Diego, CA, "Computer Program specification for the GPS Master Control Station Ephemeris Computer Programs," CP-CS-304, Part I, January 1975.

Gerster, R. H. and Schwarzbein, Z. E., "Self-Contained Orbit Determination Techniques," AIAA Paper No. 63-431, AIAA Astrodynamics Conference, August 19-21, 1963.

Geyling, F. T. and H. R. Westerman, Introduction to Orbital Mechanics, Addison-Wesley, Reading, MA, 1971.

Goldstein, H., Classical Mechanics, Addison Wesley, Reading, Mass., 1980, p. 393.

Gura, I. A., A. S. Abbott and H. T. Hendrickson, "Configuration Studies for Autonomous Satellite Navigation," Aerospace Corporation, TR-0059(6784)-1, May 28, 1971.

Henry, R. C., "Manned Space Flight Navigation Techniques," The

Journal _of_ _the_ _Institute_ _of_ _Navigation_, Vol. 16, No. 4, pp. 449-461, October 1963.

Honeywell Aerospace Division, St. Petersburg, FL, "Space Precision Attitude Reference System (SPARS) Phase II Final Report," March 1973.

Jazwinski, A. H., _Stochastic_ _Processes_ _and_ _Filtering_ _Theory_, Academic Press, New York, 1970.

Kartaschoff, P., _Frequency_ _and_ _Time_, Academic Press, London, 1978.

Kelso, J. M., _Radio_ _Ray_ _Propagation_ _in_ _the_ _Ionosphere_, McGraw-Hill, Inc., New York, 1964, p. 189.

Kerr, T. H. and L. Chin, "A Stable Decentralized Filtering Implementation for JTIDS RELNAV," Paper No. CH1597-4318, IEEE Position Location and Navigation Symposium, Dayton, OH, 1980.

Kerr, T. H. and L. Chin, "The Theory and Techniques of Discrete Time Decentralized Filters," _Agard_ _Advances_ _in_ _the_ _Techniques_ _and_ _Technology_ _of_ _the_ _Applications_ _of_ _Nonlinear_ _Filters_ _and_ _Common_ _Filters_, NATO, March 1982.

Laning, J. H., Jr., and R. H. Battin, _Random_ _Processes_ _in_ _Automatic_ _Control_, R. E. Krieger Publishing Co., New York, 1977.

Lemay, J. L., W. L. Brogan, C. E. Seal and H. T. Hendrickson, "High Altitude Navigation Study (HANS)," Aerospace Corporation, TR-0073(3491)-1, June 29, 1973.

Liu, A. S., "Satellite Autonomous Navigation Using Satellite-to-Satellite Data: An Error Analysis," Aerospace Corporation, ATM

81-(6476-03)-3, June 8, 1981.

Martin-Marietta Corporation, Denver, CO, "Space Sextant High Altitude Navigation System (SS-HANS) Study, Phase 0 Final Report," March 1975.

Martin-Marietta Corporation, Denver, CO, "Space Sextant: Mini-HALO Reference System, Technical Description," October 1980.

Martin-Marietta Corporation, Denver, CO, "Preliminary Computer Product Specification (Type C-5) Autonomous Navigation and Attitude Reference System (ANARS) (Draft)," Specification No. CO5-SS-ANARS-CSP-01 (Rev. 2), pp. 3.2.3-159, 3.2.8-78, April 15, 1981.

Maybeck, P. S., Stochastic Models, Estimation and Control, Volume 1, Academic Press, New York, 1979.

McMillan, J. D., "Mathematical Specifications of the University of Texas Orbit Processor and Application to the Laser Observations of the Beacon Explorer-C Satellite," Master's Thesis, The University of Texas at Austin, May 1973.

Meditch, J. S., "Clock Error Models for Simulation and Estimation," Aerospace Corporation, TOR 0076(6474-01)-2, 1975.

Meyerhoff, S. L., "Error Statistics from Predicting UT1-UTC and Pole Position," NSWC/DL-TR-3859, Naval Surface Weapons Center, Dahlgren, VA, August 1978.

Milliken, R. J. and C. J. Zoller, "Principle and Operation of NAVSTAR and System Characteristics," Global Positioning System,

The Institute of Navigation, Washington, D. C., 1980.

Murata, M., _Autonomous Navigation Methods Using the Global Positioning System_, Ph.D. Dissertation, The University of Texas at Austin, May 1982.

Nikolaev, A. G., N. F. Romanteev, V. I. Sevast'yanov and A. V. Levitskii, "Methods for Increasing the Efficiency in Using Astronomical Measuring Means of Astrogation," translated from _Kosmicheskie Issledovaniya_, Vol. 13, No. 4, pp. 595-602, Jul-Aug, 1975.

Owens, J. C., "Optical Refractive Index of Air: Dependence on Pressure, Temperature and Composition," _Applied Optics_ 6, 51, 1967.

Payne, C. R., Jr., "NAVSTAR Global Positioning System: 1982," Paper No. 64, Third International Geodetic Symposium on Satellite Doppler Positioning, Las Cruces, NM, February 1982.

Quell, F., "Stellar Horizon Atmospheric Dispersion (SHAD) Positioning System," Briefing at Los Angeles AFS, Calif., June 9, 1981.

Salomon, P. M., "Charge-Coupled Device (CCD) Trackers for High-Accuracy Guidance Applications," _Optical Engineering_, Vol. 2, No. 1, pp. 135-142, Jan-Feb 1981.

Sanders, C. W., E. C. Tacker and T. D. Linton, "Decentralized Estimation Via Constrained Filters," Tech. Report ECE-73-1, University of Wisconsin-Madison, 1973.

Shah, M., "Suboptimal Filtering Theory for Interacting Control Systems," Ph.D. Dissertation, Cambridge University, Cambridge, England, 1971.

Singh, M. G. and A. Titli, Systems: Decomposition, Optimization and Control, Pergamon Press, New York, 1978.

Tapley, B. D. and J. R. Ferguson, "Autonomous Spacecraft Navigation Using Current and Planned Sensor Data," Applied Research Laboratories, Report No. TR83-14, The University of Texas at Austin, December 1983.

Tapley, B. D. and J. G. Peters, "Sequential Estimation Algorithm Using a Continuous UDU^T Covariance Factorization," Journal of Guidance and Control, Vol. 3, No. 4, pp. 326-331, July-August 1980.

Tapley, B. D., J. G. Peters and B. E. Schutz, "A Comparisson of Square Root Estimation Algorithms for Autonomous Satellite Navigation," IASOM Report No. TR79-1, The University of Texas at Austin, March 1980.

TRW, Redondo Beach, CA, "Proposal for Multimission Attitude Determination and Autonomous Navigation (MADAN) System," August 31, 1979.

Van Dierendonck, A. J., S. S. Russell, E. R. Kopitzke and M. Birnbaum, "The GPS Navigation Message," Global Positioning System, The Institute of Navigation, Washington, D. C., 1980.

Wagner, C. A. and F. J. Lerch, "The Accuracy of Geopotential

Models," <u>Planetary Space Science</u>, Vol. 26, pp. 1081-1140, 1978.

Walsh, R. C. and J. R. Ferguson, "The United States Air Force Manual Space Navigation Experiment on Skylab (DOD/NASA Skylab Experiment T-002)," USAFA-TR-75-5, United States Air Force Academy, CO, 1975.

Wilson, T., <u>User's Reference Guide for the University of Texas Orbit Processor</u>, Master's Thesis, The University of Texas at Austin, December 1976.

Zhu, S. Y., "Prediction of Earth Rotation and Polar Motion," Report No. 320, Department of Geodetic Science and Surveying, Ohio State University Research Fondation, September 1981.

Zybin, Y. N., "A Method for Autonomous Navigation of Artificial Satellites," translated from <u>Kosmicheskie Issledovaniya</u>, Vol. 7, No. 2, pp. 213-219, Mar-Apr 1969.

VITA

Jackson Robert Ferguson,

After completing his work at Travis High School,
Austin, Texas, in 1960, he entered The University of Texas at Austin.
He entered the United States Air Force Academy in 1961 and received
the degree of Bachelor of Science in Engineering Science in 1965.
During the following five years, he was employed as an Astronautical
Engineer for the Air Force Satellite Control Facility in Sunnyvale,
California. In December, 1971, he received the degree of Master of
Science in Astronautics from the Air Force Institute of Technology.
Since that time, he has been employed at the NORAD Cheyenne Mountain
Complex and as an Assistant Professor of Astronautical Engineering at
the United States Air Force Academy. He entered Graduate School at
The University of Texas at Austin in January, 1980.

This dissertation was typed by Karen B. Johnson.